Frontiers of Physics
https://doi.org/10.1007/s11467-021-1070-0
Front. Phys.
16(5), 53302 (2021)

REVIEW ARTICLE

Negative thermal expansion: Mechanisms and materials

Erjun Liang†, Qiang Sun, Huanli Yuan, Jiaqi Wang, Gaojie Zeng, Qilong Gao

Key Laboratory of Materials Physics of Ministry of Education of China, and School of Physics & Microelectronics, Zhengzhou University, Zhengzhou 450001, China
Corresponding author. E-mail: †ejliang@zzu.edu.cn
Received October 14, 2020; accepted March 5, 2021

Negative thermal expansion (NTE) of materials is an intriguing phenomenon challenging the concept of traditional lattice dynamics and of importance for a variety of applications. Progresses in this field develop markedly and update continuously our knowledge on the NTE behavior of materials. In this article, we review the most recent understandings on the underlying mechanisms (anharmonic phonon vibration, magnetovolume effect, ferroelectrorestriction and charge transfer) of thermal shrinkage and the development of NTE materials under each mechanism from both the theoretical and experimental aspects. Besides the low frequency optical phonons which are usually accepted as the origins of NTE in framework structures, NTE driven by acoustic phonons and the interplay between anisotropic elasticity and phonons are stressed. Based on the data documented, some problems affecting applications of NTE materials are discussed and strategies for discovering and design novel framework structured NET materials are also presented.

Keywords negative thermal expansion, mechanisms of thermal contraction, negative thermal expansion materials, lattice thermal dynamics, magnetovolume effect, ferroelectrostriction, charge transfer, anisotropic elasticity

Contents

1 Introduction 2
2 Fundamentals of thermal expansion and contraction 2
2.1 Anharmonic oscillator 2
2.2 Rigid unit modes model 3
2.3 Correlations between phonon vibration and thermal expansion 4
2.4 NTE driven by acoustic phonon modes 4
2.5 Interplay between phonons and anisotropic elasticity 6
3 NTE in framework structures 7
3.1 AM_2O_8 7
3.2 AV_2O_7 7
3.3 $Cu_2M_2O_7$ 8
3.4 $A_2M_3O_{12}$-based compounds 9
3.4.1 ABM_3O_{12} 9
3.4.2 ABM_2XO_{12} 10
3.5 AMO_5 10
3.6 Cu_2O and Ag_2O 10
3.7 $A_2O(PO_4)_2$ 11
3.8 ScF_3 and related materials 11
3.9 Cyanides and Prussian blue analogues 12
3.10 MOFs 13
3.11 2D materials 13
4 NTE induced by spontaneous volume magnetostriction 14
4.1 Mechanism of spontaneous volume magnetostriction 14
4.2 Invar alloy and magnetic intermetallic compounds 16
4.3 Antiperovskite manganese nitrides Mn_3AN (A =Zn, Ga, etc.) 16
4.4 Magnetic oxides 17
5 NTE induced by spontaneous volume ferroelectrostriction 17
5.1 Mechanism of NTE driven by spontaneous polarization 17
5.2 $PbTiO_3$-based compounds 18
5.3 $PbVO_3$ 18
5.4 $Sn_2P_2S_6$ 18
5.5 GeTe 18
6 NTE induced by charge transfer 18
6.1 Mechanisms of NTE driven by charge transfer 18
6.2 Rare-earth fullerides 19
6.3 SmS-based monosulfides 19
6.4 $LaCu_3Fe_4O_{12}$, La-doped $BiNiO_3$ and V_2OPO_4 19
7 NTE in layered perovskites like oxides 20
7.1 Sr_2IrO_4 20

*Special Topic: Thermodynamics and Thermal Metamaterials (Editor: Ji-Ping Huang). This article can also be found at http://journal.hep.com.cn/fop/EN/10.1007/s11467-021-1070-0.

© Higher Education Press 2021

7.2 Sr_2RhO_4 20
7.3 Ca_2MnO_4 and Ca_2GeO_4 21
7.4 $Ca_3Mn_2O_7$ 21
7.5 $LaTaO_4$ 21
7.6 Ca_2RuO_4 21
8 Tailoring the properties of framework oxides 22
8.1 Phase transition 23
8.2 Hygroscopicity 23
9 Strategies for discovering and design novel NTE materials 24
9.1 The role of the length of lattice parameter on the tuning of thermal expansion 24
9.2 The concept of AAV 25
9.3 Criterions for design NTE materials without hygroscopicity 25
10 Conclusions and prospects 25
Acknowledgements 26
References 26

1 Introduction

Negative thermal expansion (NTE) of materials is an abnormal phenomenon which challenges conventional lattice thermal dynamics. It is well known that most of materials expand on heating and contract on cooling with different rates. Thermal expansion and the mismatch in coefficients of thermal expansion (CTE) in solids could cause serious problems for devices and instruments such as deterioration of performance, fatigue, temporary and permanent damage and cracking. Thermal expansion property is a critical factor in high performance devices that affects the device application environments and working lifetime. Materials with NTE, i.e., their volumes shrink on heating, are rare, but highly desirable for tailoring CTEs from negative to zero and positive in a variety of fields since thermal shock resistance of a material is inversely proportional to its coefficient of thermal expansion [1].

The rediscovery of isotropic NTE of ZrW_2O_8 in a wide temperature range (0.3–1050 K) prompted great activities in NTE materials research due to scientific curiosity and technical importance [2]. Since then increasing members of materials have been found to display NTE with very different mechanisms, such as framework oxides [3–6], cyanides and Prussian blue analogous [7–10], fluorides [11–13] and two-dimensional materials [14, 15] whose NTE are driven by anharmonic phonon vibrations, antiperovskite manganese nitrides Mn_3AN (A = Zn, Ga, etc.) and La(Fe, Si)$_{13}$-based compounds [19, 20] via magnetovolume effect, $PbTiO_3$-based compounds [21] driven by complex effects of spontaneous volume ferroelectrostriction, volume fraction change [22] and the interplay between phonons and anisotropic elasticity [23], Perovskites $LaCu_3Fe_4O_{12}$ [24] and La-doped $BiNiO_3$ [25] by intermetallic charge transfer.

Experimental and theoretical progresses in this field develop markedly and update continuously our knowledge on the NTE behavior of materials. Besides the conventional understanding of the NTE driven by rigid unit modes or transverse displacements of bridge atoms in framework structures, most recent works suggested that acoustic phonons and the interplay between the phonons and anisotropic elasticity of a material can be important in understanding the origins of NTE behavior. In this article, we review the most recent understandings of the origins of NTE behavior in different categories of materials and the achievements of NTE materials developed recently from both the theoretical and experimental aspects. In the following, we describe briefly the fundamental aspects of phonon thermal dynamics associated with thermal expansion and contraction, and then review the progress of NTE materials under each category of mechanisms. Besides discussing fundamental problems, we will also address the issues associated with applications of NTE materials and present some strategies for discovering and design NTE materials with excellent integrity properties based on documented data analyses, followed by the summary and prospects.

2 Fundamentals of thermal expansion and contraction

2.1 Anharmonic oscillator

Figure 1(a) depicts schematically the interatomic potentials for a harmonic and an anharmonic oscillator as a function of interatomic distance. In contrast to the harmonic oscillator whose average interatomic distance does not change with temperature, the average interatomic distance r_i increases with increasing thermal energy for a true anharmonic oscillator. Thermal expansion is therefore an anharmonic effect arising from interatomic interactions.

For a harmonic oscillator, the interatomic potential is given by

$$U(r) = \frac{1}{2}(r - r_0)^2, \tag{1}$$

where r_0 is interatomic distance at equilibrium. The vibration energy of the oscillator is given by

$$E_{vib} = \hbar\omega_0(n + \frac{1}{2}), \tag{2}$$

where ω_0 is the vibration frequency of the harmonic oscillator and n is the quantum number of vibration. For an anharmonic oscillator, higher order terms must be included in the potential function,

$$U(r) = D_0 + A(r - r_0)^2 + B(r - r_0)^3 + C(r - r_0)^4 + \cdots . \tag{3}$$

The cubic term is negative and produces a decrease in frequency. The quartic term is positive and produces an

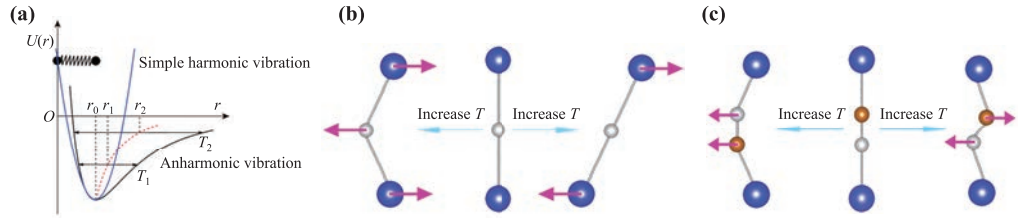

Fig. 1 **(a)** Potential energy $U(r)$ as a function of interatomic separation r for a harmonic (blue curve) and anharmonic (black curve) oscillators, **(b, c)** Schematic illustration for bend/transverse and rotation/librational vibrations driving NTE.

increase of frequency but is only three-fifths of the cubic one by assuming for the covalent bond of silicon with a Morse potential,

$$U(r) = -D_e - D_e\left[1 - \mathrm{e}^{-\beta(r-r_0)}\right]^2, \tag{4}$$

If the perturbation by the higher-order (third and fourth) terms is small compared to the harmonic term (which is usually the case), it can be shown to a good approximation that the eigenvalue of the perturbed state can still be expressed as an oscillator energy

$$\begin{aligned} E_{vib} &= \hbar\omega_0\left(n+\frac{1}{2}\right) - \chi_e\hbar\omega_0\left(n+\frac{1}{2}\right)^2 \\ &= \hbar\omega(n+\frac{1}{2}), \end{aligned} \tag{5}$$

$$\omega = \omega_0[1-\chi_e(n+\frac{1}{2})], \tag{6}$$

where $\chi_e = \frac{\hbar\omega}{4D_e} > 0$ is the constant of anharmonicity, and D_e is the dissociation energy of the bond. Eq. (6) indicates that the vibration frequency ω of the anharmonic oscillator is lower than ω_0, the frequency of the harmonic oscillator.

In a solid, the n_i can be regarded as the occupation number of phonons of frequency ω_i at temperature T, which conforms the Bose–Einstein distribution

$$\mathrm{n}_i = \frac{1}{\mathrm{e}^{\hbar\omega_{i/(k_BT)}} - 1}. \tag{7}$$

The eigenvalue of the perturbed state may still be expressed as the sum of oscillator energy

$$E_i = \hbar\omega_i(n_i + \frac{1}{2}). \tag{8}$$

When the temperature approaches the absolute zero Kelvin, n_i approaches zero. The phonon frequency becomes $\omega_i = \omega_{i0}(1-\frac{\chi_e}{2})$. Eq. (6) indicates that the phonon frequency is the highest at the ground state and lowers continuously with the increase of temperature. This explains why red shifts of phonon frequencies are usually observed experimentally. The changes in phonon frequency with temperature are manifestations of anharmonicity in the lattice potential energy.

Generally, phonon frequencies decrease with the increase of temperature and one sees a bond length increase from Fig. 1(a), corresponding to a thermal expansion along the bond direction. However, abnormal changes of phonon frequency with temperature and pressure can also occur, particularly for the low frequency modes associated with anharmonic transverse/bending and rotation/librational motions as shown in Figs. 1(b) and (c). Such motions will lead to the two end atoms to become closer in the vertical direction with the increase of temperature. The value of contraction is proportional to the magnitudes of transverse and librational vibrations. This is a simplest geometric manifestation of NTE. Many experimental and theoretical investigations demonstrate that the low frequency phonon modes involving transverse and librational vibrations contribute to the NTE of framework structures of solids.

2.2 Rigid unit modes model

The rigid unit modes (RUMs) model was initially developed to understand the origin of displacive phase transitions in tetrahedral framework structures [26]. In this RUM model a framework structure is viewed as a 3-D periodic network of interconnecting corner sharing polyhedra, which are treated as rigid units. As shown in Fig. 2, polyhedral rotations associated with transverse displacements of corner-sharing atoms consume the space in the framework and causing a shrinkage of lattice with increasing temperature. The RUMs model automatically provides a geometrical mechanism for NTE which is not restricted to any limited range of temperatures.

Though the RUMs model presents a qualitative scenario

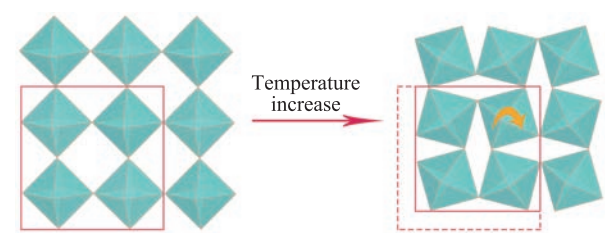

Fig. 2 Rigid unit mode flexibility of a two-dimensional polyhedra array.

of NTE in ZrW_2O_8 and some other NTE materials [27–29], however, the presence of RUMs is not a reliable indicator for NTE. Detailed RUMs calculations of ten framework oxide structures negate any simple and direct correlation between the presence or absence of RUMs in a structure and its NTE property [3]. According to this model, there are no RUMs in any systems containing octahedra except those contain non-bridging atoms such as ZrW_2O_8 [31]. There are no RUMs in ZrV_2O_7 [32] and $A_2M_3O_{12}$ family of materials [33] but strong NTE has been observed over very large temperature ranges in these compounds. Cu_2O is one of the simplest materials showing NTE but the structure is simply too-closely packed to permit RUMs flexibility [28]. The RUMs description of NTE has been shown to be inconsistent with experimental [34] and theoretical [35] observations in Cu_2O. The quasi-harmonic approximation (implicit in any RUMs formalism) has been shown to be insufficient in ScF_3 [11, 36]. Quasi-RUMs involving distortions of polyhedra have been frequently used to qualitatively understand the NTE behavior in a large number of framework structures.

2.3 Correlations between phonon vibration and thermal expansion

Thermal expansion in solids arises due to anharmonicity of the effective interaction between atoms, in which phonons are involved. The Grüneisen relation predicts that the volume coefficient of thermal expansion of solids has the same temperature dependence as the specific heat at constant volume [37],

$$\alpha_V = \frac{1}{V}\left(\frac{\partial V}{\partial T}\right)_P = \frac{1}{B}\left(\frac{\partial S}{\partial V}\right)_T = \frac{1}{V}\frac{\gamma C_V(T)}{B}, \tag{9}$$

where γ, C_V, B, V and S are the bulk Grüneisen parameter, the specific heat capacity at constant volume, isothermal bulk modulus, volume and entropy, respectively. $B = 1/\chi = -V\,(\partial P/\partial V)_T$, where χ is compressibility. The Grüneisen parameter is a measure of lattice anharmonicity. Eq. (9) indicates that negative thermal expansion of a material requires the Grüneisen parameter to be negative.

Considering the contribution of each mode, the mode specific heat capacity $c_i(T)$ for the mode with frequency ω_i is given by the well known Einstein function

$$c_i(\mathrm{T}) = \left(\frac{\partial E_i}{\partial T}\right)_V = k_B\left(\frac{\hbar\omega_i}{k_BT}\right)^2/[\exp\left(\frac{\hbar\omega_i}{k_BT}\right)-1]^2, \tag{10}$$

where k_B is Boltzmann constant. The bulk Grüneisen parameter $\gamma = \sum_i \gamma_i c_i / \sum_i c_i$. Eq. (9) becomes

$$\alpha_V = \frac{k_B}{V_0 B}\sum_i \gamma_i p_i \left(\frac{\hbar\omega_i}{k_BT}\right)^2 \exp\left(\frac{\hbar\omega_i}{k_BT}\right) \times \left[\exp\left(\frac{\hbar\omega_i}{k_BT}\right)-1\right]^{-2}, \tag{11}$$

where p_i is the degeneracy of the phonon mode with frequency ω_i of the ith branch at the Brillouin zone center, and γ_i is the mode Grüneisen parameter of the phonon with frequency ω_i, which is defined as [38]

$$\gamma_i = -\left(\frac{\partial \ln \omega_i}{\partial \ln V}\right)_p. \tag{12}$$

Since c_i is positive for all the modes at all temperatures, it is obvious that a volume NTE requires the negative values of the Grüneisen parameter for certain phonons being large enough to compensate for the normal positive values of all other phonons. By reformulating Eq. (12) and introducing the isothermal bulk modulus, the mode Grüneisen parameter can be expressed as the pressure-dependence of mode frequencies at constant temperature.

$$\gamma_i = \frac{B}{\omega_i}\left(\frac{\partial \omega_i}{\partial P}\right)_T. \tag{13}$$

The mode Grüneisen parameter can be determined by pressure-dependent phonon spectral methods at constant temperature, such as inelastic neutron scattering, Raman and infrared spectroscopy. For most materials, the mode frequencies usually increase with the increase of pressure, giving rise to positive Grüneisen parameters and hence a normal thermal expansion. Eq. (13) indicates that only those phonon modes which soften with increasing pressure have negative Grüneisen parameters and hence contribute to the NTE. The mode Grüneisen parameters provide an useful insight into the thermal expansion/contraction mechanisms.

2.4 NTE driven by acoustic phonon modes

Low frequency optical phonon modes with negative Grüneisen parameters associated with transverse displacements of bridging elements and coupled with rotations and distortions of connected polyhedra have been usually identified as the origins of NTE in framework structures. Nevertheless, the acoustic phonon modes driving NTE have been ignored in most of the studies, partially because of the difficulties in measuring them experimentally. In Fig. 3 we present a schematic model to illustrate the NTE driven by the acoustic modes in a one dimensional atomic chain and a two dimensional monolayer.

Figure 3(a) shows that both the transverse acoustic (TA) and longitudinal acoustic (LA) modes are able to make the length shorter along the chain direction when these modes are thermally activated. The TA mode has a more pronounced effect in driving the NTE than the LA mode due to the transverse displacements of atoms involved. In a 2D structure, collective out of plane vibrations of atoms will cause a shrinkage of the layer as shown in Fig. 3(b). This is also known as the membrane effect.

The acoustic mode associated with out of plane vibrations in a 2D material is named as the ZA mode. Theoretical simulations [39, 40] demonstrated that the acoustic modes are the dominate origins of NTE in 2D materials. In a framework structure, there exist both TA and LA modes which can be easily coupled with the rotations of corner-sharing polyhedra and contribute to the NTE. Two examples are given below to emphasize the importance of acoustic phonon modes in driving the NTE in framework structures.

Zn_2GeO_4 belongs to the rhombohedral phenacite structure, named after the mineral Be_2SiO_4 [41]. In the structure, GeO_4 and ZnO_4 tetrahedra (Zn is in two different crystallographic positions) are bridged by three coordinated oxygen atoms in a hexagonal unit cell. In contrast to other framework systems such as ZrW_2O_8 and $A_2M_3O_{12}$, where each bridge oxygen atom is shared by two polyhedra, each bridge oxygen atom in Zn_2GeO_4 is shared by three polyhedra and its transverse vibrations are largely restricted. From this sense, the NTE in Zn_2GeO_4 is not expected from the RUMs model or transverse vibrations of the bridge oxygen. Nevertheless, an NTE for Zn_2GeO_4 below room temperature was demonstrated by a dilatometer measurement [42] and confirmed by SXRD and NPD analyses [43], as shown in Fig. 4(a). EXAFS analysis suggests that the O3/O4 atoms in the four- and six-membered rings could have transverse displacements [Fig. 4(b)] and pressure-dependent Raman spectral measurement demonstrates negative Grüneisen parameters for some low frequency optical phonon modes (50–150 cm^{-1}). However, these negative Grüneisen parameters are not large enough to compensate for the positive ones for the occurring of NTE [43].

First principles calculations combined with the quasi-harmonic approximations (QHA) [44] demonstrate that the NTE in Zn_2GeO_4 is dominated by the TA phonon mode at the H point of the boundary of the first Brillouin zone and the LA phonon mode near the Γ point instead of the optical phonon modes. The largest (–30) and next largest (–15) Grüneisen parameters arise from the TA mode and the LA mode [Fig. 5(a)] though negative values also appear for some optical modes.

Figures 5(b)–(d) show the average amplitudes for different atoms for the two acoustic modes and the optical one with the third largest Grüneisen parameters. The two acoustic phonon modes are characterized by collective motions of Zn, Ge and O atoms. The TA mode passes across at least two unit cells in a vibration period and is clearly coupled with the rotations and distortions of the polyhedra as evidenced by the different amplitudes of vibration for different atoms. Whereas, the LA mode passes across more than ten unit cells in a period and all atoms within a unit cell move nearly in phase with same amplitude [Fig. 5(c)].

The acoustic phonon modes driving NTE was also demonstrated in cuprous halides (CuX, X=Cl, Br, and I) which form a zinc blend type fcc crystal lattice. In zinc blend structures, all atoms are tetrahedrally coordinated

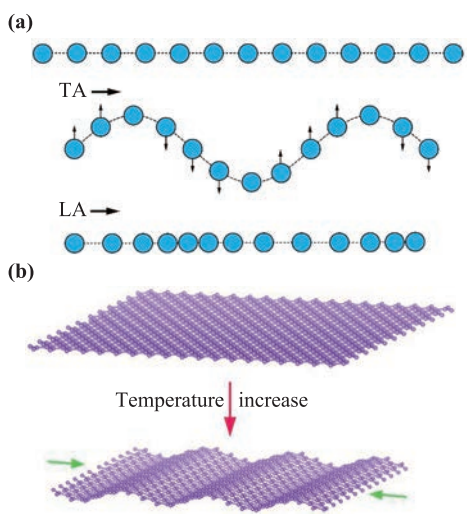

Fig. 3 Schematic illustration of acoustic modes causing NTE in **(a)** a linear chain and **(b)** 2D single layer.

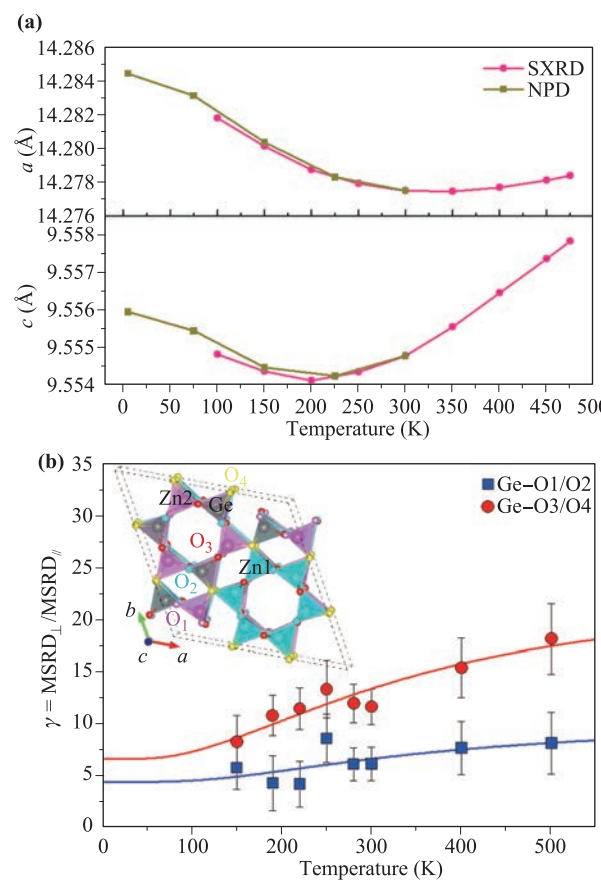

Fig. 4 **(a)** Lattice parameters vs. temperature in Zn_2GeO_4 from the refinement of the NPD and SXRD data. **(b)** Anisotropy ratio γ of Ge–O1/O2 and Ge–O3/O4 bonds [43].

and there are no linear links and no RUM-supporting polyhedral structural units can be identified. Experimental studies revealed negative thermal expansion behavior in cuprous halides at low temperatures [45]. An EXAFS study showed that the expansion of the Cu–Cl bond length is positive at all temperatures and the relative perpendicular vibrations for the Cu–Cl atomic pair are considered responsible for the NTE in zinc blende structures [46]. Nevertheless, the calculated mode Grüneisen parameters in all three compounds showed that the NTE in CuX is driven by the transverse acoustic modes which have negative Grüneisen parameters, instead of the optic modes whose Grüneisen parameters are positive [47].

The results above demonstrate that a proper description of NTE requires consideration of both the acoustic and optic phonon modes in the entire Brillouin zone. The presently structural analytical tools used derive only the local atomic displacements arising from anharmonic optical phonon vibrations and are unable to obtain the information of acoustic phonon modes.

2.5 Interplay between phonons and anisotropic elasticity

For an anisotropic solid there is a separate coefficient of thermal expansion for each independent strain coordinate. For the jth phonon mode at point $\boldsymbol{q}$ in the Brillouin zone, the directional Grüneisen parameter is defined as [48]

$$\gamma_{q,j,l} = -\frac{\partial \ln \omega_{q,j}}{\partial \ln l},\ l = a,\ b,\ c. \tag{14}$$

The directional "bulk" Grüneisen parameter is then defined as

$$\gamma_l = \frac{\sum\limits_{q,j} c_{q,j}(T)\gamma_{q,j,l}}{\sum\limits_{q,j} c_{q,j}(T)}, \tag{15}$$

where $c_{q,j}(T)$ is the mode specific capacity at temperature T. In terms of the elastic parameters and by analogous with Eq. (9), the directional thermal expansion is defined as a derivative under conditions of constant "thermodynamic tension" [49, 50]

$$\begin{aligned}\alpha_i(T) &= \frac{1}{V}\sum_l s_{i,l}\left\{\sum_{q,j} c_{q,j}\,(T)\,\gamma_{q,j,l}\right\}\\ &= \frac{1}{V}C_V(T)\sum_l s_{i,l}\gamma_l,\end{aligned} \tag{16}$$

where $s_{i,l}$ is an element of the elastic compliance tensor. The compressibility χ is given by the expression [51]

$$\chi = s_{11} + s_{22} + s_{33} + 2(s_{12} + s_{23} + s_{31}). \tag{17}$$

For a tetragonal structure, the linear CTEs along the a and c axes are written as (ignoring shear strains)

$$\alpha_a = \frac{1}{V}C_V(T)[(s_{11} + s_{12})\,\gamma_a + s_{13}\gamma_c], \tag{18}$$

$$\alpha_c = \frac{1}{V}C_V(T)(2s_{13}\gamma_a + s_{33}\gamma_c). \tag{19}$$

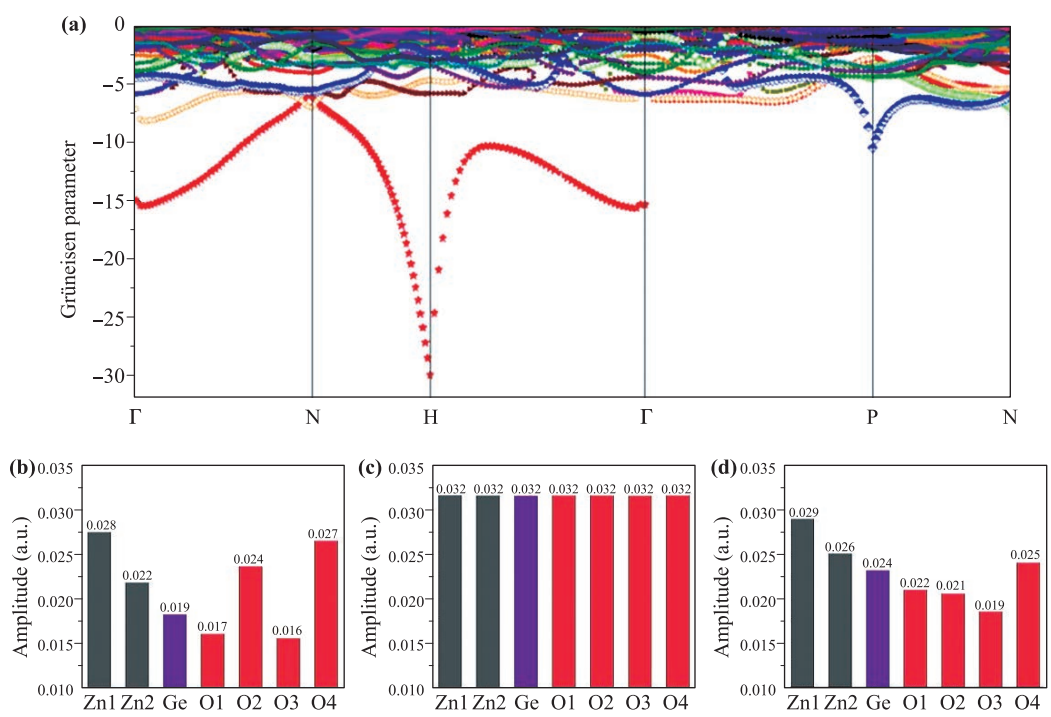

Fig. 5 **(a)** The calculated Grüneisen parameters along high symmetry directions of Zn_2GeO_4, **(b–d)** the average vibration amplitudes of the atoms for (b) TA mode at the H point, (c) LA mode at the point (0, 0, 0.03) near Γ point and (d) optical mode at the P point, respectively [44].

The volume CTE for a tetragonal phase becomes

$$\alpha_V = 2\alpha_a + \alpha_c = \frac{1}{V}C_V(T)[2\left(s_{11}+s_{12}+s_{13}\right)\gamma_a + \left(s_{13}+s_{33}\right)\gamma_c]. \quad (20)$$

Eqs. (18)–(20) indicate that anisotropic thermal expansion is controlled by the interplay between phonons and the elastic anisotropic elasticity (compliance matrix). Negative mode Grüneisen parameters might not be a necessary condition for both axial and volume NTE for anisotropic materials since the elastic compliance $s_{i,l}$ might be positive or negative. The extent of NTE is determined by two key ingredients: the presence of soft phonon modes (have negative Grüneisen parameters) that drive contraction; and anisotropic elastic compliance that predisposes the material to the deformations required for NTE along a specific axis. A volume NTE for the tetragonal structure requires

$$2\left(s_{11}+s_{12}+s_{13}\right)\gamma_a + \left(s_{13}+s_{33}\right)\gamma_c < 0. \quad (21)$$

By analogous of Eqs. (19) and (20), one can obtain the axial CTEs for hexagonal and orthorhombic structures. A first-principles theory study by Ritz and Benedek [23] shows that NTE in $PbTiO_3$ involves a delicate interplay between the phonon properties of a material (Grüneisen parameters) and its anisotropic elasticity. The interplay between the phonons and the anisotropic elasticity seems also evident in the axial CTEs of $Sc_2Mo_3O_{12}$ and $Sc_2W_3O_{12}$ [6].

3 NTE in framework structures

3.1 AM_2O_8

This group of materials includes cubic ZrW_2O_8 [2], cubic HfW_2O_8 [52], $ZrMo_2O_8$ [53] and $HfMo_2O_8$ [54]. They have an open framework structure in which each MO_4 tetrahedron shares three of its four oxygen atoms with adjacent AO_6 octahedra and exhibit NTE over a wide range of temperature up to 1050 and 600 K for tungstates and molybdates, respectively. ZrW_2O_8 and HfW_2O_8 undergo an order-disorder transition at about 440 K and 468 K, respectively, from their metastable, low-temperature cubic phase with a linear CTE of $\sim -9\times10^{-6}$ K^{-1} to a metastable, high temperature cubic phase with a linear CTE of $\sim -5\times10^{-6}$ K^{-1}. Both $ZrMo_2O_8$ and $HfMo_2O_8$ adopt the high temperature structure of ZrW_2O_8 and therefore a lower NTE.

The mechanism of NTE in open network structures was attributed to large transverse thermal motion of oxygen atoms in the M-O-M linkages, which is in coorperative with librations of undistorted polyhedra [2, 55]. RUMs were suggested to associate with the NTE in ZrW_2O_8 [32, 56], However, X-ray-absorption fine-structure (XAFS) [57, 58], X-ray pair distribution function (XPDF) and EXAFS [59] analyses indicated that the Zr–O–W linkages are relatively stiff and do not permit bending of the Zr–O–W links. The NTE effect in ZrW_2O_8 is attributed to correlated translations of the WO_4 tetrahedra and rotations of ZrO_6 octahedra, instead of primarily suggested transverse vibrations of the bridging O atoms.

All the experiments by Raman [60, 61] and infrared [62] spectroscopy demonstrate that the low frequency optical phonons involving the transverse oxygen motions associated with libration provide NTE. First principles calculations [63, 64] have also identified that the lowest energy optic modes involving in-phase translation and bending of the WO_4 and ZrO_6 networks and out-of-phase translation of WO_4 and ZrO_6 in two chains contribute the most to NTE in α-ZrW_2O_8. The nature of these modes exhibits features characteristic of both the rigid unit modes and the tent models. The theoretical studies are qualitatively in agreement with the experimental results and both show that the anharmonicity of low-energy phonon modes has a major contribution to the observed thermal expansion behavior. However, the calculated CTE deviates largely from the experimental values and this is particularly serious at high temperatures [63].

3.2 AV_2O_7

ZrV_2O_7 [65] and HfV_2O_7 [66] consist of ZrO_6 (HfO_6) octahedra and VO_4 tetrahedra. In this structure each AO_6 octahedron shares corners with six VO_4 tetrahedra, and each VO_4 tetrahedron shares corners with three AO_6 octahedra and one other VO_4 tetrahedron. At room temperature, the two compounds crystallize in a $3\times3\times3$ superstructure with space group of $Pa\overline{3}$ but undergo two successive phase transitions around 350 K and 375 K for ZrV_2O_7 and 320 K and 370 K for HfV_2O_7, with large volume expansion with increasing temperature (2.4×10^{-5} K^{-1} and 2.5×10^{-5} K^{-1}, for ZrV_2O_7 and HfV_2O_7, respectively). The intermediate phase between the phase transitions has an incommensurate structure [67]. Above the second phase transition temperature they adopt a $1\times1\times1$ normal cubic structure with space group $Pa\overline{3}$ and display isotropic NTE [65, 66]. In the superstructure, 89% of the V–O–V linkages are bent to about 160° but 11% remain on three-fold axes and are therefore constrained by symmetry to be 180° on average, whereas all V–O–V angles are 180° on average in the parent cubic structure [65]. It was recently found for ZrV_2O_7 that the phase transition shifts progressively to high temperatures by compression and the high temperature NTE phase is about twice as stiff as its low temperature superstructure [68].

As mentioned above, ZrV_2O_7 and HfV_2O_7 exhibit isotropic NTE only above ~375 K. The high phase transition temperature hinders its practical applications. Many groups have made efforts to tailor the structural phase

transition temperature for ZrV_2O_7, including single site substitution of P or Mo or W for V or Hf for Zr [74] or dual site substitutions of (Nb, Y) for Zr and P for V [75] and Cu/P [76] or Fe/P [77] or Hf/P [78, 79] and Al/Mo [80], Fe/Mo [81] for Zr/V, etc. It is noticed that these substitutions were more or less effective in reducing the phase transition temperature and suppressing the positive and negative CTEs to some extent, but few have succeeded in extending the NTE to well below RT. Even in some cases, the cubic structure could not be maintained, such as in the cases of W-substituted [67] and Fe/Mo co-substituted [76] ZrV_2O_7.

Recently a facile method for realizing NTE property of ZrV_2O_7 to cover a wide temperature range involving RT by breaking the superstructure of ZrV_2O_7 via partial substitution of Mo for V atoms was reported [82]. It was found that the incorporation of Mo prompts the V–O2–V/Mo angles to expand from 160° to 180°, which enables the NTE property to extend to lower than the room temperature. The onset of the NTE was reduced to 250 K and 225 K for $ZrV_{1.7}Mo_{0.3}O_{7+\delta}$ and $ZrV_{1.5}Mo_{0.5}O_{7+\delta}$, respectively. $ZrV_{1.5}Mo_{0.5}O_{7+\delta}$ retains a near-zero thermal expansion below 225 K, as shown in Fig. 6.

Mittal and Chaplot [83] performed lattice dynamical calculations for ZrV_2O_7 and HfV_2O_7 and found that the phonon modes of energy from 4 to 7 meV are major contributors to NTE. These phonon modes involve translations and librations of ZrO_6 octahedral and VO_4 tetrahedral units, which significantly soften on compression of the lattice and lead to the thermal shrinkage. However, pressure-dependent Raman scattering studies revealed pressure-induced phase transition and amorphization at 0.36 and 3.5 GPa for $x = 0.3$, respectively. As shown in Fig. 7, the pressure-dependent behaviors of the phonon modes in ZrV_2O_7 are quite different from those in ZrW_2O_8 where most of the low frequency phonon modes soften on compression. In ZrV_2O_7 most of low frequency phonon modes harden whereas a number of high frequency phonon modes soften on compression, suggesting different NTE mechanisms in the two systems. The lowest optical frequency mode at about 189 cm^{-1} involving translational and librational vibrations of ZrO_6 octahedra and VO_4 tetrahedra and the asymmetric stretching vibrations of the V/Mo–O bonds have negative Grüneisen parameters and contribute to the NTE of $ZrV_{2-x}Mo_xO_{7+\delta}$. That some high energy optical phonon modes soften on compression and have negative Grüneisen parameters is not limited to ZrV_2O_7 but also found in ZrW_2O_8 [60], $Al_2Mo_3O_{12}$ [84], $HfMgW_3O_{12}$ [85], etc. The role of high energy optical phonon modes played in NTE needs to be further investigated.

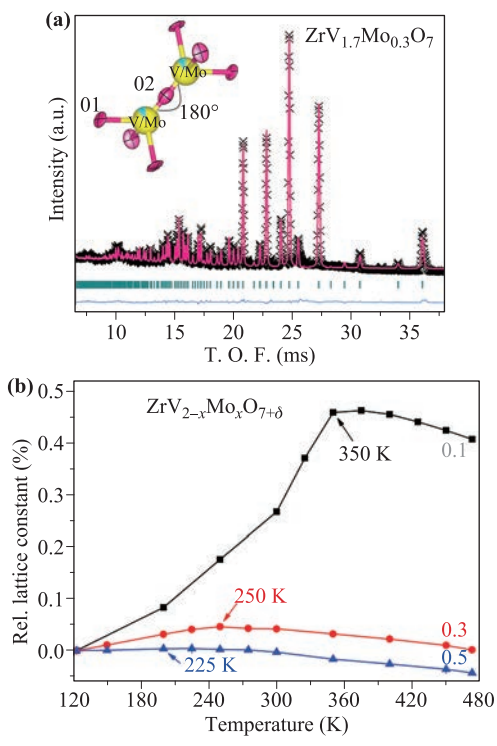

Fig. 6 **(a)** Structure refinement of $ZrV_{1.7}Mo_{0.3}O_7$ from neutron powder diffraction data obtained at 300 K. **(b)** relative lattice constants changes of $ZrV_{2-x}Mo_xO_{7+\delta}$ (x = 0.1, 0.3, and 0.5) at different temperatures obtained by XRD [82].

3.3 $Cu_2M_2O_7$

$Cu_2V_2O_7$ crystallizes in at least three different polymorphs, namely orthorhombic α, monoclinic β, and triclinic γ phases, according to the chemical composition [86–88]. The α phase is orthorhombic (space group $Fdd2$) with lattice parameters a =20.645 Å, b =8.383 Å, and c =6.442 Å. Each Cu ion is surrounded by five oxygen atoms, forming CuO_5 polyhedra. The chains made of CuO_5 polyhedra are separated by $(V_2O_7)^{4-}$ anion groups, consisting of corner-sharing VO_4 tetrahedra. The β phase is monoclinic (space group $C2/c$) with lattice parameters a =7.718 Å, b =8.044 Å, c =10.140 Å, and β =110.3°. The Cu^{2+} cations have again a fivefold oxygen coordination. The β phase is obtained from the α phase by rotating the V_2O_7 groups and shifting the planes of VO_4 tetrahedra. Both the stable α-phase and β-phase were reported to exhibit NTE recently.

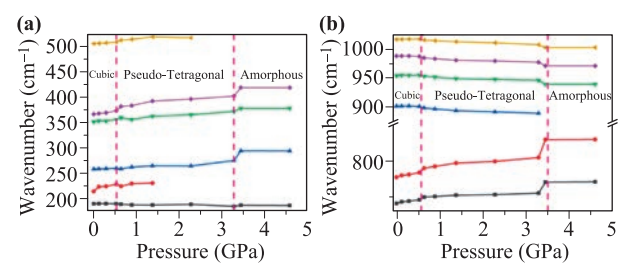

Fig. 7 Raman mode shifts in $ZrV_{1.7}Mo_{0.3}O_{7+\delta}$ with pressure: **(a)** low frequency modes and **(b)** high frequency modes [82].

Large uniaxial NTE along the b-axis and a volume contraction below 573 K in α-$Cu_2V_2O_7$ was reported by Zhang *et al.* [3]. Figure 8(a) shows the thermal expansion properties reported by Katayama *et al.* [89]. Subsequent studies demonstrate that the NTE in α-phase can be extended at least to 10 K in the low temperature range [90] but with a pronounced lattice change anomaly across $T_N = 34 \pm 1$ K. Recently, Shi *et al.* [91] reported a series of orthorhombic α-$Cu_{2-x}Zn_xV_2O_7$ ($x = 0, 0.1, 0.2$), in which the volumetric CTEs are successfully tuned from -10.19×10^{-6} K^{-1} to -1.58×10^{-6} K^{-1} in the temperature range of 100–475 K by increasing content of Zn^{2+}. By Rare-earth doping with 5% Yb, Sm, or Ce, the orthorhombic α-phase and hence volume NTE characteristics are maintained [92].

Joint SXRD and EXAFS analyses revealed that the transverse vibrations of oxygen bonded with vanadium and coupled rotations of the non-rigid polyhedra bring the shrinkage of the bc plane and account for the anisotropic NTE in α-$Cu_2V_2O_7$. Nevertheless, there exist giant ferroelectric polarization and large magnetoelectric coupling in the magnetically ordered phase of α-$Cu_2V_2O_7$ and spin, charge and structural degrees of freedom which contribute significantly to the entropy changes are driving the ordered state [93]. Considering ferroelectric instability and magnetic ordering, the underlying mechanisms of NTE in α-$Cu_2V_2O_7$ needs to be further studied.

The monoclinic β-phase has a different NTE behavior from the α-phase as shown in Fig. 8(b). It is shown that both a- and c-axis contract and the b-axis expands in the whole temperature range studied [94]. The CTEs in a-, b- and c-axis are $\alpha_a = -20.92\times10^{-6}$ K^{-1}, $\alpha_b = 20.93\times10^{-6}$ K^{-1}, and $\alpha_c = -7.76\times10^{-6}$ K^{-1}, respectively, from 323 to 573 K, giving rise to a volume contraction of $\alpha_V = -2.74\times10^{-6}$ K^{-1} (153–323 K) and $\alpha_V = -10.71\times10^{-6}$ K^{-1} (323–573 K). The underlying mechanism of the NTE of β-$Cu_2V_2O_7$ was suggested to involve the coupling effect of the tetrahedron caused by the lateral vibration of the bridge oxygen atoms and tensile effect of the tetrahedron.

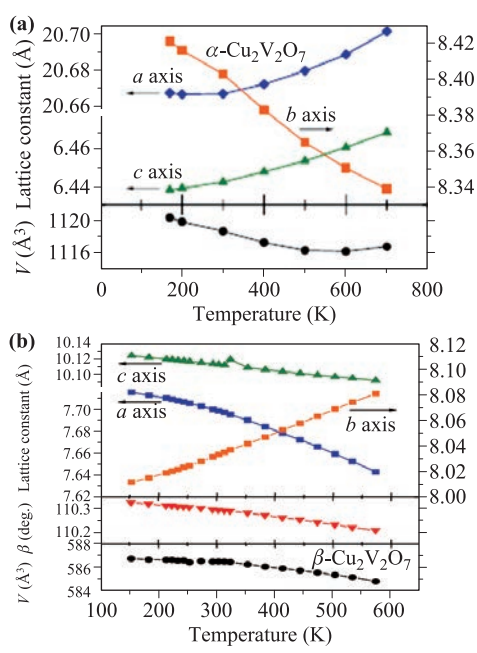

Fig. 8 Temperature dependence of crystallographic parameters of α-$Cu_2V_2O_7$ **(a)** [89] and β-$Cu_2V_2O_7$ **(b)** [94].

By substitution of Zn and Mg for Cu in $Cu_2V_2O_7$, the $Cu_{1.8}Zn_{0.2}V_2O_7$ [89, 94] and $Cu_{1.5}Mg_{0.5}V_2O_7$ [95] retain the β-phase and exhibit NTE with the linear CTE $\alpha_l = -14.4\times10^{-6}$ K^{-1} and -8.72×10^{-6} K^{-1} by dilatometry measurements, respectively, over a wide temperature range from 100 K to 700 K, which is about 2.6 and 3.9 times larger than the intrinsic lattice linear contraction, confirming the microstructural effects similar to that found in layered ruthenium oxides [96–98] .

Recently the α-$Cu_2P_2O_7$ (space group $C2/c$) has been found to exhibit strong NTE along the a- and b-axis ($\alpha_V \sim -27.69\times10^{-6}$ K^{-1}, 5–375 K) by Shi *et al.* [5]. The coupling twist and rotation of PO_4 and CuO_5 polyhedra are identified as the inherent factors for the NTE nature of $Cu_2P_2O_7$, which is triggered by the transverse vibrations of oxygen atoms. α-$Cu_2P_{2-x}V_xO_7$ was also synthesized and shown to exhibit comparable coefficients of NTE but with extended temperature range ($a_V = -18.36\times10^{-6}$ K^{-1}, 173–673 K for Cu_2PVO_7).

3.4 $A_2M_3O_{12}$-based compounds

Due to the chemical flexibility and NTE over wide temperature range, the $A_2M_3O_{12}$-based compounds (A = transition metal or rare earth, M = W or Mo) constitute a large family of NTE materials and have received considerable attention. In this structure, each AO_6 octahedron shares its six corners with MO_4 tetrahedra and each Mo_4 tetrahedron shares all its corners with AO_6 octahedra. These materials crystallize either in an orthorhombic or monoclinic symmetry at room temperature depending on the "A" cation size but only the orthorhombic corner shared polyhedral network shows significant NTE behavior. Those with smaller A^{3+} cation size or larger electronegativity (A = Al, Fe, Cr, In) crystalize in a monoclinic structure at RT and exhibit NTE only after monoclinic to orthorhombic phase transition at higher temperatures [99–103].

3.4.1 ABM_3O_{12}

The chemical flexibility of $A_2M_3O_{12}$ and NTE in a wide temperature range offers an excellent opportunity for new materials design with desired properties. It was demonstrated that the A^{3+} cation in $A_2M_3O_{12}$ can be replaced by divalent and tetravalent ions. With this strategy, series of materials with low NTE or near-zero CTE have been developed in recent years including $HfMgW_3O_{12}$ [104], $HfMgMo_3O_{12}$ [105], $ZrMgMo_3O_{12}$ [106], $ZrMgW_3O_{12}$ [107], $ZrMnMo_3O_{12}$ [108]

and $HfMnMo_3O_{12}$ [109]. All these materials show low positive or negative thermal expansion with near-zero linear CTE.

3.4.2 ABM_2XO_{12}

By taking the advantage of chemical flexibility, novel materials with excellent NTE property covering large temperature range have been designed recently. This includes $ZrScMo_2VO_{12}$ [4], $ZrScW_2PO_{12}$ [110], $HfScMo_2VO_{12}$ [111], $HfScW_2PO_{12}$ [112], $ZrFeMo_2VO_{12}$ [113], $Sc_2W_4O_{15}$ [114], and $(HfSc)_{0.83}W_{2.25}P_{0.83}O_{12-\delta}$ [115], etc. It is demonstrated that $AScM_2XO_{12}$ (A = Zr, Hf; M = W, Mo; X = V, P) exhibit excellent NTE property in a very large temperature range (~100–800 K for those containing Mo/V and 100–1473 K for those containing W/P) without hygroscopicty. Besides the NTE property, they were found to have strong photoluminescence (PL) covering the visible range, suggesting the potential for LED applications.

The mechanisms of NTE have been studied by first-principles calculations for $Y_2Mo_3O_{12}$ [116] and $Zr_{0.3}Sc_{1.7}Mo_{2.7}V_{0.3}O_{12}$ [117]. The results show that most of the optical phonon modes below 150 cm^{-1} have negative Grüneisen parameters and contribute to the NTE. The lowest optical phonon modes involving translational motions of the bridge O atom in a A–O–M linkage, coupled with the rotation and distortion of the AO_6 octahedron and MO_4 tetrahedron have the largest negative Grüneisen parameters and account for a large part of the NTE behavior (Fig. 9). Recent *ab initio* lattice dynamical calculations for the orthorhombic $Sc_2(MoO_4)_3$ and $Sc_2(WO_4)_3$ showed that phonon modes involving translation, libration, and distortion of ScO_6 and MoO_4 units at about 6 meV significantly contribute to the NTE [6].

3.5 AMO_5

AMO_5 (A = Nb, Ta; M = P, V) are framework structured compounds that exhibit NTE in their high temperature phase. $NbPO_5$ crystallizes in a monoclinic (space group $P2_1/c$) or a tetragonal (space group $P4/n$) structure at ambient conditions. Both are based on NbO_6 octahedra and PO_4 tetrahedra, which share corners to form three-dimensional networks. The tetragonal $NbOPO_4$ undergoes a phase transition to $P4/nmm$ at about 473 K. All cell edges showed positive thermal expansion below the transition, but NTE was observed for the a and b axes above the transition. The monoclinic $NbPO_5$ undergoes a reversible first order transition to orthorhombic phase (Space group $Pnma$) above 565 K. One cell edge shows NTE over the entire temperature range while the other two cell edges show NTE only above the phase transition. The NTE behavior is attributed to the rocking motions of corner-shared NbO_6 octahedra and PO_4 tetrahedra [118] or related to transverse thermal motions of oxygen [119].

$TaVO_5$ adopts a monoclinic symmetry with space group $P2_1/c$ at low temperatures and transforms to an orthorhombic symmetry with space group $Pnma$ above 259 K. $TaVO_5$ is reported to have NTE behavior in all the axes above room temperature till 1073 K [120]. $NbVO_5$ adopts also orthorhombic structure at ambient conditions [121]. The volume CTEs for $TaVO_5$ and $NbVO_5$ were reported to be -8.92×10^{-6} K^{-1} and -6.63×10^{-6} K^{-1}, respectively, from RT to 873 K.

Pressure dependent Raman and *ab initio* calculations showed that not only the modes related to coupled rotations of TaO_6 octahedra and VO_4 tetrahedra, but also those related to bending motions and the stretching vibrations have negative Grüneisen parameters and contribute to NTE in $TaVO_5$, suggesting that the NTE in $TaVO_5$ is due to the rotations of TaO_6 octahedra and VO_4 tetrahedra accompanied by distortion of VO_4 tetrahedra [122]. A pressure−temperature phase diagram of $TaVO_5$ is presented by Salke *et al.* [123]. Pressure-dependent Raman investigation shows that orthorhombic $TaVO_5$ undergoes transition to monoclinic phase and amorphization at 0.2 and 8 GPa, respectively [123].

3.6 Cu_2O and Ag_2O

The cuprite structure (Ag_2O and Cu_2O, space group $Pn\bar{3}m$) can be described as a framework of two interpenetrating but independent networks of corner-sharing M_4O tetrahedra (M = Ag, Cu), in which each Matom is linearly coordinated to two O atoms, and each O atom is tetrahedrally coordinated to four Matoms. Negative thermal expansion of the cell parameter has been observed from 5 to about 200 K for Cu_2O [124] and up to 470 K for Ag_2O [125].

EXAFS measurements for the Ag–O and Ag–Ag distances in Ag_2O [126] suggest that the NTE is a result of competition between the Ag–O bond expansion and Ag–Ag distance contraction. The *ab initio* calculations identified the bending motions of the Ag_4O tetrahedra having the maximum negative Grüneisen parameter as major contributor to NTE [127]. It is argued that the rigid unit modes and the bending modes of the Ag_4O tetrahedra play key roles in NTE at low temperatures and the NTE at temperatures above 250 K is caused by strong interactions of O-dominated modes with Ag-dominated modes [128].

Though the results from EXAFS analyses indicate that the tetrahedral units in Ag_2O and Cu_2O are lack of rigidity and consequently inadequacy of a RUM model, Rimmer *et al.* [35] argued that the NTE in Cu_2O can be described as being driven by RUMs, but with the rigid unit recast as an O–Cu–O rod. They characterized the NTE mechanism in Cu_2O via mapping of different Cu_2O structural flexibility models onto phonons obtained using *ab initio* lattice dynamics. It was proposed that low-frequency acoustic modes that are responsible for the NTE in this material correspond to vibrations of rigid O–Cu–O rods. There is also some small contribution from higher-

frequency optic modes that correspond to rotations of rigid and near-rigid OCu_4 tetrahedra as well as of near-rigid O–Cu–O rods. The intense transverse thermal motion of the metallic atom with respect to the O–M–O direction should be directly connected with the origin of NTE.

3.7 $A_2O(PO_4)_2$

Dithorium oxide phosphate $Th_2O(PO_4)_2$ and $U_2O(PO_4)_2$ adopt an orthorhombic structure (space group *Cmca*). Both are isotypic with the orthorhombic high-temperature (β) form of $Zr_2O(PO_4)_2$. In these compounds, the tetravalent cation (MIV) adopts a seven-fold coordination. They all display NTE along the *b*-axis (-3.6×10^{-6} K^{-1}, -7.4×10^{-6} K^{-1} and -11.1×10^{-6} K^{-1}, RT-1223K) and linear CTE of 1.5×10^{-6} K^{-1}, -1.4×10^{-6} K^{-1} and -1.6×10^{-6} K^{-1} for $Zr_2O(PO_4)_2$, $Th_2O(PO_4)_2$ and $U_2O(PO_4)_2$, respectively [129].

3.8 ScF_3 and related materials

Scandium trifluoride contains a simple network of corner-sharing ScF_6 octahedra and was found to display NTE across a wide range of temperature [11]. Subsequently, NTE behavior was observed for $CaZrF_6$, $CaHfF_6$ [12] and $MgZrF_6$ [130], $CaNbF_6$ [13] and $CaTiF_6$ [131]. By comparing the inelastic neutron scattering measurements with the frozen phonon calculations for ScF_3, Li *et al.* [36] demonstrated that some of the modes with motions of F atoms transverse to their bond direction around 25 meV stiffen with the temperature. The quartic potential that originates from harmonic interatomic forces accounts for phonon stiffening with the temperature and a significant part of NTE in ScF_3. By deriving a real-space model of atomic motion in ScF_3 from total neutron scattering data, Dove *et al.* [132] showed that NTE in this material depends not only on rigid unit modes, but also on modes that distort these octahedra. They demonstrated that anharmonicity in the form of quartic terms involving individual modes does not significantly affect the distribution of atomic displacements, suggesting that NTE can be understood within the context of the traditional quasi-harmonic approximation when taking account of quartic anharmonicities through phonon renormalization, rather than through the effect on the intrinsic energy of certain individual phonon modes. By performing a set of anharmonic free-energy calculations based on density functional theory, Oba *et al.* [133] showed that the contribution from the cubic anharmonicity to the vibrational free energy, evaluated by the improved self-consistent phonon theory, is significant and as important as that from the quartic anharmonicity for robust understandings of the temperature dependence of the thermal expansion coefficient. The origin of the NTE in ScF_3 was explained by the interplay between expansion and rotation of ScF_6 octahedra by Bocharov *et al.* using *ab initio* molecular dynamics simulations in the isothermal-isobaric ensemble [134].

Recent *ab initio* lattice dynamical studies on the metal fluorides ($CaZrF_6$, $MgZrF_6$, and $SrZrF_6$) [135] show that

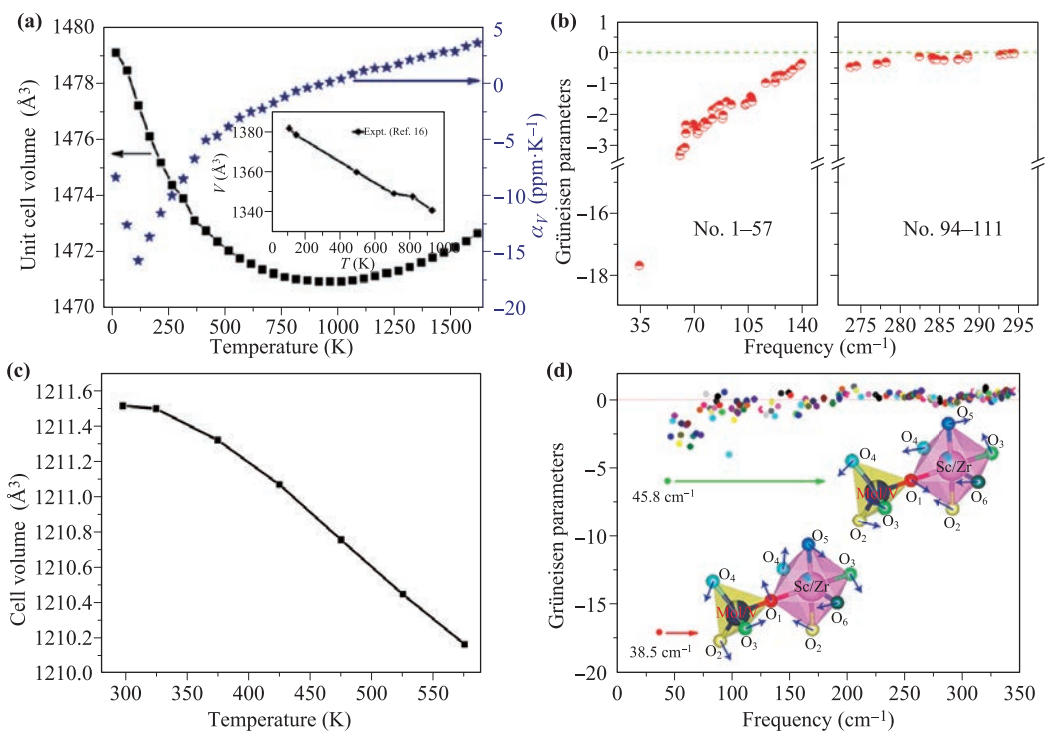

Fig. 9 Negative thermal expansion and calculated Grüneisen parameters for $Y_2Mo_3O_{12}$ [116] and $Zr_{0.3}Sc_{1.7}Mo_{2.7}V_{0.3}O_{12}$ [117].

the phonon modes involving ZrF_6 polyhedral rotational motions lead to large transverse amplitude of the vibrations of the fluorine atom in the Zr-F-M bond (Fig. 10). These modes have large negative Grüneisen parameters and are responsible for the NTE in these materials.

By using a symmetry-motivated approach to analyzing X-ray pair distribution functions (PDF), Bird *et al.* [136] studied the mechanism of NTE in ScF_3 and $CaZrF_6$ and concluded that it is the flexibility of M–F–M linkages (M = Ca, Zr, Sc) due to dynamic rigid and semirigid "scissoring" modes that facilitate the observed NTE behavior. The amplitudes of these dynamic distortions correspond well with the experimentally observed magnitudes of the thermal expansion, which is larger for $CaZrF_6$ than for ScF_3.

It might be concluded that the MF_6 octahedral rotations make a significant contribution to the NTE in ScF_3 and $MZrF_6$ but higher order (cubic and quartic) anharmonicities must be included to correctly understand the NTE behaviors of these materials. Since first-principles calculations using the quasiharmonic approximation (QHA) only accounts for the volume dependence of phonon frequencies and neglects higher-order anharmonicities, most of them could not match the experimental values of CTE, particularly at high temperatures. In fact, cubic anharmonicity is observed to dominate the higher-frequency A_g phonon-mode, and quartic anharmonicity is found to dominate the lower-frequency F_{2g} phonon-mode by Raman measurements [137]. The strong contribution of the explicit anharmonicity indicates that the large NTE of $CaZrF_6$ cannot be accurately predicted through the quasi-harmonic approximation. The improved phonon theoretical calculations involving higher order anharmonicities are necessary for the phonon modes with large anharmonicities.

Cubic ReO_3 is isostructure of ScF_3 but its NTE is much smaller and in a much narrower temperature range (<200 K). The structure consists of corner-linked ReO_6 octahedra with Re at the centers. ReO_3 was found to exhibit NTE in two temperature ranges: 2–220 K and 600–680 K. From about 220 K to about 600 K the thermal expansion becomes positive [138]. The NTE of ReO_3 at low temperatures was ascribed to the negative Grüneisen parameter of the zone boundary $M3$ phonon mode representing the antiphase rotation of the neighboring ReO_6 octahedra. The origin of the second NTE range is not yet understood but may possibly be related to anomalous behavior of the $M3$ phonon mode. The smaller NTE in ReO_3 was attributed to the much stiffer Re–O bond which is harder to bend and less flexible than the Sc–F bond [139].

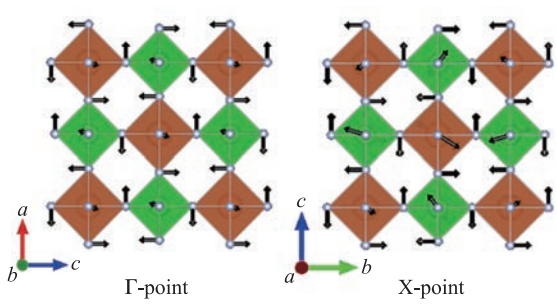

Fig. 10 The displacement pattern of typical phonon modes having a large negative Grüneisen parameter at Γ (0 0 0) and (1 0 0) points in the Brillouin zone [135].

3.9 Cyanides and Prussian blue analogues

Cyanides $M(CN)_2$ (M = Zn, Cd, Cu, Ni) [7] and many Prussian blue analogues [8–10, 140–142] were found to display either isotropic or anisotropic NTE. A common feature for these materials is that they have M–C ≡ N–M′ linkages.

$Zn(CN)_2$ and $Cd(CN)_2$ exhibit large isotropic NTE in the temperature range of 25–375 K [7]. First-principles calculations based on density functional theory [143] showed that the transverse translational modes (the C and N atoms vibrating in the same direction perpendicular to the M–C ≡ N–M linkages) and the librational modes (the C and N atoms vibrating in the opposite direction) give rise to negative Grüneisen parameters and therefore contribute to the NTE. Figure 11 shows the translational and librational modes which contribute most to the NTE [144]. Both motions of the hard −C ≡ N− bond have the same effect of drawing the anchoring metal atoms closer. This conclusion is supported by total neutron diffraction measurements [145], which demonstrate that the principal motions giving rise to NTE are those in which the carbon and nitrogen atoms within individual M–C ≡N–M linkages are displaced to the same side of the Zn···Zn axis. Displacements of the carbon and nitrogen atoms to opposite sides of the Zn···Zn axis make smaller contributions. Similarly, the mechanism of NTE in $ZnAu_2(CN)_4$ is identified in terms of specific anharmonic phonon modes that involve bending of the –Zn–NC–Au–CN–Zn– linkage [146].

Besides optical phonons, acoustic phonons may also contribute to the NTE effect. Inelastic neutron scattering revealed a lowest-energy peak near 2 meV (∼16 cm^{-1}) which has also a negative Grüneisen parameter. *ab initio* lattice dynamical calculations by Mittal *et al.* [147] and molecular dynamics simulations by Fang *et al.* [148] indicate that the acoustic phonon modes of energy ∼2 meV are major contributors to the NTE in $Zn(CN)_2$. The TA modes corresponding to collective motions of Zn–CN–Zn as a rigid body without involving relatively high-energetic angle bending in the linkage, have the most negative Grüneisen parameters and hence contribute half of the NTE of the material. The optic modes corresponding to rotations of the neighboring tetrahedral units against each other involving angle bending in the Zn–CN–Zn linkage have less negative Grüneisen parameters.

$Ni(CN)_2$ has a layered structure consisting of Ni^{2+}-

centered corner sharing square-planar units. This leads to 2D NTE in the plane of the layers with $\alpha_a = -65 \times 10^{-6}$ K^{-1}, where $a = b$ is the in-plane lattice parameter, and a positive thermal expansion perpendicular to the layers resulting in an overall positive volume expansion, $\alpha_V = +48 \times 10^{-6}$ K^{-1} [149]. The mechanism of NTE in $Ni(CN)_2$ was considered to be similar as in $Zn(CN)_2$ [143].

Replacing half of the Ni^{2+} ions with Cu^{2+} to form $CuNi(CN)_4$ results in an isostructural compound with a smaller interlayer separation and more pronounced 2D NTE [$\alpha_a = -97(8) \times 10^{-6}$ K^{-1}] [150]. Analysis of mode Grüneisen parameters and eigenvectors [151] reveals that the most NTE-inducing phonons include a large deformation of the $[CuN_4]$ units, while the $[NiC_4]$ units move as a rigid entity. This type of deformation allows for greater out-of-plane motion of the N atoms. As these motions were not found in previous studies of $Ni(CN)_2$, they are believed to be the reason for the enhanced NTE in $CuNi(CN)_4$ with respect to $Ni(CN)_2$.

While the parent cubic $Zn(CN)_2$ and layered $Ni(CN)_2$ exhibit respectively 3D and 2D NTE, the $ZnNi(CN)_4$, a 3D framework consisting of two interpenetrating networks, in which ZnN_4 tetrahedra are linked by square-planar NiC_4 units, was predicted to exhibit pronounced anisotropic NTE ($\alpha_a = -21.2 \times 10^{-6}$ K^{-1}; $\alpha_b = +14.6 \times 10^{-6}$ K^{-1}; $\alpha_c = -26.95 \times 10^{-6}$ K^{-1}) [9]. Analysis of the mode eigenvectors and Grüneisen parameters show that although low-energy phonons with RUM-like character do contribute to the NTE, twisted transverse motions, which are not present in $Zn(CN)_2$, and play a more significant role in the NTE of $ZnNi(CN)_4$.

More recently, several Prussian blue analogous such as

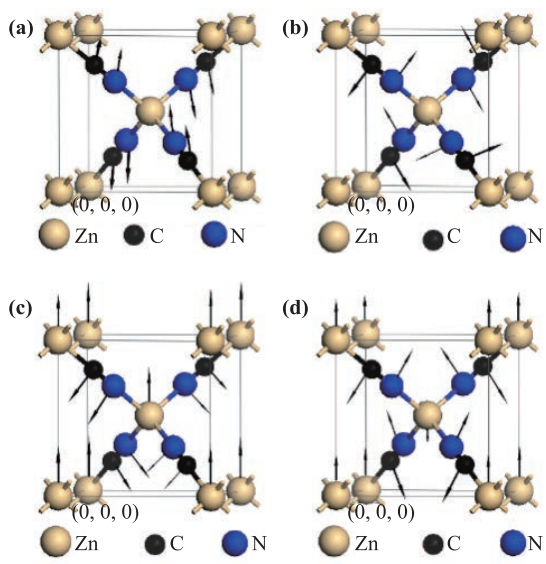

Fig. 11 Translational **(a, c)** and librational **(b, d)** modes contributing most to the NTE in $Zn(CN)_2$: (a) 47 cm ($\gamma = -22.7$), (b) 263 cm ($\gamma = -2.52$), (c) 189 cm ($\gamma = -1.1$) and (d) 356 cm ($\gamma = -0.86$) [143].

$AgB(CN)_4$, $CuB(CN)_4$ [10], and $ScCo(CN)_6$ [142] with large isotropic NTE in a wide temperature range were discovered. The CTEs for $AgB(CN)_4$ is $\alpha_V = -40 \times 10^{-6}$ K^{-1} (100–600 K) and $\alpha_V = -20 \times 10^{-6}$ K^{-1} (25−600 K). The analysis by EXAFS and first-principles calculation indicate that the NTE driving force comes from the transverse vibrations of bridge chain atoms of C and N, corresponding to the low-frequency phonon modes. The same transverse vibration direction of C and N atoms is a key factor for the occurrence of strong NTE in these and related compounds [152, 153].

$Si(NCN)_2$ was also found to display isotropic NTE with $\alpha_V = -3.72 \times 10^{-6}$ K^{-1} at 500 K and $\alpha_V = -5.79 \times 10^{-6}$ K^{-1} at 1123 K [154]. The transverse and librational displacements of the –N=C=N– units in the Si–N=C=N–Si linkages were found to be essential for the NTE in $Si(NCN)_2$ [155].

3.10 MOFs

MOFs are metal organic frameworks constructed from inorganic metal nodes and connected with organic ligands. Due to inherent structure flexibility, MOF compounds also readily display NTE. Cubic structure MOF-5 was reported to exhibit isotropic NTE with a linear thermal-expansion coefficient of $\alpha_l = -16 \times 10^{-6}$ K^{-1} from 4 to 600 K [156–158]. The NTE was attributed to the transverse vibration of the ligands (phenyl ring) perpendicular to the linkage Zn_4O–BDC–Zn_4O and the rotation of metallic clusters, which has the effect of pulling the anchoring ZnO_4 clusters closer [159, 160].

The NTE behavior has also been found in several other MOFs [161–163]. Orthorhombic MIL-68(In) was reported to exhibit anisotropic NTE. A SXRD and high-energy SXRD scattering studies demonstrate that the transverse vibration of the phenyl ring leads to the NTE in the *ab* plane while the rotation of rigid octahedrons gives rise to the contraction along the *c*-axis [164].

As a novel class of nanoporous materials, MOFs have attracted considerable interest owing to their structural diversities and wide applications, such as gas storage, sensing, drug delivery and heterogeneous catalysts. Nevertheless, due to the porous framework and unique large-scale flexibility, displayed by many MOFs, these compounds undergo adsorption-induced significant lattice contraction and expansion or transformations following the adsorption (or desorption) of gases or liquids [165]. These features may change their thermal expansion property completely.

3.11 2D materials

Negative thermal expansion in 2D materials such as graphene [14, 37], transition metal dichalcogenides [166, 167], blue and black phosphorene [168–171], arsenene and antimonene [15] and layered structures stacked by van der Waals interactions [150] has been reported in recent years.

These materials show a distinctive in-plane negative thermal expansion which is strong temperature dependent. For graphene, a value of -8.0×10^{-6} K^{-1} at room temperature was reported by Yoon *et al.* [14]. Nevertheless, after consideration of this strain profile and after incorporating temperature dependent Grüneisen parameter corrections [172], the CTE of graphene is estimated to be -3.75×10^{-6} K^{-1} on average for the entire temperature range and it approaches close to zero for $T<150$ K.

First-principles calculations showed that the NTE in the monolayer is mainly determined by the out of plane ZA mode, which has a negative Grüneisen parameter and results in the in-plane shrinkage. The ZA mode is also found to be the dominate mechanism for the in-plane NTE of three different types (α, β, and γ) of graphyne [173] and two to five monolayer CdSe nanoplatelets [174]. Monolayer graphene is predicted to exhibit NTE over 2300 K due to an additional out of plane optical ZO′ mode at about $\sim$900 cm^{-1} with a small negative Grüneisen parameter [37, 93] or the "vibrational elongation" effect arising from large out-of-plane fluctuations [175]. In bilayer and multilayer graphene, there appears a new optical ZO' mode, in which the out-of-plane atomic displacements are in phase in the same layer and out of phase in adjacent layers. This mode has a negative Grüneisen parameter.

The blue phosphorene displays an isotopic in plane NTE from 0 to 350 K while the thermal expansion behavior in black phosphorene is highly anisotropic. In black phosphorene, the ZO mode with a frequency of $\sim$130 cm^{-1} is also characterized by a negative Grüneisen parameter [176]. The monolayer of $MoTe_2$ and WTe_2 consists of three atomic layers. The ZA mode has a large negative Grüneisen parameter while LA and TA modes with an *in-plane* polarization also have small negative Grüneisen parameters [38]. The TA and LA modes with a negative γ were also observed in monolayers of silicene and germanene [171]. All three types of graphyne are predicted to exhibit larger coefficients of NTE than graphene up to T =1000 K. Besides the ripple effect, particular phonon modes identified as "rigid unit modes" corresponding to the libration of each rigid unit composed of sp^2 bonds with frequencies of around a few hundreds of cm^{-1} may fill empty spaces resulting in area reduction as well [177]. Antimonene is expected to display NTE in the whole temperature range studied while arsenene only in low temperatures. In arsenene and antimonene, the contribution from the transverse acoustic TA mode is not negligible [15]. In nanoplatelets, in addition to ZA and TA acoustic modes, there are n optical E modes (n is the thickness of the nanoplatelet) and two surface E modes which have negative Grüneisen parameters.

In-plane NTE was also found in layered structures of 3D frameworks such cyanide $Ni(CN)_2$ [150] and $Ta_2Mo_2O_{11}$ [178]. Both display NTE within the layers, and PTE in the direction perpendicular to the layers. In contrast to $Ni(CN)_2$ which exhibits weak in plane NTE and strong PTE in the c-direction, giving rise to a large volume expansion, $Ta_2Mo_2O_{11}$ has a low volume NTE with much lower thermal expansion anisotropy.

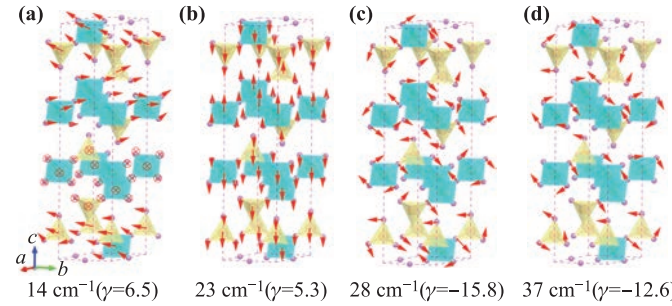

Fig. 12 Low frequency phonon modes contributing to positive and negative thermal expansion [178].

$Ta_2Mo_2O_{11}$ forms a layered structure with corner-sharing TaO_6 octahedra and MoO_4 tetrahedra. Within the layer, each TaO_6 octahedron is connected with three TaO_6 octahedra and three MoO_4 tetrahedra, while each MoO_4 tetrahedron shares its corners with only three TaO_6 octahedra. The layers stack along the c axis through van der Waals interactions. The CTEs were measured to be $\alpha_a = -4.15\times10^{-6}$ K^{-1}, $\alpha_c = 9.42\times10^{-6}$ K^{-1} and $\alpha_l = -0.37\times10^{-6}$ K^{-1} by temperature-dependent high-resolution SXRD. Its in-plane NTE is identified to arise from the phonon modes involved in the transverse displacements of bridging oxygen atoms and rotations of the polyhedra (Fig. 12). The phonon modes associated with the layer shearing motions (LA) and opposite/parallel motions between the layers (TA) have positive Grüneisen parameters and are responsible for the PTE along the c-axis [178].

4 NTE induced by spontaneous volume magnetostriction

4.1 Mechanism of spontaneous volume magnetostriction

The magnetovolume effect (MVE) is a change in volume due to a variation in the amplitude of the average magnetic moment in a magnetic material. A general explanation of NTE caused by the MVE is that a larger volume favors the appearance of an average magnetic moment in a metal. Guillaume firstly reported the MVE in Invar magnetic alloy $Fe_{65}Ni_{35}$ in 1897 [179]. The "Invar" indicates invariant volume of the alloys over a wide temperature range. The Invar magnetic alloys are the magnetic alloys with low or zero thermal expansion properties below the magnetic ordering temperature. It was believed very early that there must exist a negative contribution to the thermal expansion, which is related to magnetism and which compensates the ever present positive contribution coming from the anharmonicity of the lattice vibrations. The early simple phenomenological 2γ-state model was then

proposed to explain the MVE in the Invar alloys [180]. The key of the model is the hypothesis that there exist low-spin/low-volume and high-spin/high-volume states in the magnetic alloys. The model may explain Invar effect for many magnetic alloys. However, it does not describe the low temperature behavior properly and would actually require the existence of magnetic inhomogeneities. Moriya *et al.* proposed a spin fluctuation theory for itinerate ferromagnetic metal [181, 182] to fix the problems. Another disordered local moment (DLM) model developed from the spin fluctuation theory was also proposed to understand the Invar behavior of the weak itinerate magnetic alloy Fe-Ni [183, 184]. The advantage of the DLM formalism is that it can directly be related to a finite temperature state of the magnetic alloy. In recent decades noncolinear spin ordering were introduced in *ab initio* calculations based on density functional theory to allow for a continuous magnetic transition in FeNi [185, 186].

In the framework of the spin fluctuation model established on the Landau–Ginzburg theory [187], the spontaneous volume magnetostriction (SVMS) $\omega_s(T)$ can be written as a function of the amplitude of magnetic moment M and spin fluctuation ξ,

$$\omega_s(T) = 3\sum \alpha_m(T)\mathrm{d}T = kC_{mV}\left\{M^2(T)+\xi^2(T)\right\}, \tag{22}$$

where $\alpha_m(T)$ is the magnetic contribution to linear CTE at temperature T, k and C_{mV} are the compressibility and the magnetovolume coupling parameter, and $M(T)$ and $\xi(T)$ are the amplitudes of local magnetic moment and spin fluctuations, respectively. The first term is important in itinerant ferromagnets, where the $3d$ electron states responsible for magnetism generally form an energy band. The magnetization arises as a result of splitting of sub-bands owing to the exchange interaction (spontaneous effect) or to application of the external magnetic field H (forced, or field-induced effect). The $3d$-band polarization causes an increase in the kinetic energy of electrons. This is compensated by a volume expansion. The increase in kinetic energy is proportional to square of magnetic moment (M^2) to a first order of approximation. With increasing temperature, the absolute value of the "long-time averaged" magnetization (M) decreases as $M(T) = M_0 - \alpha T^{3/2}$ (Bloch's $T^{3/2}$ law). The second term originates from fluctuations of the magnetic (electron spin) moment in magnetic systems. The spin fluctuation represents the random, time-dependent deviation from the "long-time average" magnetization $M(T)$. By the microscopic spin fluctuation theory, the mean square amplitude of the fluctuating magnetization is shown to be constructed from two contributions of the thermal and zero-point spin fluctuations. It is a monotonically increasing function of temperature and can be estimated from the microscopic theory [188, 189]. In the ground state (T =0 K) of a ferromagnetic system, all local moments are oriented in the same direction (the effect of the zero-point spin fluctuations is exclusive), the spin fluctuation is zero [$\xi(T) = 0$]. At low temperature far from critical point T_C, $\omega_s(T)$ can be simply estimated from the square of magnetism, $M^2(T)$. Figure 13 shows the temperature dependence of lattice parameters of Y_2Fe_{17} (hexagonal crystal structure) and Y_6Fe_{23} (cubic crystal structure) and the temperature dependence of $\omega_s(T)$ for Y_2Fe_{17} and Y_6Fe_{23}. The solid lines in the figure (the first two panels) represent the phonon contribution to the thermal expansion obtained by extrapolation of the paramagnetic behavior into the ferromagnetic range according to Debye–Grüneisen relationship. Below the Curie temperature, T_C, the experimental curves deviate from the extrapolated ones. The differences between the measured and the extrapolated values of the respective lattice parameters correspond to the spontaneous volume magnetostriction (SVMS) $\omega_s(T)$. In Fig. 13 (bottom) the temperature dependence of $\omega_s(T)$ for Y_2Fe_{17} and Y_6Fe_{23} is compared with $M^2(T)$. A good agreement can be seen for a wide temperature range. However, as temperature increases the deviation from experimental values becomes obvious, especially at critical point T_C, where $M^2(T)$ is zero. The deviation can be attributed to the effect of spin fluctuation.

There are many magnetic compounds which exhibit MVE, such as Invar alloys, Laves phase inter-

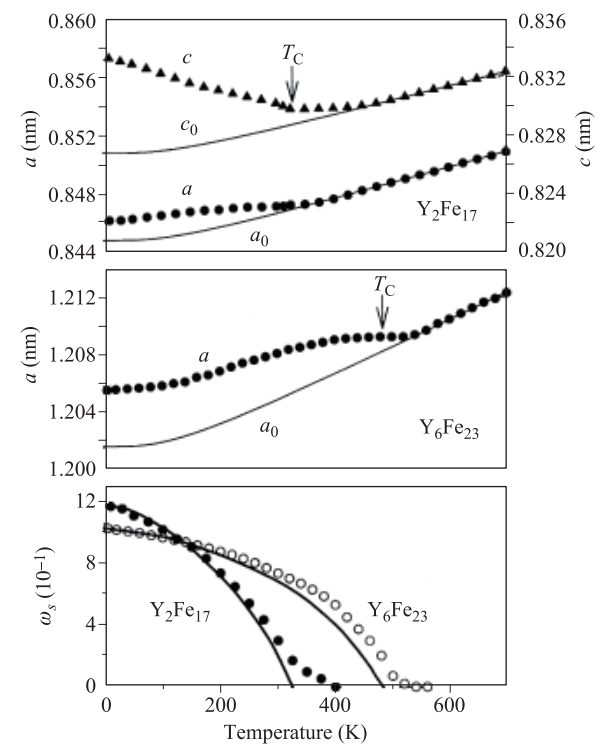

Fig. 13 Temperature dependence of lattice parameters a and c of Y_2Fe_{17} and a of Y_6Fe_{23}. The curves are the phonon contributi on to the thermal expansion. The arrows indicate the Curie temperature. Bottom: Temperature dependence of spontaneous volume magnetostriction ω_s; the lines represent the $\omega_s(T)=\omega_s(0)M^2(T)/M^2(0)$ dependence [190].

metallics [190–198], and antiperovskite of Mn_3AX, which can be well understood in the framework of the spin fluctuation model [199–205].

4.2 Invar alloy and magnetic intermetallic compounds

Invar alloys have been studied for more than one hundred years since the discovery of the invar alloy $Fe_{65}Ni_{35}$ by Guillaume in 1897. The investigations on invar effect also extended from invar alloys to generally magnetic materials. For more information on invar effect readers can refer to the excellent reviews [206–209].

The invar effect has been found in many ferromagnetic alloys, for examples in Fe-based binary and ternary alloy like $Fe_{1-x}Pt_x$, $Fe_{1-x}Mn_x$, $Ni_{1-x}Mn_x$, $Co_{1-x}Mn_x$, $Co_{1-x}Fe_x$, $Cr_{1-x}Fe_x$, $Cr_{1-x}Mn_x$, Fe–Ni–Co, Fe–Co–Cr, Fe–Ni–Mn [206, 210, 211], in many intermetallic compounds like $ZrFe_2$ [212], MnB [213], $RECo_2$(RE: Gd, Tb, Dy, Ho, Er), RE_2Fe_{17} (RE: Y, Dy, Lu) [214, 215], $(Hf_{1-x}Nb_x)Fe_2$ ($0 < x \leq 0.15$) [209], in shape memory alloy $Ti_{29.7}Ni_{50.3}Hf_{20}$ [216], and in gum metal, a class of Ti-Nb based alloys [217]. Similar NTE behaviors related to Invar effect were also found in La(Fe, Si)$_{13}$-based compounds [19, 218], Fe-doped MnNiGe [219], $CrTe_{1-x}Se_x$ ($0 \leq x \leq 0.15$) [220], $Nd_2Fe_{16.5}Cr_{.5}$ [221]; $Mn_{2-x}Cr_xSb$ [222] and $Gd_5(Si,Ge)_4$ [223]. In contrast to most magnetic materials whose NTE are governed by magntovolume effect, the NTE behavior in $Gd_5(Si,Ge)_4$ was found in two temperature windows: 90–160 K (-32.2 ppm K^{-1}), and within the room temperature 255–340 K (-69 ppm K^{-1}). Based on the fact that the observed NTE is retained even at temperatures above the magnetic ordering temperature, the magnetovolume coupling is discarded as the primary cause of NTE in the authors' opinion. They attributed the NTE to the bond flexing of the key Ge3-Gd1-Ge3 triplet chain and a size-reduction effect.

Recently, Song *et al.* reported a chemical modification strategy to transform thermal expansion from positive to negative in cubic magnetic compounds of (Zr, Nb)Fe_2 by tuning the magnetic exchange interaction. They found that an isotropic zero thermal expansion can be established in $Zr_{0.8}Nb_{0.2}Fe_2$ ($\alpha = 1.4 \times 10^{-6}$ K^{-1}, 3–470 K) over a broad temperature range that is even wider than that of the prototype Invar alloy of $Fe_{0.64}Ni_{0.36}$. The NTE of (Zr, Nb)Fe_2 is originated from the weakened magnetic exchange interaction and the increased d electrons of Fe by the Nb chemical substitution [224]. They also reported an unconventional MVE in the solid solution of $(Sc_{1-x}Ti_x)Fe_2$ ($x = 0.6$, $\alpha_V = 28.36\times10^6$ K^{-1}, 125–205 K) which were attributed to the ferromagnetic transition from one with high moment to another with low moment. The (Sc, Ti)Fe_2 material is a first example that shows an unconventional MVE caused by the new type of ferromagnetic-to-ferromagnetic transition [225].

Yokoyama *et al.* [226] reported local thermal expansions and lattice strains in the Elinvar alloy $Fe_{49.66}Ni_{42.38}Cr_{5.49}Ti_{2.47}$ (Ni Span C). They found that the local thermal expansion around Fe is considerably smaller than the ones around Ni and Cr. According to zero- and finite-temperature first-principles calculations versus composition, Crisan *et al.* [184] suggested that magnetochemical effects lead to Invar anomalies in Fe–(Ni, Co, Pt) alloys. Chemical short- or long-range order and negative interatomic exchange interaction of electrons in antibonding majority-spin states force the face-centered-cubic lattice to compete simultaneously for a smaller volume (from antiferromagnetic tendencies) and a larger volume (from Stoner ferromagnetic tendencies).

4.3 Antiperovskite manganese nitrides Mn_3AN (A =Zn, Ga, etc.)

Antiperovskite manganese nitrides Mn_3AN (A = Zn, Ga, etc.) were found to be a typical class of materials that feature giant NTE of a magnetic origin [16, 17, 205, 227]. Sharp volume contraction occurs upon heating from low-temperature large-lattice antiferromagnetic (AF) to high-*temperature* small-lattice paramagnetic (PM) phases.

A classical spin model with competing bond-length dependent exchange interactions was developed to study the magnetism-induced NTE in inverse perovskite antiferromagnets Mn_3AN (A = Zn, Ga, etc.) [228] and the condition for occurrence of the NTE upon the magnetic transition to the Γ^{5g}-type antiferromagnetic order was obtained as

$$0.714 < \frac{J^{FM}}{J^{AM}} \leq 1. \tag{23}$$

J^{AM} is the antiferromagnetic exchange of the direct Mn–Mn path and J^{FM} is ferromagnetic exchange of Mn–N–Mn path mediated by N ions at the center of the octahedron. The spin model neglected higher harmonic elastic term and orbital degrees of freedom and produces the second-order phase transition which contradicts with the experimentally observed first-order phase transition. A more theoretical study incorporating the orbital degrees of freedom is expected.

Though magnetovolume effect has been found in a variety of magnetic compounds, the physical mechanism for this magnetism-induced volume contraction has yet to be well elucidated due to the complexity of coupling among the spin, electron and phonons. In the low temperature larger volume AF phase, spin–phonon coupling plays a more important role than the electron–phonon coupling, whereas in the high temperature small volume PA phase, electron–phonon coupling will become important due to the metallic nature of PA ordering phase. The interplay among the freedoms of spin, electron and lattice need to be examined.

Since the giant NTE in these materials is companied by the antiferromagnetic to paramagnetic phase transition, it occurs generally within a narrow temperature window. To tailor the coefficient of NTE and broaden the NTE

temperature window are current hot topics. Many experimental results demonstrated that tailoring thermal expansion property of these materials is possible by partial replacement of constituent elements [18, 20, 229–231]. Generally, partial replacement of constituent elements may induce a local structure distortion due to the different atomic radius of the substitutional atoms. For the magnetic materials, the local distortion can alter the distance of the coupling magnetic atoms and the ordered magnetic moment, and consequently the NTE temperature window may be tuned wide through the way [232, 233]. Alternatively, by decreasing the dimension of the antiperovskite manganese nitrides to the nanoparticle size, the NTE operation-temperature window becomes also broaden, which is attributed to the excess atomic displacements together with the reduced structural coherence of the nanoparticles [234, 235].

4.4 Magnetic oxides

NTE and spin frustration in hexagonal $GdInO_3$ in the temperature range of 50–100 K was reported by Paul *et al.* [236]. Magnetostriction measurement and the anomalous softening of the phonon mode of Gd-related atomic vibration indicate a spin–phonon coupling in this system. The competitive role of magnetic interaction energy and thermal stabilization energy in determining the change in interatomic distances is the possible origin for the NTE in $GdInO_3$ over a limited range of temperature.

Miao *et al.* [237] reported a new class of layered Perovskite $LnBaCo_2O_{5.5+x}$ (Ln = Pr or Nd) MVE material which exhibits a strong NTE ($\alpha_V = -3.6 \times 10^{-5}$ K^{-1} at $PrBaCo_2O_{5.74}$) near the boundary between ferromagnetic (F) and antiferromagnetic (AF) phases in the phase diagram. They attributed the MVE to the competition between F clusters and the AF matrix. Other layered Perovskite oxides, such as Ruddlesden–Popper $A_{n+1}B_nO_{3n+1}$ [96, 238, 239], which also exhibit NTE induced by multiple effects, will be described in Section 7.

5 NTE induced by spontaneous volume ferroelectrostriction

5.1 Mechanism of NTE driven by spontaneous polarization

Spontaneous polarization in a ferroelectric (FE) material occurs below its Curie temperature, which increases with the decrease of temperature. The phase transition from nonpolar to polar in a displacive FE crystal is accompanied by the displacement of certain atoms from their higher temperature symmetry positions. Spontaneous polarization P_S is associated to the atomic displacement by

$$P_S = \frac{1}{V_c}\sum_i eZ_i^*(u_i - u_{ic}), \tag{24}$$

where V_c is unit cell volume at Curie temperature, eZ_i^* the Born effective charge, and $u_i - u_{ic}$ the displacement of ion i along the polarization direction in the unit cell of the FE state with respect to a reference nonpolar paraelectric (PE) state at Curie temperature. With the increase of temperature, the overall spontaneous polarization decreases gradually and becomes zero at the FE–PE phase transition temperature. In an ionic crystal, the Born affective charge is assumed not to change with temperature. The increase in spontaneous polarization with decreasing temperature means a larger displacement but in opposite directions for positively and negatively charged ions, resulting in macroscopically an increase in the crystal lattice along the easy-polarization direction. Eq. (24) is therefore correlated to lattice parameters by

$$P_S = \frac{1}{V_c}eZ^*(x - x_c), \tag{25}$$

where x denotes the lattice parameter a, b or c, depending on the easy-polarization direction, and eZ^* the total effective charge. The linear relationship in Eq. (25) is in good agreement with the experimental empirical one obtained for a number of ferroelectrics [240]. For a cubic PE to tetragonal FE phase transition and polarization along the c direction, Eq. (25) may be reformed as

$$P_S = \beta\left(\frac{c}{a} - 1\right) = \beta'\left(\frac{V - V_c}{V_c}\right) = \beta'\omega_s, \tag{26}$$

where $\varepsilon = \left(\frac{c}{a} - 1\right)$ is the tetragonal strain, $\omega_s = \frac{V - V_c}{V_c}$ the spontaneous volume ferroelectrostriction (SVFS), $\beta = \frac{a}{V_c}eZ^*$ and $\beta' = \frac{1}{ab}eZ^*$ the electron-lattice coupling constants. Eq. (26) indicates that the NTE in the easy polarization direction follows the trend of tetragonal strain and volume ferroelectrostriction, which is in good agreement with experimental results in $PbTiO_3$–(Bi, La)FeO_3 [241].

According to Eq. (26) and the definition of CTE, the axial coefficient is proportional to the spontaneous polarization and inversely proportional to temperature change dT,

$$\alpha_c = \eta\frac{P_S}{\mathrm{d}T}, \tag{27}$$

where η is the proportional coefficient.

The empirical relation of phase transition temperature is [240]

$$k_B T_C = \frac{1}{2}K(u_i - u_{ic})^2, \tag{28}$$

where k_B is the Boltzmann constant and K has the dimensions of a force constant. At T_C, the amplitude of thermal motion of the homopolar atom becomes equal to u_{ic}, resulting in an average displacement of zero for this atom. Below T_C, as the thermal amplitude progressively decreases, the average displacement increases to its asymptotic value $u_i - u_{ic}$, at which point the low-temperature displacive energy is equal to the thermal energy at the Curie point.

5.2 $PbTiO_3$-based compounds

Perovskite $PbTiO_3$ is one of the most extensively studied ferroelectric materials. $PbTiO_3$ shows the ferroelectric tetragonal (FE) to paraelectric cubic (PE) phase transition at about 763 K at ambient pressure. The FE phase has a large tetragonal distortion with an axis ratio of $c/a = 1.06$ at room temperature, resulting in considerably large spontaneous polarization and ionic shifts, high Curie temperature T_C, and a wide temperature region in which the tetragonal phase is stable along with the NTE phenomenon.

$PbTiO_3$ adopts a tetragonal (*P4mm*) ferroelectric (FE) structure at RT and exhibits unusual NTE behavior along the *c*-axis from RT to Curie temperature (763 K) from where it transforms to paraelectric (PE) cubic phase [23]. The NTE of $PbTiO_3$ is considered to result from SVFS. The NTE in ferroelectrics takes place when the SVFS surpasses the inherent lattice anharmonicity. Experimental evidence [242] indicates that there is an apparent correlation between tetragonality (c/a) and spontaneous polarization originating from Pb/Bi–O hybridization which is strongly associated with the negative thermal expansion. Raman scattering experiments [243] showed obvious softening of several low frequency phonon modes with increasing pressure, which corresponds to negative Grüneisen parameters. First principles calculations by Wang *et al.* [244] showed that optical phonons contribute to volume contraction but the overall contribution from all phonons to thermal expansion is positive. Nevertheless, *ab initio* molecular dynamics simulations [245] showed that both tetragonal and cubic local atomic configurations coexist below and above the FE–PE transition temperature. The fraction of tetragonal configuration decreases and that of cubic configuration with smaller volume increases with the increase of temperature, depicting the origin of its NTE phenomenon. By combining a theory analysis and first principles calculations, Ritz and Benedek [23] found that the NTE in $PbTiO_3$ involves a delicate interplay between the phonon properties of a material (Grüneisen parameters) and its anisotropic elasticity. Considering the results above, the uniaxial NTE in $PbTiO_3$ arise from the interplay between spontaneous polarization and phonons whereas part of volume contraction originate from the increased cubic to tetragonal phase ratio with increasing temperature.

5.3 $PbVO_3$

$PbVO_3$ has a perovskite $PbTiO_3$-type tetragonal crystal structure with a giant lattice distortion ($c/a = 1.23$ at RT) and a calculated spontaneous polarization P_s exceeding 100 μC/cm^2 which are much larger than that in $PbTiO_3$ ($c/a = 1.06$ and $P_s = 59$ μC/cm^2 at RT). $PbVO_3$ exhibits a pressure induced large volume collapse reaching 10.6% originating from a transition from a polar insulator tetragonal (*P4mm*) phase to a non-polar metallic cubic (*Pm-3m*) one [246, 247]. Temperature induced tetragonal-to-cubic transition and NTE were observed in fluorine substituted $PbVO_{3-x}F_x$ by Ogata *et al.* [248]. The decrease in the average volume results from the decrease in the fraction of the large tetragonal phase and the increase in the small cubic phases during phase transition since both the tetragonal and cubic phase show normal thermal expansion on heating. The average linear CTE is about $\alpha_l = -50$ ppm K^{-1} (233–473 K) for $PbVO_{2.79}F_{0.21}$. Dilatometry measurement gives an unusually large magnitude of NTE ($\alpha_{l,d} = -358$ ppm K^{-1}) in this composition. Similar effects were also observed in $PbV_{1-x}Cr_xO_3$ [249] and La substituted $Bi_{0.5}Na_{0.5}VO_3$ [250].

5.4 $Sn_2P_2S_6$

An averaged large volume NTE of -4.7×10^{-5} K^{-1} from 243 K to T_C (338 K) was observed in the non-perovskite lead-free ferroelectric $Sn_2P_2S_6$ [251]. Structure refinements and first-principle calculations revealed that spontaneous volume ferroelectrostriction could well elucidate the nature of NTE in ferroelectric $Sn_2P_2S_6$.

5.5 GeTe

GeTe is a well-known ferroelectric and thermoelectric material that undergoes a ferroelectric phase transition from a rhombohedral to a cubic structure at Curie temperature of about 600–705 K depending on the stoichiometry. An anomalous volume contraction of 0.6% was demonstrated across the phase transition [252, 253]. First-principles calculations show that the negative thermal expansion is induced by the coupling between acoustic and soft transverse optical phonons [254].

6 NTE induced by charge transfer

6.1 Mechanisms of NTE driven by charge transfer

This type of NTE is associated with the volume shrinkage resulting from thermally activated charge transfer process between constituent ions. With a constant anion, unit cell volumes of isostructural series are proportional to the cation volumes [255]. As shown in Fig. 14(a), a cation size at higher oxidized state is smaller than at lower oxidized state when the coordination number keeps unchanged. The valence transition from low oxidized state to high oxidized state or vice versa will thus have a profound effect on the lattice size. A cation accepting electrons expands, whereas a cation donating electrons shrinks. When the expansion exceeds the value of shrinkage, a net volume shrinkage occurs. However, this variation in the ionic radius depends strongly on the element and/or electronic configuration. The ionic radius expands with the coordination number and the transition from low spin (LS) to

high spin (HS) state as well, as shown in Fig. 14(b). For a given valence and coordination number, the high-spin state has a larger radius than the low-spin state due to the constraint of the Pauli exclusion principle, which requires the electrons to be placed in different orbitals in the case of a high-spin configuration.

6.2 Rare-earth fullerides

NTE driven by thermally induced charge transfer has been reported for $Sm_{2.75}C_{60}$ [256] and $Yb_{2.75}C_{60}$ [257]. They show a temperature induced quasi-continuous isosymmetric phase transformation accompanied by significant lattice contraction: 0.84% for $Sm_{2.75}C_{60}$ from 4.2 to 32 K and 1.4% for $Yb_{2.75}C_{60}$ from 5 to 60 K. The profound effect on the lattice size were attributed to valence transition of Sm^{2+} (Yb^{2+}) $\rightarrow$ Sm^{3+} (Yb^{3+})+ e electron transfer induced on heating and the coupling of the Sm (Yb) $4f$ band to the electronically active t_{1u} band of C_{60}.

6.3 SmS-based monosulfides

Samarium has two possible ground state configurations in SmS, a nonmagnetic Sm^{2+} with $4f^6(^7F)$ configuration and a magnetic Sm^{3+} with $4f^5(^6H_{5/2})$ configuration. SmS exhibits pressure- and temperature-induced semiconducting (black)–metallic (gold) transition and a volume change driven by the electronic configurations alteration of samarium atoms. The results of an earlier X-ray diffraction (XRD) study [258] suggested possible NTE with the volume change exceeding 3% in $Sm_{1-x}Y_xS$. A recent study using high-quality single crystals of Y-doped SmS verified a large volume change related to NTE of up to 4.1% from 100 to 315 K, via control of the electronic configuration in Sm atoms of SmS by partial replacement of Sm with Y [259]. Similarly, a giant NTE of $Sm_{0.80}Ce_{0.20}S$ with total volume change of 2.6% from 100 to 330 K was also reported [260]. The valence change is considered to be caused by a strong coupling between an emergent Kondo lattice state and a large isotropic volume change, suggesting that the electron-lattice coupling gives rise to a unified mechanism underpinning the pressure- and temperature-induced volume collapses, and the associated giant NTE in the golden phase [261].

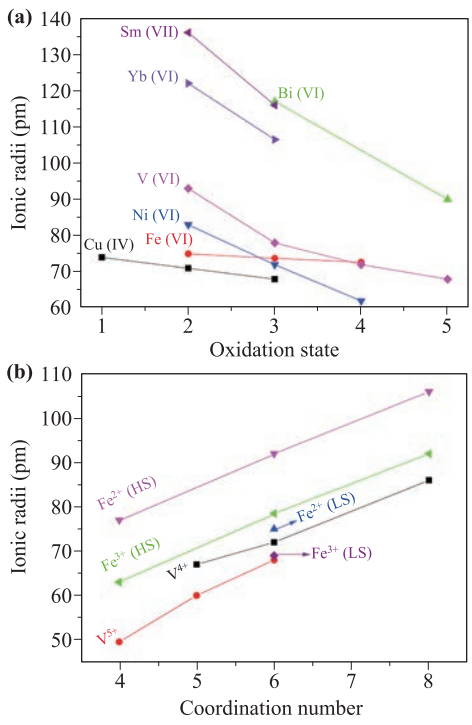

Fig. 14 Illustrations of ionic radii changes with oxidation state **(a)** and coordination number/spin state **(b)**. Data are from Ref. [255].

6.4 $LaCu_3Fe_4O_{12}$, La-doped $BiNiO_3$ and V_2OPO_4

The A-site-ordered perovskite $LaCu_3Fe_4O_{12}$ was the first compound found to show temperature-induced intermetallic charge transfer (CT) at ambient pressure [24]. Intersite charge transfer from the B-site Fe to A-site Cu ions leads to antiferromagnetism-to-paramagnetism and insulator-to-metal isostructural phase transitions accompanied by a large decrease in unit-cell volume (~1%) at the CT transition temperature. In $LaCu_3Fe_4O_{12}$, the sensitive expansion of Cu–O bonds to temperature can trigger a transformation from Cu^{3+} to Cu^{2+}, which imposes a covalent state transition of B-site Fe from +3 to +3.75. The resultant shrinkage of the Fe–O bonds is demonstrated to play a pivotal role in the volume contraction of the oxide at high temperatures [262]. Subsequently, CT-induced cell volume contraction (~2.6%) was found in La-doped $BiNiO_3$ [25] and $SrCu_3Fe_4O_{12}$ [263]. It is shown that the observed volume changes are primarily caused by the size effect of the constituent ions in the oxides and can be qualitatively reproduced with a simple ionic crystal model by using the SPuDS software program [264]. In La-doped $BiNiO_3$, the large change results from the dominant contraction of the Ni–O perovskite framework as Ni^{2+} is oxidized to the smaller Ni^{3+} at the transition, which outweighs the lattice expanding effects of reducing Bi^{5+} to Bi^{3+} and increases in the Ni–O–Ni angles. The changes of oxidation states in Bi and Ni ions lead to changes of Ni–O and Bi–O bonds and distortion/rotation of NiO_6 octahedra and displacement of metal atoms. Shrinkage in cell volume is attributed to the release of stress [265]. A theoretical analysis shows that the valence transition is caused by commensurate locking of the electron filling in each orbital associated with charge and magnetic orderings, and the critical temperature and the nature of the transitions are strongly affected by the relative energy between the Bi and Ni levels and the effective electron-electron interaction in the Bi sites [266].

V_2OPO_4 adopts a monoclinic distortion to *C2/c* sym-

metry below a charge ordering transition T_{co} with long range V^{2+}/V^{3+} charge ordering and a tetragonal $I4_1/amd$ structure above the transition. Anisotropic NTE ($\alpha_a = -10.8 \times 10^{-6}$ K^{-1}, $\alpha_c = +8.3 \times 10^{-6}$ K^{-1}, $\alpha_V = -13.3 \times 10^{-6}$ K^{-1}) in the (a, b)-plane between 600 to 800 K in V_2OPO_4 was recently reported above $T_{co} =$ 605 K [267, 268]. The NTE is believed to arise purely from loss of charge ordering ($V^{2+}V^{3+}OPO_4 \rightarrow V_2^{2.5+}OPO_4$). The overall volume change $\frac{\Delta V}{V} = -0.3\%$ arises from the average size of ordered V^{2+} and V^{3+} in the monoclinic phase being slightly greater than that of the disordered or delocalized $V^{2.5+}$ state in the tetragonal structure at a given temperature.

CT induced NTE is usually large but only within a very narrow temperature window. Elemental doping is shown to be an effective way to broaden the temperature window of NTE to some extent and realize tunable CTE [269, 270].

7 NTE in layered perovskites like oxides

Due to their unusual lattice couplings and dynamics, there has been renewed recent interest in tuning the properties of layered materials based on the perovskite structure, including proper [271], and improper [272] ferroelectricity, the electrocaloric effect [273], colossal magnetoresistance [274] and negative thermal expansion [96, 98, 275]. Many of these physical properties of layered materials based on the perovskite structure rely on excitations of the ground state structure and are mediated by phonon interactions, electron–phonon couplings and spin-lattice couplings. The NTE in these compounds may arise from more than one origins and has not been well studied. Due to the uniaxial NTE in these materials, the NTE behavior might be described by the uniaxial strain model, i.e., the interplay between phonons and anisotropic elasticity (Section 2.5).

The Ruddlesden–Popper (RP) series $A_{n+1}B_nO_{3n+1}$, for favorable A and B cations (A = Ca, Sr, La, B = Ti, Mn, V, Fe, Ru, and Ir), form a near-infinite homologous series of materials whose structure may be described as containing n slabs of the perovskite structure interspersed periodically with an AO rock salt layer along the c axis. Most of this group of perovskites exhibit only uniaxial NTE and their volume CTE is usually positive except Ca_2RuO_4. Ca_2RuO_4 shows very large volume NTE.

7.1 Sr_2IrO_4

Sr_2IrO_4 crystallizes in the Ruddlesden–Popper $A_{n+1}B_nO_{3n+1}$ or layered K_2NiF_4 type structure, which consists of alternate stacking of rock-salt, SrO, and perovskite like $SrIrO_3$ layers. Sr_2IrO_4 has the symmetry of space group $I4_1/acd$, and lattice parameters a =5.4994 Å, c = 25.7841 Å. An analysis of synchrotron X-ray diffraction between 20 and 1273 K by Ranjbar and Kennedy [238] showed that Sr_2IrO_4 undergoes an apparently continuous transition from $I4_1/acd$ to $I4/mmm$ near 1123 K and exhibits an unusual anisotropic NTE along the c-axis in low temperature phase (Fig. 15). The former occurs due to loss of the cooperative tilting of the IrO_6 octahedra while the latter arises from the cooperative tilting of the corner sharing IrO_6 octahedra on heating.

7.2 Sr_2RhO_4

Sr_2RhO_4 is isostructure of Sr_2IrO_4 with space group $I4_1/acd$. A continuous unusual NTE from 10 to 450 K along the c-axis in Sr_2RhO_4 ($\alpha_c = -2.33 \times 10^{-6}$ K^{-1}) was first observed by Vogt and Buttrey [276] but the mechanism was not elucidated. Recent SXRD study of Sr_2RhO_4 between 100 and 1273 K by Ranjbar *et al.* [277] showed that Sr_2RhO_4 undergoes a continuous transition from $I4_1/acd$ to $I4/mmm$ near 850 K. The c-axis is observed to contract upon heating from 100 K to ~850 K and then it increases again above this. Between 100 and ~850 K the thermal expansion of the a-axis mimics that of the cell volume. The NTE in Sr_2RhO_4 has been ascribed to static changes in octahedral rotation angle. The loss of the cooperative tilting of the corner sharing RhO_6 octahedra is believed to be the cause of the unusual thermal expansion behavior that involves remarkable uniaxial NTE that extends over several hundred degrees.

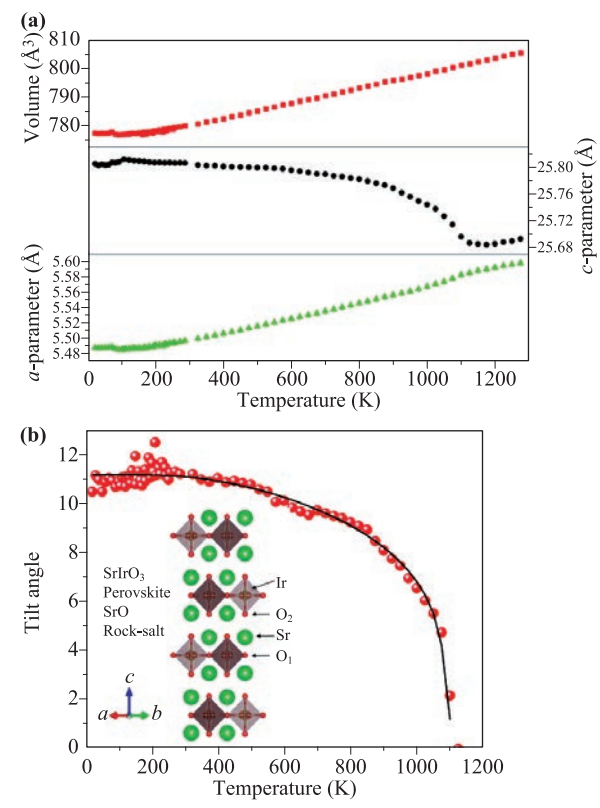

Fig. 15 Temperature dependence of the unit cell parameters and cell volume **(a)** and the tilt angle in Sr_2IrO_4 **(b)** [238].

7.3 Ca_2MnO_4 and Ca_2GeO_4

Ca_2MnO_4 has the tetragonal super structure as same as the Pb-substituted Ca_2MnO_4, the space group $I4_1/acd$, with lattice parameters $a = 5.183(1)$ Å and $c = 24.117(4)$ Å at room temperature. This $I4_1/acd$ super structure contains the tilted MnO_6 octahedra about their c axes, and the octahedra are contra-rotated along c axes. While the c axis decreases with increasing temperature, the a-axis and the unit cell volume increase up to about 1000 K [278]. The contraction along c-axis was attributed to the modification of the CaO layer which become shrunk with increasing temperature and the expansion in a-axis with increasing temperature was caused by the decreasing of the magnitude of the rotation of MnO_6 octahedra.

Based on the concepts of anisotropic elastic compliance and soft phonon modes, Ablitt *et al.* [48] presented another scenario to understand the uni-axial NTE in layered perovskites and predicted also uniaxial NTE in $I4_1$/acd Ca_2GeO_4. The NTE arises due to soft phonon modes with octahedral tilt character that have $\gamma_1>0$ and $\gamma_3<0$, which drive the contraction of the c-axis with increasing temperature, as a result of the large s_{13} components in the elastic compliance matrix.

7.4 $Ca_3Mn_2O_7$

$Ca_3Mn_2O_7$ and $Ca_3Ti_2O_7$ also belong to the RP $A_{n+1}B_nX_{3n+2}$ family of oxides, with $n = 2$. They have a layered orthorhombic structure, whereby the perovskite bilayers $[Ca(Mn/TiO_3)_2]$ are separated by the rock salt [CaO] layers along the c axis. In $Ca_3Mn_2O_7$, there is a phase coexistence over a very large temperature range (200–320 K) and a substantial hysteresis (≈70 K) on warming and cooling. A pronounced uniaxial NTE (-3.6×10^{-6} K^{-1}) along the c axis in the high temperature $Acaa$ phase and PTE in the coexisting low-temperature $A2_1am$ phase were reported by Senn *et al.* [279]. In the case of $Ca_3Mn_2O_7$, there is a complex competition between lattice modes of different symmetry which leads to a phase coexistence over a large temperature range and the "symmetry trapping" of a soft mode. The NTE in the nonpolar phase of $Ca_3Mn_2O_7$ is attributed to the symmetry trapping of the X_3^- mode (RUM) by the high-temperature $Acaa$ phase and completely unrelated to the observation of strain coupling.

In the case of $Ca_3Ti_2O_7$ with space group $Cmc2_1$, the rigid-unit modes are locked due to the low orthorhombic symmetry of the crystal. Using first-principles methods, Huang *et al.* [275] identified a quasi-two-dimensional phonon mode in the layered-perovskite $Ca_3Ti_2O_7$ which exhibits atomic displacements perpendicular to the layered $(CaTiO_3)_2$ blocks and has a negative Grüneisen parameter. Owing to the quasi-2D structural and dynamical features, the mode can be utilized to realize unusual membrane effects, including a tunable NTE and a rare pressure-independent thermal softening of the bulk modulus. Detailed microscopic analysis shows that the NTE relies on strong intralayer Ti–O covalent bonding and weaker interlayer interactions.

7.5 $LaTaO_4$

$LaTaO_4$ is a member of the $A_nB_nX_{3n+2}$ family. The crystal structure consists of perovskite-like blocks of corner-shared octahedra extending in the ac plane, separated by the La^{3+} cations. The orthorhombic polymorph O-$LaTaO_4$ (space group $Cmc2_1$) has very large negative expansivity of the b-axis ($\alpha_b \approx -40 \times 10^{-6}$ K^{-1}) in the temperature range 373–573 K, leading to a near-zero volume expansivity around 473–523 K [280]. The NTE of the b-axis was attributed to rotation of octahedra in the perovskite layer since both the inter-octahedral angle and thickness of layer contraction across the region 373–573 K while the interlayer distance changes little.

7.6 Ca_2RuO_4

Ca_2RuO_4 is a prototype Mott insulator, where all of the degrees of freedom charge, spin, orbital and lattice show robust interactions in distinctive phase transitions. It undergoes a paramagnetic metal–insulator transition at $T_{MI} = 357$ K, followed by a well-separated antiferromagnetic order at $T_N = 110$ K. The origin of the MIT, orbital ordering and spin–phonon coupling have been the hot topic intensively investigated [281–283]. The investigation of thermal expansion of Ca_2RuO_4 can be traced back to Braden *et al.* [284] and Friedt *et al.* [285]. They observed a contraction of lattice volume by 1% upon heating from 100 to 400 K for the stoichiometric crystalline Ca_2RuO_4, whereas Alexander *et al.* [286] has revealed a volume expansion of 1% during heating from 90 to 400 K for the single crystal Ca_2RuO_4. In both cases, uniaxial NTE in the b-axis was demonstrated though conflict results in volume thermal expansion were observed by different groups. Subsequently, Qi *et al.* [287, 288] found that M doping for Ru produces lattice volume NTE in $Ca_2Ru_{1-x}M_xO_4$ (M = Cr, Mn, Fe, or Cu) and the lattice volume expands on cooling with a total volume expansion ratio 1%. The onset of NTE complies well with the metal–insulator transition temperature T_{MI}, below which the volume starts to expand upon cooling. The reported results demonstrate that Cr doping shifts the T_{MI} to lower temperatures whereas Fe, Mn, Cu and Sn doping makes the T_{MI} to move to higher temperatures, capable of tuning the NTE range [96, 97, 287, 288].

A giant extrinsic NTE of $\alpha_l = -115 \times 10^{-6}$ K^{-1} in reduced ruthenate was discovered recently by Takenaka *et al.* [96, 97] as shown in Fig. 16. They attributed it to microstructural effects consuming open spaces in the sintered body on heating [289]. It is interesting to note that the NTE (intrinsic and extrinsic) in Ca_2RuO_4 seems

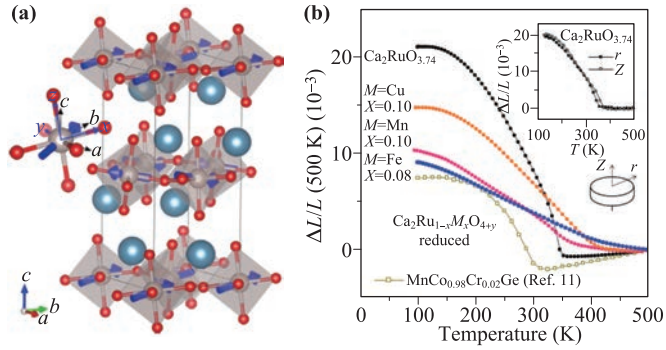

Fig. 16 **(a)** Structure of Ca_2RuO_4, and **(b)** linear thermal expansion of reduced layered ruthenates [96].

appear only in the samples with oxygen vacancies and doped samples.

Recently we studied the effect of oxygen defects on the structure and intrinsic thermal expansion property of Ca_2RuO_4 [98]. The results show that $Ca_2RuO_{4+\delta}$ containing excess oxygen adopts the *L-Pbca* structure, metallic in nature and displays a normal thermal expansion behavior in all axes, without structure and metal–insulator transitions found from 100 to 500 K. Nevertheless, all the $Ca_2RuO_{4-\delta}$ samples with oxygen vacancies crystalize in *S-Pbca* structure, insulating in nature at RT and exhibits unusually large NTE along the *b*-axis ($\alpha_b = -151.4\times10^{-6}$ K^{-1}) and enormous NTE in lattice volume ($\alpha_V = -39.8\times10^{-6}$ K^{-1} for the sample of $Ca_2RuO_{3.73}$) from 100 to about 360 K, from where it transforms to metallic *L-Pbca* phase but different from the one with excess oxygen in lattice volume (352.66 vs. 349.42 Å^3, at 400 K), Ru–O(2) bond length (2.044 vs. 2.287 Å), Ru–O(2) rotation and Ru–O(1) tilt angles. Besides, extrinsic colossal NTE ($\alpha_l = -94.4\times10^{-6}$ K^{-1}) similar to those reported by Takenaka *et al.* [96] was also demonstrated to appear only in samples with oxygen vacancies. These results indicate that oxygen vacancies play a vital role in the phase formation and the NTE behavior of Ca_2RuO_4. In fact, oxygen vacancies can have profound effects on the magnetic, electronic, and transport properties of transition metal oxides. The introduction of oxygen vacancies was also found to enhance the coefficient of NTE by about an order of magnitude in $In_{0.6}(HfMg)_{0.7}Mo_3O_{12}$ [290].

Figure 17 shows the dependence of lattice parameters, orthorhombic strain, Ru–O1 bond lengths and distortion of RuO_6 octahedra with temperature. The NTE along the *b*-axis follows the trend of orthorhombic strain which is defined as $\varepsilon=(b-a)/(b+a)$. Detailed structure analysis shows that the in-plane distortion of the RuO_6 octahedra in $Ca_2RuO_{4-\delta}$ reaches maximum across about 260 K and then relaxes monotonically as indicated by the progressive reduction of in-plane bond length difference and extension of the bond angle on cooling. The expansion of the *b*-axis in $Ca_2RuO_{4-\delta}$ on cooling is a result of in-plane distortions and the rotations (the change in the Ru–O1–Ru bond angles) of RuO_6 octahedra.

The observation of maximum in-plane distortion of RuO_6 octahedra complies well with the occurring of an antiferromagnetic orbital ordering in the paramagnetic phase across $T_{OO} = 260$ K [291] and a strong suppression of oscillation-amplitude and a phase flip over 180° for an *Ag* symmetric phonon mode [292]. Density functional theory calculations suggested that the *Ag* phonon mode oscillations result in x/y-anisotropic octahedral distortions [293]. These unusual observations suggest a complex interplay between the orbital, spin, and lattice degrees of freedom. It is noticed that an abrupt volume expansion occurs upon metal–insulator transition and a continuous expansion retains across the paramagnetic phase [287, 288] with addition magnetic ordering on cooling, suggesting that the coupling of spin–phonon interactions plays a decisive role in the contraction of the *b*-axis.

8 Tailoring the properties of framework oxides

As can be seen above, some materials display NTE only at much lower or higher temperatures than RT while some others are hygroscopic and their NTE are only observed after complete removal of crystal water. Improper phase transition temperature and hygroscopicity are major obstacles hindering their applications.

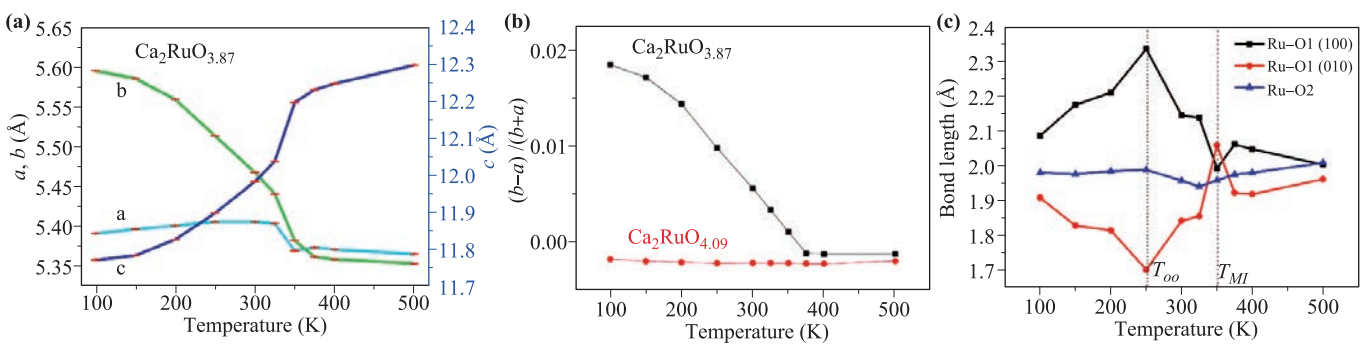

Fig. 17 Changes of lattice constants **(a)**, orthorhombic strain **(b)**, Ru–O bond lengths **(c)** and RuO_6 octahedral distortion with temperature for $Ca_2RuO_{3.87}$. In (b) orthorhombic strain for $Ca_2RuO_{4.09}$ is also illustrated for comparison [98].

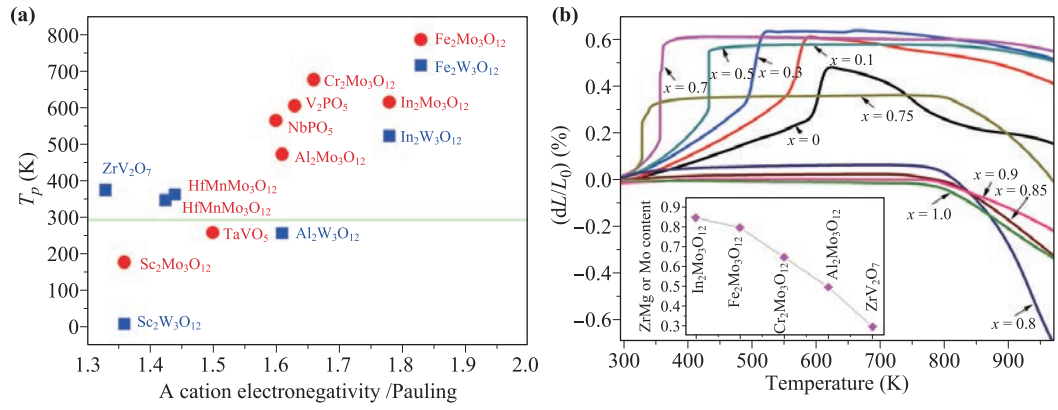

Fig. 18 **(a)** Phase transition temperature against A site electronegativity for some oxides; **(b)** Tuning the phase transition temperature of $In_2Mo_3O_{12}$ by substitution of ZrMg for In [300]. Insert: The content of (ZrMg) required to shift the phase transition to lower than RT for the $A_2Mo_3O_{12}$ compounds or Mo substitu tion for ZrV_2O_7.

8.1 Phase transition

In Fig. 18(a) we present the phase transition temperatures against the electronegativity of A-site cation for a number of framework oxides, whose NTE appear only in the high temperature phase after phase transition [65, 100, 102, 109, 118, 120, 266, 294–297]. It is noticed that the problem of high phase transition temperature is not limited to $A_2M_3O_{12}$-based compounds, but also exists in other groups of NTE materials. For example, the NTE behavior of ZrV_2O_7 [82] and $NbPO_5$ [118] occurs only at temperatures above 375 K and 565 K, respectively. Reducing the phase transition temperature to lower than RT is meaningful for a variety of applications.

For the $A_2M_3O_{12}$ compounds, the phase transition temperature depends on not only the electronegativity of A-site cation but also that of M site elements. The effect of A and M site cations on the phase transition in $A_2Mo_3O_{12}$ compounds was analyzed by Liu *et al.* [101]. There have been a lot of work in tailoring the phase transition temperature. Analysis of the documented data of tailoring the phase transition temperature shows that either single site substitution of Sc [298, 299] or the combination of (ZrMg) [107, 300–303] for the A-site cation or dual site substitutions of Zr for Fe and V for Mo [113] have been demonstrated to be effective ways in reducing the phase transition temperature, without introducing hygroscopicity. An example of $In_{2(1-x)}(HfMg)_xMo_3O_{12}$ is presented in Fig. 18(b) to demonstrate the effectiveness of such substitutions. In the insert of Fig. 18(b) [300], we summarize the content of (ZrMg) needed to reduce the phase transition temperature of the oxides to below RT. Substitution for the smaller A-site cation by a larger A^{3+} ion is very effective in reducing the phase transition temperature, but concomitantly introduces hydration nature of the materials.

Zn^{2+} substitution for Mg^{2+} seems to be an effective way to tailor the phase transition temperature of $HfMgMo_3O_{12}$ [304] and $ZrMgMo_3O_{12}$ [305] at well below room temperatures. It is interesting to note that these substitutions lead usually to near-zero thermal expansion in a large temperature range for the $A_2M_3O_{12}$-based materials [107, 113, 298–306].

8.2 Hygroscopicity

Hygroscopicity is another obstacle limiting applications of NTE materials. $A_2M_3O_{12}$ compounds with large A^{3+} cation size exhibit larger NTE over wide temperature range but they are highly hygroscopic and easily hydrated at ambient conditions. Admission of water molecules leads to an abrupt contraction and the release of them results in a sharp expansion of the lattice. NTE is only observed after complete removal of the crystal water species [307, 308]. Besides, sharp contraction and expansion of lattice by water molecules adsorption and release deteriorate mechanical property of the materials [307]. $ZrMgW_3O_{12}$ and $HfMgW_3O_{12}$ were also demonstrated to be moderately hygroscopic [85, 107]. Figure 20 shows evolution of the structure, thermal expansion property and Raman spectra of $HfMgW_3O_{12}$ from moderately hydrated to dehydrated form with increasing of temperature. Crystal water forms hydrogen bonding in the framework structure and serves as a spring to pull the polyhedrons closer. It hinders not only the transverse motions of bridge oxygen (low optical phonon modes), but also the stretch vibrations of some high frequency phonon modes, and hence the NTE [309, 310].

Such problems are not limited to $A_2M_3O_{12}$-based compounds, but also exist in other series of NTE materials, such as ZrW_2O_8 [311, 312] and a number of Prussian blue analogous $YFe(CN)_6$ [313], $ZnPt(CN)_6$ and $CdPt(CN)_6$ [314], $ErCo(CN)_6$ [315], and MOFs [164]. Hydration will also make these materials lose NTE property. It is postulated that the presence of guests within the pores of Prussian blue analogous impedes the vibrational

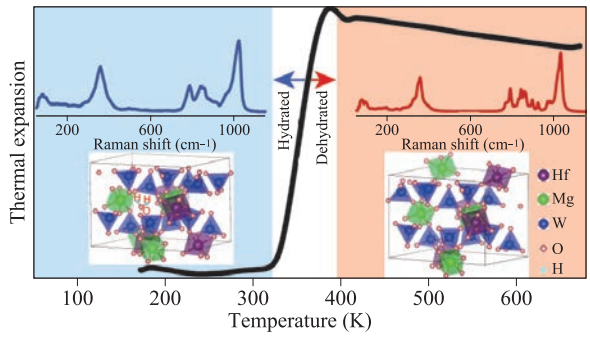

Fig. 19 Changes of structure, thermal expansion curve and Raman spectrum of hydrated $HfMgW_3O_{12}$ with temperature.

motion of the cyanide linkages responsible for loss or weakening of NTE behavior. First principles calculations for ZrW_2O_8 show that the rotation and distortion motions get inhibited on hydration and lead to positive thermal expansion [316].

Hygroscopicity for some NTE materials are summarized in Fig. 20(a), in which the number of water species per molecular unit is plotted against the electronegativity of A-site cation. Much effort has been devoted to reducing the hygroscopicity of NTE materials. It is demonstrated that the content of crystal water can be reduced to some extent by substitutions but it is difficult to eliminate crystal water completely by substitution, no matter smaller or larger sized ions are used as shown in Fig. 20(b), which contains the results of substitution of La for Y in $Y_2W_3O_{12}$ [317], Fe for Y in $Y_2Mo_3O_{12}$ [309] and Al for Yb in $Yb_2Mo_3O_{12}$ [318] and Al for (ZrMg) in $ZrMgW_3O_{12}$ [107]. When the substitution amount exceeds a critical value, the CTEs switch from negative to positive for Ce substitution for Y in $Y_2Mo_3O_{12}$ [319] and for Al substitution for (ZrMg) in $ZrMgW_3O_{12}$ [107]. Even if the CTEs become positive at higher substitution level, crystal water still could not be completely eliminated from the framework structure.

The difficulty in completely eliminating crystal water indicates that hygroscopicity is a localized effect arising from the dipole–dipole interaction between water molecules and the local A–O bonds. As it is difficult to completely eliminate the crystal water by substitution, Liu *et al.* [320] tried an alternative method to avoid the invasion of water species into the framework structure of $Y_2Mo_3O_{12}$ by heating $Y_2Mo_3O_{12}$ with $CO(NH_2)_2$. The method is effective in avoiding crystal water and retaining the NTE behavior of $Y_2Mo_3O_{12}$ at room temperature.

9 Strategies for discovering and design novel NTE materials

As can be seen above, many of NTE materials have some drawbacks such as NTE within narrow temperature window, or not covering RT range, or uniaxial NTE but with volume PTE, or hygroscopic. From application point of view, materials with isotropic or low anisotropic NTE covering large temperature range including RT are highly desired. Discovering and design NTE materials with excellent properties are challenging.

9.1 The role of the length of lattice parameter on the tuning of thermal expansion

Sanson [321] has studied thermal expansion, cubic-to-rhombohedral transition and lattice parameters in framework fluorides and found that the length of the lattice parameter plays a key role in controlling thermal expansion and phase transition. The CTEs decrease and switch from positive to negative with the increase of lattice parameter for $MZrF_6$ (Ca, Mn, Fe, Zn, Co, Ni) and $Sc_{1-x}Ti_xF_3$. This means, in isostructural materials, the magnitude of NTE increases with the lattice parameter or lattice volume.

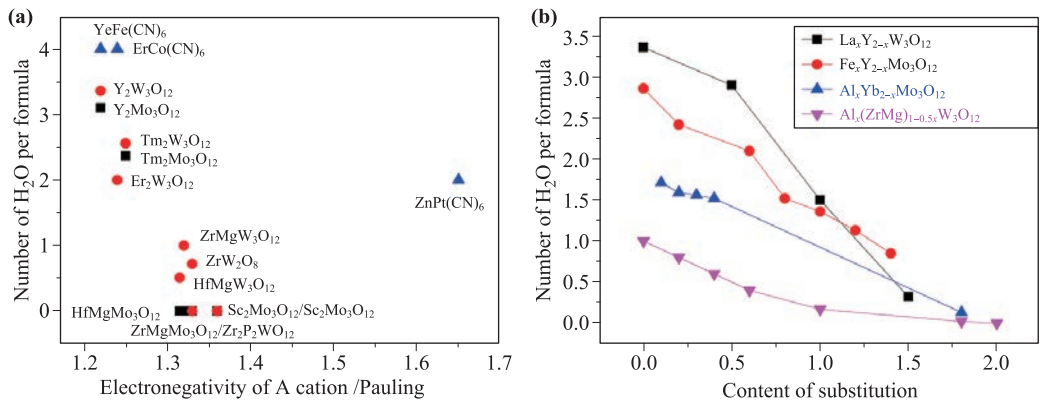

Fig. 20 **(a)** Number of water species per unit formula against the electronegativity of the A cation in some oxides and Prussian blue analogous; **(b)** The trend of the number of crystal water with the substitution content of La, Fe and Al in $Y_2W_3O_{12}$ [317], $Y_2Mo_3O_{12}$ [309], $Yb_2Mo_3O_{12}$ [318], and $ZrMgW_3O_{12}$ [108], respectively.

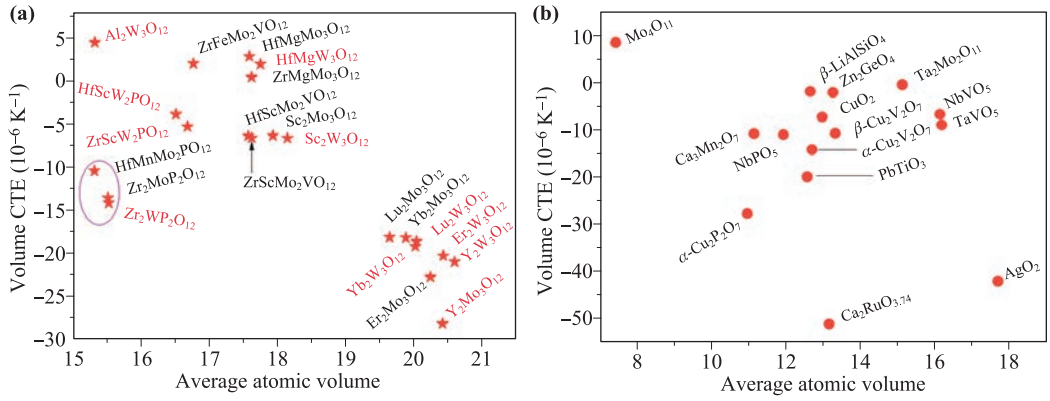

Fig. 21 Volume CTE vs. average atomic volume for framework oxides.

9.2 The concept of AAV

Recently Gao *et al.* [10] presented a concept of average atomic volume (AAV) for screening NTE materials in crystal data base. The AAV is defined as unit cell volume divided by the numbers of atoms within the unit cell. It is found that most of NTE materials with framework structure have an AAV value larger than 16 Å^3. Guided by this concept they have found two new compounds $AgB(CN)_4$ and $CuB(CN)_4$ which meet the criterion and hence display isotropic NTE in a relatively large temperature range. In Figs. 21(a) and (b) we summarize the volume CTEs for a number of NTE oxides vis. AAV. It can be seen that most of the framework structure NTE materials also meet this criterion but there are some exceptions such as α-$Cu_2V_2O_7$ [3], β-$Cu_2V_2O_7$ [94], $Cu_2P_2O_7$ [5], $Zr_2P_2WO_{12}$ [322], and $Zr_2P_2MoO_{12}$ [323]. Therefore, the criterion may be regarded as a sufficient condition for materials to display NTE. The AAV concept is helpful for search NTE materials when the lattice parameters are known.

9.3 Criterions for design NTE materials without hygroscopicity

It is found that the hygroscopicity of $A_2M_3O_{12}$ compounds is associated largely to the electronegativity of the A-site cation and the contribution from M site ion is small. Due to the large difference in electronegativity between the A site cation and oxygen, the A–O bond has a larger dipole moment than the M–O bonds and a water molecule prefers to adsorb on the A-site cation. This assumption is supported by molecular dynamic simulations [324, 325]. The M–O dipole has the effect to weaken the interaction between the water molecule and the A–O bond due to approximate opposite orientations of them in the A–O–M linkage. Whether a compound is hygroscopic or not depending on the electronegativity difference between the A-site and B-site ions rather than the coefficient of thermal expansion. For example, $HfMgW_3O_{12}$ and $ZrMgMo_3O_{12}$ have near zero thermal expansion, but the former is hygroscopic and the latter is not.

By analyzing the data in Fig. 19(a) and the results for the subgroup materials of ABM_2XO_{12} which are not hygroscopic, it is possible for us to present a criterion for design NTE materials without hygroscopicity:

$$\begin{aligned} &\chi_{A,\min} = \min(\chi_{A1}, \chi_{A2}) \geq 1.30, \\ &\bar{\chi}_{\mathrm{M,\ mean}} = \mathrm{mean}\,(\chi_{M1}, \chi_{M2}, \chi_{M3}) \leq 2.36Q. \end{aligned} \tag{29}$$

$\chi_{A,\min}$ is the minimum value of electronegativity of the A-site ions, and $\bar{\chi}_{\mathrm{M,mean}}$ the mean value of electronegativity of M-site ions. This criterion can also be taken as reference for other group of materials, for example ZrW_2O_8, and Prussian blue analogous where the A-site is metal element and M is C or N. This criterion is expected to guide design NTE materials without hygroscopicity, which is critical for NTE materials being valuable in engineering.

10 Conclusions and prospects

Increasing number of NTE materials have been discovered or designed in recent years and much progress has been made both in theoretical and experimental understanding of the origins of NTE in each category of materials. The researches in NTE phenomenon and materials are still in its infancy and unfolding as far as the mechanisms of NTE and quantity and quality of NTE materials and their applications are concerned. It is also noted that much progress in compositing NTE materials with those of PTE has also been achieved but not included here. It is interesting to note that NTE can also be realized by macro or microstructure effects and mechanical metamaterials design [326, 327] but the mechanisms are different from those discussed in this review.

As discussed above, our present understandings about the origins of NTE in most categories of NTE materials are certainly still limited and unilateral. A full understanding of the mechanisms in framework structures need to consider both the acoustic and optical phonon contributions in the entire Brillouin zone. Analytical tools such

NPD, EXAFS, Raman and infrared spectroscopy offer important information of local displacements of atoms associated with optical phonon modes but could not touch the NTE behavior driven by acoustic phonons modes that are associated with collective motions of atoms or polyhedra. The acoustic modes usually span several or tens of unit cells. Additional experimental tools such as Brillouin scattering might be used to provide complementary information. In some materials high energy optical phonon modes have also negative Grüneisen parameters but their roles in the thermal expansion are still not well understood.

Lattice dynamics simulations and first principles calculations are powerful theoretical tools in exploring the origins of NTE. Due to the computational costs, most of the calculations are limited to simple structures and simple cases using QHA which only accounts for the volume dependence of phonon frequencies and neglects higher-order anharmonicities. Such calculations might not be enough to reproduce the experimental values of CTEs, particularly at high temperatures. Theoretical calculation methods involving higher order anharmonicities are expected. It is generally accepted that negative Grüneisen parameters are necessary for phonon modes to drive NTE. Nevertheless, a recent theoretical strain model claims that negative Grüneisen parameters are neither sufficient nor necessary for a material to undergo NTE. This model is interesting but needs more experimental validations. Presently, the understanding of the NTE induced by charge transfer is still limited to the phenomenological level and the electron-phonon coupling in these systems has not well been explored yet. The origins of NTE in magnetic systems particularly those accompanied by metal–insulator and paramagnetic-antiferromagnetic transitions are still poorly understood. Theoretical models and effective calculation methods involving interplay among the freedoms of magnetic ordering, orbital ordering and lattice are expected to be developed in the near future.

Acknowledgements This work was supported by the National Natural Science Foundation of China (Nos. 11874328, 11774078, and 21905252) and China Postdoctoral Science Foundation (No. 2019M652558).

References

1. L. P. Prisco, P. I. Ponton, M. V. Guaman, R. R. Avillez, C. P. Romao, M. B. Johnson, M. A. White, and B. A. Marinkovic, Assessment of the thermal shock resistance figures of merit of $Al_2W_3O_{12}$, a low thermal expansion ceramic, *J. Am. Ceram. Soc.* 99(5), 1742 (2016)
2. T. A. Mary, J. S. O. Evans, T. Vogt, and A. W. Sleight, Negative thermal expansion from 0.3 to 1050 Kelvin in ZrW_2O_8, *Science* 272(5258), 90 (1996)
3. N. Zhang, L. Li, M. Wu, Y. Li, D. Feng, C. Liu, Y. Mao, J. Guo, M. Chao, and E. Liang, Negative thermal expansion and electrical properties of α-$Cu_2V_2O_7$, *J. Eur. Ceram. Soc.* 36(11), 2761 (2016)
4. X. H. Ge, Y. C. Mao, X. S. Liu, Y. G. Cheng, B. H. Yuan, M. J. Chao, and E. J. Liang, Negative thermal expansion and broad band photo luminescence in a novel material of $ZrScMo_2VO_{12}$, *Sci. Rep.* 6(1), 24832 (2016)
5. N. K. Shi, A. Sanson, Q. Gao, Q. Sun, Y. Ren, Q. Z. Huang, D. O. deSouza, X. R. Xing, and J. Chen, Strong negative thermal expansion in a low-cost and facile oxide of $Cu_2P_2O_7$, *J. Am. Chem. Soc.* 142(6), 3088 (2020)
6. M. K. Gupta, R. Mittal, and S. L. Chaplot, Negative thermal expansion behavior in orthorhombic $Sc_2(MoO_4)_3$ and$Sc_2(WO_4)_3$, *J. Appl. Phys.* 126(12), 125114 (2019)
7. A. L. Goodwin and C. J. Kepert, Negative thermal expansion and low-frequency modes in cyanide-bridged framework materials, *Phys. Rev. B* 71, 140301(R) (2005)
8. K. W. Chapman, P. J. Chupas, and C. J. Kepert, Compositional dependence of negative thermal expansion in the Prussian blue analogues $M^{II}Pt^{IV}(CN)_6$(M)Mn, Fe, Co, Ni, Cu, Zn, Cd), *J. Am. Chem. Soc.* 128(21), 7009 (2006)
9. S. d'Ambrumenil, M. Zbiri, A. M. Chippindale, S. J. Hibble, E. Marelli, and A. C. Hannon, Lattice dynamics and negative thermal expansion in the framework compound $ZnNi(CN)_4$ with two-dimensional and three-dimensional local environments, *Phys. Rev. B* 99(2), 024309 (2019)
10. Q. Gao, J. Wang, A. Sanson, Q. Sun, E. Liang, X. Xing, and J. Chen, Discovering large isotropic negative thermal expansion in framework compound $AgB(CN)_4$ via the concept of average atomic volume, *J. Am. Chem. Soc.* 142(15), 6935 (2020)
11. B. K. Greve, K. L. Martin, P. L. Lee, P. J. Chupas, K. W. Chapman, and A. P. Wilkinson, Pronounced negative thermal expansion from a simple structure: Cubic ScF_3, *J. Am. Chem. Soc.* 132(44), 15496 (2010)
12. J. C. Hancock, K. W. Chapman, G. J. Halder, C. R. Morelock, B. S. Kaplan, L. C. Gallington, A. Bongiorno, C. Han, S. Zhou, and A. P. Wilkinson, Large negative thermal expansion and anomalous behavior on compression in cubic ReO_3-type $A^{II}B^{IV}F_6$: $CaZrF_6$ and $CaHfF_6$, *Chem. Mater.* 27(11), 3912 (2015)
13. B. R. Hester, J. C. Hancock, S. H. Lapidus, and A. P. Wilkinson, Composition, response to pressure, and negative thermal expansion in $M^{II}B^{IV}F_6$ (M = Ca, Mg; B = Zr, Nb), *Chem. Mater.* 29(2), 823 (2017)
14. D. Yoon, Y. W. Son, and H. Cheong, Negative thermal expansion coefficient of graphene measured by Raman spectroscopy, *Nano Lett.* 11(8), 3227 (2011)
15. G. Liu and J. Zhou, First-principles study of thermal expansion and thermomechanics of group-V monolayers: blue phosphorene, arsenene, and antimonene, *J. Phys.: Condens. Matter* 31(6), 065302 (2019)
16. K. Takenaka and H. Takagi, Giant negative thermal expansion in Ge-doped anti-perovskite manganese nitrides, *Appl. Phys. Lett.* 87(23), 261902 (2005)
17. Y. Sun, C. Wang, Y. C. Wen, K. G. Zhu, and J. T. Zhao, Lattice contraction and magnetic and electronic transport properties of $Mn_3Zn_{1-x}Ge_xN$, *Appl. Phys. Lett.* 91(23), 231913 (2007)

18. X. G. Guo, P. Tong, J. C. Lina, C. Yang, K. Zhang, M. Wang, Y. Wu, S. Lin, W. H. Song, and Y. P. Sun, Large negative thermal expansion in$(Ga_{0.7}Cu_{0.3})_{1-x}Mn_xNMn_3$ ($x \leq 0.4$), compensating for the thermal expansion of cryogenic materials, *Scr. Mater.* 128, 74 (2017)
19. R. J. Huang, Y. Y. Liu, W. Fan, J. Tan, F. R. Xiao, L. H. Qian, and L. F. Li, Giant negative thermal expansion in $NaZn_{13}$-type La(Fe, Si, Co)$_{13}$ compounds, *J. Am. Chem. Soc.* 135(28), 11469 (2013)
20. W. T. Sun, H. Zhang, W. Li, R. J. Huang, Y. Q. Zhao, W. Wang, and L. F. Li, Controllable negative thermal expansion in $NaZn_{13}$-type La(Fe, Co, Al)$_{13}$ compounds, *AIP Adv.* 10(7), 075123 (2020)
21. X. R. Xing, J. X. Deng, J. Chen, and G. R. Liu, Novel thermal expansion of lead titanate, *Rare Met.* 22(4), 294 (2003)
22. H. Fang, Y. Wang, S. Shang, and Z. K. Liu, Nature of ferroelectric–paraelectric phase transition and origin of negative thermal expansion in $PbTiO_3$, *Phys. Rev. B* 91(2), 024104 (2015)
23. E. T. Ritz and N. A. Benedek, Interplay between phonons and anisotropic elasticity drives negative thermal expansion in $PbTiO_3$, *Phys. Rev. Lett.* 121(22), 255901 (2018)
24. Y. W. Long, N. Hayashi, T. Saito, M. Azuma, S. Muranaka, and Y. Shimakawa, Temperature-induced A–B intersite charge transfer in an A-site-ordered $LaCu_3Fe_4O_{12}$ perovskite, *Nature* 458(7234), 60 (2009)
25. M. Azuma, W. T. Chen, H. Seki, M. Czapski, S. Olga, K. Oka, M. Mizumaki, T. Watanuki, N. Ishimatsu, N. Kawamura, S. Ishiwata, M. G. Tucker, Y. Shimakawa, and J. P. Attfield, Colossal negative thermal expansion in $BiNiO_3$ induced by intermetallic charge transfer, *Nat. Commun.* 2(1), 347 (2011)
26. A. P. Giddy, M. T. Dove, G. S. Pawley, and V. Heine, The determination of rigid-unit modes as potential soft modes for displacive phase transitions in framework crystal structures, *Acta Crystallogr Sec. A: Found. Crystallogr.* A49, 697 (1993)
27. L. Goodwin, Rigid unit modes and intrinsic flexibility in linearly bridged framework structures, *Phys. Rev. B* 74(13), 134302 (2006)
28. M. T. Dove, Flexibility of network materials and the Rigid Unit Mode model: A personal perspective, *Phil. Trans. R. Soc. A* 377(2149), 20180222 (2019)
29. W. Kim, S. H. Kang, and Y. K. Kwon, Rigid unit modes in sp-sp(2) hybridized carbon systems: Origin of negative thermal expansion, *Phys. Rev. B* 92(24), 245434 (2015)
30. J. Z. Tao and A. W. Sleight, The role of rigid unit modes in negative thermal expansion, *J. Solid State Chem.* 173(2), 442 (2003)
31. K. D. Hammonds, A. Bosenick, M. T. Dove, and V. Heine, Rigid unit modes in crystal structures with octahedrally coordinated atoms, *Am. Mineral.* 83(5–6), 476 (1998)
32. A. K. A. Pryde, K. D. Hammonds, M. T. Dove, V. Heine, J. D. Gale, and M. C. Warren, Origin of the negative thermal expansion in ZrW_2O_8 and ZrV_2O_7, *J. Phys.: Condens. Matter* 8(50), 10973 (1999)
33. L. H. N. Rimmer and M. T. Dove, Simulation study of negative thermal expansion in yttrium tungstate $Y_2W_3O_{12}$, *J. Phys.: Condens. Matter* 27(18), 185401 (2015)
34. A. Sanson, F. Rocca, G. Dalba, P. Fornasini, R. Grisenti, M. Dapiaggi, and G. Artioli, Negative thermal expansion and local dynamics in Cu_2O and Ag_2O, *Phys. Rev. B* 73(21), 214305 (2006)
35. L. H. N. Rimmer, M. T. Dove, B. Winkler, D. J. Wilson, K. Refson, and A. L. Goodwin, Framework flexibility and the negative thermal expansion mechanism of copper (I) oxide Cu_2O, *Phys. Rev. B* 89(21), 214115 (2014)
36. C. W. Li, X. Tang, J. A. Munöz, J. B. Keith, S. J. Tracy, D. L. Abernathy, and B. Fultz, Structural relationship between negative thermal expansion and quartic anharmonicity of cubic ScF_3, *Phys. Rev. Lett.* 107(19), 195504 (2011)
37. C. P. Romao, Anisotropic thermal expansion in flexible materials, *Phys. Rev. B* 96(13), 134113 (2017)
38. E. Grüneisen, Theory of the solid state of monoatomic elements, *Ann. Phys.* 344(12), 257 (1912)
39. N. Mounet and N. Marzari, First-principles determination of the structural, vibrational and thermodynamical properties of diamond, graphite, and derivatives, *Phys. Rev. B* 71(20), 205214 (2005)
40. Z. Y. Wang, Y. L. Zhou, X. Q. Wang, F. Wang, Q. Sun, Z. X. Guo, and Y. Jia, Effects of in-plane stiffness and charge transfer on thermal expansion of monolayer transition metal dichalcogenide, *Chin. Phys. B* 24(2), 026501 (2015)
41. R. M. Hazen and A. Y. Au, High-pressure crystal chemistry of phenakite (Be_2SiO_4) and bertrandite ($Be_4Si_2O_7(OH)_2$), *Phys. Chem. Miner.* 13(2), 69 (1986)
42. R. Stevens, B. F. Woodfield, J. Boerio-Goates, and M. K. Crawford, Heat capacities, third-law entropies and thermodynamic functions of the negative thermal expansion material Zn_2GeO_4 from T =(0 to 400) K, *J. Chem. Thermodyn.* 36(5), 349 (2004)
43. H. L. Yuan, Q. L. Gao, P. Xu, J. Guo, L. H. He, A. Sanson, M. J. Chao, and E. J. Liang, Understanding negative thermal expansion of Zn_2GeO_4 through local structure and vibrational dynamics, *Inorg. Chem.* 60(3), 1499 (2021)
44. J. Q. Wang, P. Xu, H. L. Yuan, Q. L. Gao, Q. Sun, and E. J. Liang, Negative thermal expansion driven by acoustic phonon modes in rhombohedral Zn_2GeO_4, *Results Phys.* 19, 103531 (2020)
45. J. N. Plendl and L. C. Mansur, Anomalous thermal expansion with infrared spectroscopy, *Appl. Opt.* 11(5), 1194 (1972)
46. M. Vaccari, R. Grisenti, P. Fornasini, F. Rocca, and A. Sanson, Negative thermal expansion in CuCl: An extended X-ray absorption fine structure study, *Phys. Rev. B* 75(18), 184307 (2007)
47. A. M. Gopakumar, M. K. Gupta, R. Mittal, S. Rolsd, and S. L. Chaplot, Investigating anomalous thermal expansion of copper halides by inelastic neutron scattering and *ab initio* phonon calculations, *Phys. Chem. Chem. Phys.* 19(19), 12107 (2017)

48. T. H. K. Barron and R. W. Munn, Analysis of the thermal expansion of anisotropic solids: Application to zinc, *Philos. Mag.* 15(133), 85 (1967)

49. C. Ablitt, S. Craddock, M. S. Senn, A. A. Mostofi, and N. C. Bristowe, The origin of uniaxial negative thermal expansion in layered perovskites, *npj Comput. Mater.* 3, 44 (2017)

50. N. Mounet and N. Marzari, First-principles determination of the structural, vibrational and thermodynamical properties of diamond, graphite, and derivatives, *Phys. Rev. B* 71(20), 205214 (2005)

51. G. Lucazeau, Effect of pressure and temperature on Raman spectra of solids: Anharmonicity, *J. Raman Spectrosc.* 34(7–8), 478 (2003)

52. L. C. Gallington, K. W. Chapman, C. R. Morelock, P. J. Chupas, and A. P. Wilkinson, Dramatic softening of the negative thermal expansion material HfW_2O_8 upon heating through its WO_4 orientational order–disorder phase transition, *J. Appl. Phys.* 115(5), 053512 (2014)

53. S. Allen and J. S. O. Evans, Negative thermal expansion and oxygen disorder in cubic $ZrMo_2O_8$, *Phys. Rev. B* 68(13), 134101 (2003)

54. A. Kennedy, M. A. White, A. P. Wilkinson, and T. Varga, Low thermal conductivity of the negative thermal expansion material, $HfMo_2O_8$, *Appl. Phys. Lett.* 90(15), 151906 (2007)

55. J. S. O. Evans, T. A. Mary, and A. W. Sleight, Negative thermal expansion materials, *Physica B* 241, 311 (1998)

56. M. G. Tucker, A. L. Goodwin, M. T. Dove, D. A. Keen, S. A. Wells, and J. S. O. Evans, Negative thermal expansion in ZrW_2O_8: Mechanisms, rigid unit modes, and neutron total scattering, *PRL* 95(22), 255501 (2005)

57. D. Cao, F. Bridges, G. R. Kowach, and A. P. Ramirez, Frustrated softmodes and negative thermal expansion in ZrW_2O_8, *Phys. Rev. Lett.* 89(21), 215902 (2002)

58. F. Cao, F. Bridges, G. R. Kowach, and A. P. Ramirez, Correlated atomicmotions in the negative thermal expansion material ZrW_2O_8: A local structure study, *Phys. Rev. B* 68(1), 014303 (2003)

59. F. Bridges, T. Keiber, P. Juhas, S. J. L. Billinge, L. Sutton, J. Wilde, and G. R. Kowach, Local vibrations and negative thermal expansion in ZrW_2O_8, *Phys. Rev. Lett.* 112(4), 045505 (2014)

60. T. R. Ravindran, A. K. Arora, and T. A. Mary, High-pressure Raman spectroscopic study of zirconium tungstate, *J. Phys.: Condens. Matter* 13(50), 11573 (2001)

61. E. J. Liang, Y. Liang, Y. Zhao, J. Liu, and Y. J. Jiang, Low frequency phonon modes and negative thermal expansion in $A(MO_4)_2$ (A=Zr, Hf and M=W, Mo) by Raman and terahertz time-domain spectroscopy, *J. Phys. Chem. A* 112(49), 12582 (2008)

62. J. N. Hancock, C. Turpen, Z. Schlesinger, G. R. Kowach, and A. P. Ramirez, Unusual low-energy phonon dynamics in the negative thermal expansion compound ZrW_2O_8, *Phys. Rev. Lett.* 93(22), 225501 (2004)

63. V. Gava, A. L. Martinotto, and C. A. Perottoni, First-principles mode Gruneisen parameters and negative thermal expansion in α-ZrW_2O_8, *Phys. Rev. Lett.* 109(19), 195503 (2012)

64. M. K. Gupta, R. Mittal, and S. L. Chaplot, Negative thermal expansion in cubic ZrW_2O_8: Role of phonons in the entire Brillouin zone from *ab initio* calculations, *Phys. Rev. B* 88(1), 014303 (2013)

65. N. Khosrovani, A. W. Sleight, and T. Vogt, Structure of ZrV_2O_7 from –263 to 470 °C, *J. Solid State Chem.* 132(2), 355 (1997)

66. C. Turquat, C. Muller, E. Nigrelli, C. Leroux, J. L. Soubeyroux, and G. Nihoul, Structural investigation of temperature-induced phase transitions in HfV_2O_7, *Eur. Phys. J. Appl. Phys.* 10(1), 15 (2000)

67. R. L. Withers, J. S. O. Evans, J. Hanson, and A. W. Sleight, An *in situ* temperature-dependent electron and X-ray diffraction study of structural phase transitions in ZrV_2O_7, *J. Solid State Chem.* 137(1), 161 (1998)

68. L. C. Gallington, B. R. Hester, B. S. Kaplan, and A. P. Wilkinson, Pressure-dependence of the phase transitions and thermal expansion in zirconium and hafnium pyrovanadate, *J. Solid State Chem.* 249, 46 (2017)

69. V. Korthuis, N. Khosrovani, A. W. Sleight, N. Roberts, R. Dupree, and W. W. Warren, Negative thermal expansion and phase transitions in the $ZrV_{2-x}P_xO_7$ series, *Chem. Mater.* 7(2), 412 (1995)

70. P. P. Sahoo, S. Sumithra, G. Madras, and T. N. G. Row, Synthesis, structure, negative thermal expansion, and photocatalytic property of Mo doped ZrV_2O_7, *Inorg. Chem.* 50(18), 8774 (2011)

71. H. L. Yuan, B. H. Yuan, F. Li, and E. J. Liang, Phase transition and thermal expansion properties of $ZrV_{2-x}P_xO_7$, *Acta Physica Sinica* 61(22), 226502 (2012)

72. Q. Q. Liu, J. Yang, X. J. Sun, X. N. Cheng, H. Tang, and H. H. Li, Influence of W doped ZrV_2O_7 on structure, negative thermal expansion property and photocatalytic performance, *Appl. Surf. Sci.* 313, 41 (2014)

73. H. Yanase, H. Chida, and H. Kobayashi, Fabrication and negative thermal expansion properties of P-substituted ZrV_2O_7 sintered bodies, *J. Eur. Ceram. Soc.* 38(1), 221 (2018)

74. T. Hisashige, T. Yamaguchi, T. Tsuji, and Y. Yamamura, Phase transition of $Zr_{1-x}Hf_xV_2O_7$ solid solutions having negative thermal expansion, *J. Ceram. Soc. Jpn.* 114(1331), 607 (2006)

75. T. Yanase, T. Kojima, and H. Kobayashi, Effects of Nb and Y substitution on negative thermal expansion of $ZrV_{2-x}P_xO_7$ ($0 \leq x \leq 0.8$), *Solid State Commun.* 151(8), 595 (2011)

76. B. H. Yuan, H. L. Yuan, W. B. Song, X. S. Liu, Y. G. Cheng, M. J. Chao, and E. J. Liang, High solubility of hetero-valence ion (Cu^{2+}) for reducing phase transition and thermal expansion of $ZrV_{1.6}P_{0.4}O_7$, *Chin. Phys. Lett.* 31(7), 076501 (2014)

77. B. H. Yuan, X. S. Liu, W. B. Song, Y. G. Cheng, M. J. Chao, and E. J. Liang, High substitution of Fe^{3+} for Zr^{4+} in $ZrV_{1.6}P_{0.4}O_7$ with small amount of $FeV_{0.8}P_{0.2}O_4$ for low thermal expansion, *J. Phys. Lett. A* 378(45), 3397 (2014)
78. P. Wang, Q. D. Chen, S. L. Li, Y. J. Ji, W. Y. Mu, W. W. Feng, G. J. Zeng, Y. W. Liu, and E. J. Liang, Phase transition and near-zero thermal expansion of $Zr_{0.5}Hf_{0.5}VPO_7$, *Chin. Phys. B* 27(6), 066501 (2018)
79. P. Wang, Q. D. Chen, S. L. Li, Y. J. Ji, G. J. Zeng, Y. W. Liu, and E. J. Liang, Phase transition and near-zero thermal expansion properties of $Zr_{0.5}Hf_{0.5}V_{2-x}P_xO_7$ ($0\leq x \leq 1.2$), *Solid State Commun.* 287, 7 (2019)
80. B. H. Yuan, W. S. Cao, X. H. Ge, Y. G. Cheng, X. S. Liu, and E. J. Liang, Substitutions of dual-ion Al^{3+}/Mo^{6+} for Zr^{4+}/V^{5+}in ZrV_2O_7 for realizing near-zero thermal expansion, *Acta Physica Sinica* 66(7), 076501 (2017)
81. B. H. Yuan, X. S. Liu, Y. C. Mao, J. Q. Wang, J. Guo, Y. G. Cheng, W. B. Song, E. J. Liang, and M. J. Chao, Low thermal expansion over a wide temperature range of $Zr_{1-x}Fe_xV_{2-x}Mo_xO_7$ ($0\leq x \leq 0.9$), *Mater. Chem. Phys.* 170, 162 (2016)
82. W. Wei, Q. L. Gao, J. Guo, M. J. Chao, L. H. He, J. Chen, and E. J. Liang, Realizing isotropic negative thermal expansion covering room temperature by breaking the superstructure of ZrV_2O_7, *Appl. Phys. Lett.* 116(18), 181902 (2020)
83. R. Mittal and S. L. Chaplot, Lattice dynamical calculation of negative thermal expansion in ZrV_2O_7 and HfV_2O_7, *Phys. Rev. B* 78(17), 174303 (2008)
84. M. Maczka, W. Paraguassu, A. G. S. Filho, P. T. C. Freire, J. M. Filho, F. E. A. Melo, and J. Hanuza, High-pressure Raman study of $Al_2(WO_4)_3$, *J. Solid State Chem.* 177(6), 2002 (2004)
85. G. J. Zeng, H. L. Yuan, J. Guo, Q. Sun, Q. L. Gao, M. J. Chao, X. Ren, and E. J. Liang, Hydrate formation and its effects on the thermal expansion properties of $HfMgW_3O_{12}$, *Phys. Chem. Chem. Phys.* 22(22), 12605 (2020)
86. J. Pommer, V. Kataev, K. Y. Choi, P. Lemmens, A. Ionescu, Y. Pashkevich, A. Freimuth, and G. Güntherodt, Interplay between structure and magnetism in the spin-chain compound $(Cu, Zn)_2V_2O_7$, *Phys. Rev. B* 67(21), 214410 (2003)
87. M. Schindler and F. C. Hawthorne, Structural characterization of the β-$Cu_2V_2O_7$–α-$Zn_2V_2O_7$ solid solution, *J. Solid State Chem.* 146(1), 271 (1999)
88. B. V. Slobodin and R. F. Samigullina, Thermoanalytical study of the polymorphism and melting behavior of $Cu_2V_2O_7$, *Inorg. Mater.* 46(2), 196 (2010)
89. K. Katayama, K. Otsuka, M. Mitamura, Y. Yokoyama, Y. Okamoto, and K. Takenaka, Microstructural effects on negative thermal expansion extending over a wide temperature range in β-$Cu_{1.8}Zn_{0.2}V_2O_7$, *Appl. Phys. Lett.* 113(18), 181902 (2018)
90. L. Wang, J. Werner, A. Ottmann, R. Weis, M. Abdel-Hafiez, J. Sannigrahi, S. Majumdar, C. Koo, and R. Klingeler, Magnetoelastic coupling and ferromagnetic-type in-gap spin excitations in multiferroic α-$Cu_2V_2O_7$, *New J. Phys.* 20(6), 063045 (2018)
91. K. Shi, A. Sanson, A. Venier, L. L. Fan, C. L. Sun, X. R. Xing, and J. Chen, Negative and zero thermal expansion in α-$(Cu_{2-x}Zn_x)V_2O_7$ solid solutions, *Chem. Commun. (Camb.)* 56(73), 10666 (2020)
92. M. Sato, V. Warne-Lang, Y. Kadowaki, N. Katayama, Y. Okamoto, and K. Takenaka, Sol–gel synthesis of doped $Cu_2V_2O_7$ fine particles showing giant negative thermal expansion, *AIP Adv.* 10(7), 075207 (2020)
93. Y. W. Lee, T. H. Jang, S. E. Dissanayake, S. Lee, and Y. H. Jeong, Magnetism and magnetoelectricity in the polar oxide α-$Cu_2V_2O_7$, *Europhys. Lett.* 113(2), 27007 (2016)
94. H. Wang, M. Yang, M. Chao, J. Guo, Q. Gao, Y. Jiao, X. Tang, and E. Liang, Negative thermal expansion property of β-$Cu_2V_2O_7$, *Solid State Ion.* 343, 115086 (2019)
95. H. Wang, M. Yang, M. Chao, J. Guo, X. Tang, Y. Jiao, and E. Liang, Negative thermal expansion properties of $Cu_{1.5}Mg_{0.5}V_2O_7$, *Ceram. Int.* 45(8), 9814 (2019)
96. K. Takenaka, Y. Okamoto, T. Shinoda, N. Katayama, and Y. Sakai, Colossal negative thermal expansion in reduced layered ruthenate, *Nat. Commun.* 8(1), 14102 (2017)
97. K. Takenaka, N. Inoue, Y. Mizuno, Y. Okamoto, N. Katayama, Y. Sakai, T. Nishikubo, and M. Azuma, Extended operating temperature window of giant negative thermal expansion in Sn-doped Ca_2RuO_4, *Appl. Phys. Lett.* 113(7), 071902 (2018)
98. S. Xu, Y. M. Hu, Y. Liang, C. F. Shi, Y. L. Su, J. Guo, Q. L. Gao, M. J. Chao, and E. J. Liang, Negative thermal expansion of Ca_2RuO_4 with oxygen vacancies, *Chin. Phys. B* 29(8), 086501 (2020)
99. A. K. Tyagi, S. N. Achary, and M. D. Mathews, Phase transition and negative thermal expansion in $A_2(MoO_4)_3$ system (A = Fe^{3+}, Cr^{3+} and Al^{3+}), *J. Alloys Compd.* 339(1–2), 207 (2002)
100. T. Varga, J. L. Moats, S. V. Ushakov, and A. Navrotsky, Thermochemistry of $A_2M_3O_{12}$ negative thermal expansion materials, *J. Mater. Res.* 22(9), 2512 (2007)
101. X. S. Liu, B. H. Yuan, Y. G. Cheng, E. J. Liang, and W. F. Zhang, Combined influences of A^{3+} and Mo^{6+} on monoclinic–orthorhombic phase transition of negative-thermal-expansion $A_2Mo_3O_{12}$, *J. Alloys Compd.* 776, 236 (2019)
102. G. Yang, X. S. Liu, X. W. Sun, E. J. Liang, and W. F. Zhang, Synthesis process control of low-thermal-expansion $Fe_2W_3O_{12}$ by suppressing the intermediate phase Fe_2WO_6, *Ceram. Int.* 44(17), 22032 (2018)
103. Z. P. Zhang, W. K. Sun, H. F. Liu, B. T. Xiao, X. H. Zeng, and X. B. Chen, Densification and negative thermal expansion property of $In_{0.5}Sc_{1.5}(MoO_4)_3$ ceramics, *J. Alloys Compd.* 783, 77 (2019)
104. T. Suzuki and A. Omote, Negative thermal expansion in $(HfMg)(WO_4)_3$, *J. Am. Ceram. Soc.* 87(7), 1365 (2004)
105. B. A. Marinkovic, P. M. Jardim, M. Ari, R. R. de Avillez, F. Rizzo, and F. F. Ferreira, Low positive thermal expansion in $HfMgMo_3O_{12}$, *Phys. Status Solidi. (b)* 245(11), 2514 (2008)
106. W. B. Song, E. J. Liang, X. S. Liu, Z. Y. Li, B. H. Yuan, and J. Q. Wang, A negative thermal expansion material of $ZrMgMo_3O_{12}$, *Chin. Phys. Lett.* 30(12), 126502 (2013)

107. F. Li, X. S. Liu, W. B. Song, B. Yuan, Y. G. Cheng, H. L. Yuan, F. X. Cheng, M. J. Chao, and E. liang, Phase transition, crystal water and low thermal expansion behavior of $Al_{2-2x}(ZrMg)_xW_3O_{12}\cdot n(H_2O)$, *Solid State Chem.* 218, 15 (2014)

108. X. H. Ge, Y. C. Mao, L. Li, L. P. Li, N. Yuan, Y. G. Cheng, J. Guo, M. J. Chao, and E. J. Liang, Phase transition and negative thermal expansion property of $ZrMnMo_3O_{12}$, *Chin. Phys. Lett.* 33(4), 046503 (2016)

109. Y. Y. Liu, B. H. Yuan, Y. G. Cheng, E. J. Liang, X. H. Ge, H. L. Yuan, Y. Zhang, J. Guo, and M. J. Chao, Phase transition and negative thermal expansion of $HfMnMo_3O_{12}$, *Mater. Res. Bull.* 99, 255 (2018)

110. X. H. Ge, X. S. Liu, Y. G. Cheng, B. H. Yuan, D. X. Chen, M. J. Chao, J. Guo, J. Q. Wang, and E. J. Liang, Negative thermal expansion and photoluminescence properties in a novel material $ZrScW_2PO_{12}$, *J. Appl. Phys.* 120(20), 205101 (2016)

111. Y. G. Cheng, Y. Liang, X. H. Ge, X. S. Liu, B. H. Yuan, J. Guo, M. J. Chao, and E. J. Liang, A novel material of $HfScMo_2VO_{12}$ with negative thermal expansion and intense white-light emission, *RSC Advances* 6(59), 53657 (2016)

112. Y. G. Cheng, Y. Liang, Y. C. Mao, X. H. Ge, B. H. Yuan, J. Guo, M. J. Chao, and E. J. Liang, A novel material of $HfScW_2PO_{12}$ with negative thermal expansion from 140 K to 1469 K and intense blue photoluminescence, *Mater. Res. Bull.* 85, 176 (2017)

113. X. Chen, B. H. Yuan, Y. G. Cheng, X. H. Ge, Y. Jia, E. J. Liang, and M. J. Chao, Phase transition and near-zero thermal expansion in $ZrFeMo_2VO_{12}$, *Phys. Lett. A* 380(48), 4070 (2016)

114. D. X. Chen, Y. Zhang, X. H. Ge, Y. G. Cheng, Y. Y. Liu, H. L. Yuan, J. Guo, M. J. Chao, and E. J. Liang, Structural, vibrational and thermal expansion properties of $Sc_2W_4O_{15}$, *Phys. Chem. Chem. Phys.* 20(27), 20160 (2018)

115. Y. Liang, Y. G. Cheng, X. H. Ge, B. H. Yuan, J. Guo, Q. Sun, and E. J. Liang, Negative thermal expansion and photoluminescence in solid solution $(HfSc)_{0.83}W_{2.25}P_{0.83}O_{12-\delta}$, *Chin. Phys. B* 26(10), 106501 (2017)

116. L. Wang, F. Wang, P. F. Yuan, Q. Sun, E. J. Liang, Y. Jia, and Z. X. Guo, Negative thermal expansion correlated with polyhedral movements and distortions in orthorhombic $Y_2Mo_3O_{12}$, *Mater. Res. Bull.* 48(7), 2724 (2013)

117. H. L. Yuan, C. Y. Wang, Q. L. Gao, X. H. Ge, H. Sun, S. H. Lapidus, J. Guo, M. J. Chao, Y. Jia, and E. J. Liang, Structure and negative thermal expansion in $Zr_{0.3}Sc_{1.7}Mo_{2.7}V_{0.3}O_{12}$, *Inorg. Chem.* 59(6), 4090 (2020)

118. T. G. Amos, A. Yokochi, and A. W. Sleight, Phase transition and negative thermal expansion in tetragonal $NbOPO_4$, *J. Solid State Chem.* 141(1), 303 (1998)

119. T. G. Amos and A. W. Sleight, Negative thermal expansion in orthorhombic $NbOPO_4$, *J. Solid State Chem.* 160(1), 230 (2001)

120. X. Wang, Q. Huang, J. Deng, R. Yu, J. Chen, and X. Xing, Phase transformation and negative thermal expansion in $TaVO_5$, *Inorg. Chem.* 50(6), 2685 (2011)

121. J. Wang, J. Deng, R. Yu, J. Chen, and X. Xing, Coprecipitation synthesis and negative thermal expansion of $NbVO_5$, *Dalton Trans.* 40(13), 3394 (2011)

122. N. P. Salke, M. K. Gupta, R. Rao, R. Mittal, J. Deng, and X. Xing, Raman and *ab initio* investigation of negative thermal expansion material $TaVO_5$: Insights into phase stability and anharmonicity, *J. Appl. Phys.* 117(23), 235902 (2015)

123. N. P. Salke, R. Rao, S. N. Achary, C. Nayak, A. B. Garg, P. S. R. Krishna, A. B. Shinde, S. N. Jha, D. Bhattacharyya, Jagannath, and A. K. Tyagi, High pressure phases and amorphization of a negative thermal expansion compound $TaVO_5$, *Inorg. Chem.* 57(12), 6973 (2018)

124. M. Ivanda, D. Waasmaier, A. Endriss, J. Ihringer, A. Kirfel, and W. Kiefer, Low-temperature anomalies of cuprite observed by Raman spectroscopy and X-ray powder diffraction, *J. Raman Spectrosc.* 28(7), 487 (1997)

125. A. Sanson, G. Dalba, P. Fornasini, R. Grisenti, F. Rocca, G. Artioli, M. Dapiaggi, and W. Tiano, EXAFS and XRD study of local dynamics in Cu_2O and Ag_2O, *Phys. Scr. T* 115, 271 (2005)

126. S. A. Beccara, G. Dalba, P. Fornasini, R. Grisenti, A. Sanson, and F. Rocca, Local thermal expansion in a cuprite structure: The case of Ag_2O, *Phys. Rev. Lett.* 89(2), 025503 (2002)

127. M. K. Gupta, R. Mittal, S. Rols, and S. L. Chaplot, Inelastic neutron scattering an *ab–initio* calculation of negative thermal expansion in Ag_2O, *Physica B* 407(12), 2146 (2012)

128. T. Lan, C. W. Li, J. L. Niedziela, H. Smith, D. L. Abernathy, G. R. Rossman, and B. Fultz, Anharmonic lattice dynamics of Ag_2O studied by inelastic neutron scattering and first-principles molecular dynamics simulations, *Phys. Rev. B* 89(5), 054306 (2014)

129. G. Wallez, N. Clavier, N. Dacheux, and D. Bregiroux, Negative thermal expansion in $Th_2O(PO_4)_2$, *Mater. Res. Bull.* 46(11), 1777 (2011)

130. J. Xu, L. Hu, Y. Song, F. Han, Y. Qiao, J. Deng, J. Chen, and X. Xing, Zero thermal expansion in cubic $MgZrF_6$, *J. Am. Ceram. Soc.* 100(12), 5385 (2017)

131. B. R. Hester and A. P. Wilkinson, Negative thermal expansion, response to pressure and phase transitions in $CaTiF_6$, *Inorg. Chem.* 57(17), 11275 (2018)

132. M. T. Dove, J. Du, A. E. Phillips, D. A. Keen, and M. G. Tucker, A real-space experimental model for negative thermal expansion in scandium trifluoride, arXiv: 1905.09250 (2019)

133. Y. Oba, T. Tadano, R. Akashi, and S. Tsuneyuki, First-principles study of phonon anharmonicity and negative thermal expansion in ScF_3, *Phys. Rev. Mater.* 3(3), 033601 (2019)

134. D. Bocharov, M. Krack, Y. Rafalskij, A. Kuzmin, and J. Purans, *Ab initio* molecular dynamics simulations of negative thermal expansion in ScF_3: The effect of the supercell size, *Comput. Mater. Sci.* 171, 109198 (2020)

135. M. K. Gupta, B. Singh, R. Mittal, and S. L. Chaplot, Negative thermal expansion behavior in $MZrF_6$ (M = Ca, Mg, Sr): *Ab initio* lattice dynamical studies, *Phys. Rev. B* 98(1), 014301 (2018)

136. T. A. Bird, J. Woodland-Scott, L. Hu, M. T. Wharmby, J. Chen, A. L. Goodwin, and M. S. Senn, Anharmonicity and scissoring modes in the negative thermal expansion materials ScF_3 and $CaZrF_6$, *Phys. Rev. B* 101(6), 064306 (2020)

137. A. Sanson, M. Giarola, G. Mariotto, L. Hu, J. Chen, and X. R. Xing, Lattice dynamics and anharmonicity of $CaZrF_6$ from Raman spectroscopy and *ab initio* calculations, *Mater. Chem. Phys.* 180, 213 (2016)

138. T. Chatterji, T. C. Hansen, M. Brunelli, and P. F. Henry, Negative thermal expansion of ReO_3 in the extended temperature range, *Appl. Phys. Lett.* 94(24), 241902 (2009)

139. Y. M. Liu, Z. H. Wang, M. Wu, Q. Sun, M. J. Chao, and Y. Jia, Negative thermal expansion in isostructural cubic ReO_3 and ScF_3: A comparative study, *Comput. Mater. Sci.* 107, 157 (2015)

140. A. L. Goodwin, M. Calleja, M. J. Conterio, M. T. Dove, J. S. O. Evans, D. A. Keen, L. Peters, and M. G. Tucker, Colossal positive and negative thermal expansion in the framework material $Ag_3[Co(CN)_6]$, *Science* 319(5864), 794 (2008)

141. L. Gao, N. K. Shi, Q. Sun, A. Sanson, R. Milazzo, A. Carnera, H. Zhu, S. H. Lapidus, Y. Ren, Q. Huang, J. Chen, and X. Xing, Low-frequency phonon driven negative thermal expansion in cubic $GaFe(CN)_6$ Prussian blue analogues, *Inorg. Chem.* 57(17), 10918 (2018)

142. L. Gao, Y. Sun, N. Shi, R. Milazzo, S. Pollastri, L. Olivi, Q. Huang, H. Liu, A. Sanson, Q. Sun, E. Liang, X. Xing, and J. Chen, Large isotropic negative thermal expansion in water-free Prussian blue analogues of $ScCo(CN)_6$, *Scr. Mater.* 187, 119 (2020)

143. P. Ding, E. J. Liang, Y. Jia, and Z. Y. Du, Electronic structure, bonding and phonon modes in the negative thermal expansion materials of $Cd(CN)_2$ and $Zn(CN)_2$, *J. Phys.: Condens. Matter* 20(24), 275224 (2008)

144. Z. Y. Du, E. J. Liang, P. Ding, J. P. Wang, and E. M. Xu, Lattice vibrational analysis of the negative thermal expansion materials of $Zn(CN)_2$ and $Zn(CN)_2$, *Chin. J. Light Scatt.* 20(2),145 (2008)

145. J. Hibble, A. M. Chippindale, E. Marelli, S. Kroeker, V. K. Michaelis, B. J. Greer, P. M. Aguiar, E. J. Bilbe, E. R. Barney, and A. C. Hannon, Local and average structure in zinc cyanide: Toward an understanding of the atomistic origin of negative thermal expansion, *J. Am. Chem. Soc.* 135(44), 16478 (2013)

146. M. K. Gupta, B. Singh, R. Mittal, M. Zbiri, A. B. Cairns, A. L. Goodwin, H. Schober, and S. L. Chaplot, Anomalous thermal expansion, negative linear compressibility, and high-pressure phase transition in $ZnAu_2(CN)_4$: Neutron inelastic scattering and lattice dynamics studies, *Phys. Rev. B* 96(21), 214303 (2017)

147. M. Mittal, H. Zbiri, E. Schober, S. J. Marelli, A. M. Hibble, A. M. Chippindale, and S. L. Chaplot, Relationship between phonons and thermal expansion in $Zn(CN)_2$ and $Ni(CN)_2$ from inelastic neutron scattering and *ab initio* calculations, *Phys. Rev. B* 83(2), 024301 (2011)

148. H. Fang, M. T. Dove, L. H. N. Rimmer, and A. J. Misquitta, Simulation study of pressure and temperature dependence of the negative thermal expansion in $Zn(CN)_2$, *Phys. Rev. B* 88(10), 104306 (2013)

149. J. Hibble, A. M. Chippindale, A. H. Pohl, and A. C. Hannon, Surprises from a simple material — The structure and properties of nickel cyanide, *Angew. Chem. Int. Ed.* 46(37), 7116 (2007)

150. A. M. Chippindale, S. J. Hibble, E. Marelli, E. J. Bilbé, A. C. Hannon, and M. Zbiri, Chemistry and structure by design: Ordered $CuNi(CN)_4$ sheets with copper(ii) in a square-planar environment, *Dalton Trans.* 44(25), 12502 (2015)

151. S. d'Ambrumenil, M. Zbiri, A. M. Chippindale, and S. J. Hibble, Phonon dynamics in the layered negative thermal expansion compounds $Cu_xNi_{2-x}(CN)_4$, *Phys. Rev. B* 100(9), 094312 (2019)

152. M. Li, Y. Li, C. Y. Wang, and Q. Sun, Negative thermal expansion of $GaFe(CN)_6$ and effect of Na insertion by first-principles calculations, *Chin. Phys. Lett.* 36(6), 066301 (2019)

153. Y. Li, Q. L. Gao, D. H. Chang, P. J. Sun, J. Z. Liu, Y. Jia, E. J. Liang, and Q. Sun, Effect of bond on negative thermal expansion of Prussian blue analogues $MCo(CN)_6$ (M = Fe, Ti and Sc): A first-principles study, *J. Phys.: Condens. Matter* 32(45), 455703 (2020)

154. P. Kroll, M. Andrade, X. Yan, E. Ionescu, G. Miehe, and R. Riedel, Isotropic negative thermal expansion in β-$Si(NCN)_2$ and itsorigin, *J. Phys. Chem. C* 116(1), 526 (2012)

155. L. Li, K. Refson, and M. T. Dove, Negative thermal expansion of cubic silicon dicarbodiimide, $Si(NCN)_2$, studied by *ab initio* lattice dynamics, *J. Phys.: Condens. Matter* 32(46), 465402 (2020)

156. D. Dubbeldam, K. S. Walton, D. Ellis, and R. Snurr, Exceptional negative thermal expansion in isoreticular metal–organic frameworks, *Angew. Chem. Int. Ed.* 119(24), 4580 (2007)

157. S. S. Han, and W. A. Goddard, Metal-organic frameworks provide large negative thermal expansion behavior, *J. Phys. Chem. C* 111(42), 15185 (2007)

158. W. Zhou, H. Wu, T. Yildirim, J. R. Simpson, and A. R. H. Walker, Originof the exceptional negative thermal expansion in metal–organic framework-5 Zn_4O(1, 4-benzenedicarboxylate)$_3$, *Phys. Rev. B* 78(5), 054114 (2008)

159. N. Lock, M. Christensen, Y. Wu, V. K. Peterson, M. K. Thomsen, R. O. Piltz, A. J. Ramirez-Cuesta, G. J. McIntyre, K. Norén, R. Kutteh, C. J. Kepert, G. J. Kearley, and B. B. Iversen, Scrutinizing negative thermal expansion in MOF-5 by scattering techniques and *ab initio* calculations, *Dalton Trans.* 42(6), 1996 (2013)

160. L. H. N. Rimmer, M. T. Dove, A. L. Goodwin, and D. C. Palmer, Acoustic phonons and negative thermal expansion in MOF-5, *Phys. Chem. Chem. Phys.* 16(39), 21144 (2014)

161. Y. Wu, A. Kobayashi, G. Halder, V. Peterson, K. Chapman, N. Lock, P. Southon, and C. Kepert, Negative thermal expansion in the metal–organic framework material Cu_3(1, 3, 5-benzenetricarboxylate)$_2$, *Angew. Chem. Int. Ed.* 47(46), 8929 (2008)

162. W. L. Queen, C. M. Brown, D. K. Britt, P. Zajdel, M. R. Hudson, and O. M. Yaghi, Site specific CO_2 adsorption and zero thermal expansion in ananisotropic pore network, *J. Phys. Chem. C* 115(50), 24915 (2011)

163. S. Henke, A. Schneemann, and R. A. Fischer, Massive anisotropic thermal expansion and thermo-responsive breathing in metal–organic frameworks modulated by linker functionalization, *Adv. Funct. Mater.* 23(48), 5990 (2013)

164. Z. N. Liu, Q. Li, H. Zhu, K. Lin, J. X. Deng, J. Chen, and X. Xing, 3D negative thermal expansion in orthorhombic MIL-68(In), *Chem. Commun. (Camb.)* 54(45), 5712 (2018)

165. F. X. Coudert and J. D. Evans, Nanoscale metamaterials: Meta-MOFs and framework materials with anomalous behavior, *Coord. Chem. Rev.* 388, 48 (2019)

166. Z. Y. Wang, Y. L. Zhou, X. Q. Wang, F. Wang, Q. Sun, Z. X. Guo, and Y. Jia, Effects of in-plane stiffness and charge transfer on thermal expansion of monolayer transition metal dichalcogenide, *Chin. Phys. B* 24(2), 026501 (2015)

167. D. Kumar, B. Singh, P. Kumar, V. Balakrishnan, and P. Kumar, Thermal expansion coefficient and phonon dynamics in coexisting allotropes of monolayer WS_2 probed by Raman scattering, *J. Phys.: Condens. Matter* 31(50), 505403 (2019)

168. Y. Aierken, D. Cakir, C. Sevik, and F. M. Peeters, Thermal properties of black and blue phosphorenes from a first-principles quasiharmonic approach, *Phys. Rev. B* 92(8), 081408 (2015)

169. L. Wang, C. Wang, and Y. Chen, Black phosphorene exhibiting negative thermal expansion and negative linear compressibility, *J. Phys.: Condens. Matter* 31(46), 465003 (2019)

170. H. Sun, G. Liu, Q. Li, and X. G. Wan, First-principles study of thermal expansion and thermomechanics of single-layer black and blue phosphorus, *Phys. Lett. A* 380(24), 2098 (2016)

171. X. J. Ge, K. L. Yao, and J. T. Lü, Comparative study of phonon spectrum and thermal expansion of graphene, silicene, germanene, and blue phosphorene, *Phys. Rev. B* 94(16), 165433 (2016)

172. P. R. Shaina, L. George, V. Yadav, and M. Jaiswal, Estimating the thermal expansion coefficient of graphene: The role of graphene-substrate interactions, *J. Phys.: Condens. Matter* 28(8), 085301 (2016)

173. C. W. Kim, S. H. Kang, and Y. K. Kwon, Rigid unit modes in sp-sp2 hybridized carbon systems: Origin of negative thermal expansion, *Phys. Rev. B* 92(24), 245434 (2015)

174. A. I. Lebedev, Negative thermal expansion in CdSe quasi-two-dimensional nanoplatelets, *Phys. Rev. B* 100(3), 035432 (2019)

175. Y. Hu, J. Chen, and B. Wang, On the intrinsic ripples and negative thermal expansion of graphene, *Carbon* 95, 239 (2015)

176. H. Sun, G. Liu, Q. Li, and X. G. Wan, First-principles study of thermal expansion and thermomechanics of single-layer black and blue phosphorus, *Phys. Lett. A* 380(24), 2098 (2016)

177. C. W. Kim, S. H. Kang, and Y. K. Kwon, Rigid unit modes in sp-sp2 hybridized carbon systems: Origin of negative thermal expansion, *Phys. Rev. B* 92(24), 245434 (2015)

178. Y. X. Gao, C. Y. Wang, Q. L. Gao, J. Guo, M. J. Chao, Y. Jia, and E. J. Liang, Zero thermal expansion in $Ta_2Mo_2O_{11}$ by compensation effects, *Inorg. Chem.* 59(24), 18427 (2020)

179. C. Guillaume, Recherches sur les aciers au nickel, Dilatations auxtemperatures elevees, resistance electrique, *CR Acad. Sci.* 125(235), 18 (1897)

180. R. J. Weiss, The origin of the "Invar" effect, *Proc. Phys. Soc.* 82(2), 281 (1963)

181. T. Moriya and K. Usami, Magneto-volume effect and invar phenomena in ferromagnetic metals, *Solid State Commun.* 34(2), 95 (1980)

182. H. Yamada, Metamagnetic transition and susceptibility maximum in an itinerant-electron system, *Phys. Rev. B* 47(17), 11211 (1993)

183. H. Akai and P. H. Dederichs, Local moment disorder in ferromagnetic alloys, *Phys. Rev. B* 47(14), 8739 (1993)

184. V. Crisan, P. Entel, H. Ebert, H. Akai, D. D. Johnson, and J. B. Staunton, Magnetochemical origin for Invar anomalies in iron–nickel alloys, *Phys. Rev. B* 66(1), 014416 (2002)

185. Y. Wang, G. M. Stocks, D. M. C. Nicholson, W. A. Shelton, V. P. Antropov, and B. N. Harmon, Noncollinear magnetic structure in $Ni_{0.35}Fe_{0.65}$, *J. Appl. Phys.* 81(8), 3873 (1997)

186. M. Schilfgaarde, I. A. Abrikosov, and B. Johansson, Origin of the Invar effect in iron–nickel alloys, *Nature* 400(6739), 46 (1999)

187. H. Yamada, Pressure effect in an itinerant-electron metamagnet at finite temperature, *J. Magn. Magn. Mater.* 139(1–2), 162 (1995)

188. G. G. Lonzarich and L. TaiUefer, Effect of spin fluctuations on the magnetic equation of state of ferromagnetic or nearly ferromagnetic metals, *J. Phys. (Paris)* 18, 4339 (1985)

189. T. Moriya, Spin Fluctuations in Itinerant Electron Magnetism, Springer-Verlag, Berlin, 1985

190. A. V. Andreev, F. R. de Boer, T. H. Jacobs, and K. H. J. Buschow, Thermal expansion anomalies and spontaneous magnetostriction in $R_2Fe_{17}C_x$ intermetallic compounds, *Physica B* 175(4), 361 (1991)

191. Y. M. Hao, X. M. Zhang, B. W. Wang, Y. Z. Yuang, and F. Wang, Anomalous thermal expansion and magnetic properties of $Tm_2Fe_{17-x}Cr_x$ compounds, *J. Appl. Phys.* 108(2), 023915 (2010)

192. P. Álvarez-Alonso, P. Gorria, J. A. Blanco, J. Sánchez-Marcos, G. J. Cuello, I. Puente-Orench, J. A. Rodríguez-Velamazán, G. Garbarino, I. dePedro, J. R. Fernández, and J. L. S. Llamazares, Magnetovolume and magnetocaloric effects in Er_2Fe_{17}, *Phys. Rev. B* 86, 184411 (2012)
193. D. Givord and R. Lemaire, Magnetic transition and anomalous thermal expansion in R_2Fe_{17} compounds, *IEEE Trans. Magn.* 10(2), 109 (1974)
194. R. J. Huang, Y. Liu, W. Fan, J. Tan, F. Xiao, L. Qian, and L. Li, Giant negative thermal expansion in $NaZn_{13}$-type La(Fe, Si, Co)$_{13}$ compounds, *J. Am. Chem. Soc.* 135(28), 11469 (2013)
195. B. Li, X. H. Luo, H. Wang, W. J. Ren, S. Yano, C. W. Wang, J. S. Gardner, K. D. Liss, P. Miao, S. H. Lee, T. Kamiyama, R. Q. Wu, Y. Kawakita, and Z. D. Zhang, Colossal negative thermal expansion induced by magnetic phase competition on frustrated lattices in Laves phase compound (Hf, Ta)Fe_2, *Phys. Rev. B* 93(22), 224405 (2016)
196. Y. Song, J. Chen, X. Liu, C. Wang, Q. Gao, Q. Li, L. Hu, J. Zhang, S. Zhang, and X. Xing, Structure, magnetism, and tunable negative thermal expansion in (Hf, Nb)Fe_2 alloys, *Chem. Mater.* 29(17), 7078 (2017)
197. L. F. Li, P. Tong, Y. M. Zou, W. Tong, W. B. Jiang, Y. Jiang, X. K. Zhang, J. C. Lin, M. Wang, C. Yang, X. B. Zhu, W. H. Song, and Y. P. Sun, Good comprehensive performance of Laves phase $Hf_{1-x}Ta_xFe_2$ as negative thermal expansion materials, *Acta Mater.* 161, 258 (2018)
198. H. Yibole, A. K. Pathak, Y. Mudryk, F. Guillou, N. Zarkevich, S. Gupta, V. Balema, and V. K. Pecharsky, Manipulating the stability of crystallographic and magnetic sub-lattices: A first-order magnetoelastic transformation in transition metal based Laves phase, *Acta Mater.* 154, 365 (2018)
199. K. Takenaka and H. Takagi, Giant negative thermal expansion in Ge-doped anti-perovskite manganese nitrides, *Appl. Phys. Lett.* 87(23), 261902 (2005)
200. K. Takenaka, K. Asano, M. Misawa, and H. Takagi, Negative thermal expansion in Ge-free antiperovskite manganese nitrides: Tin-doping effect, *Appl. Phys. Lett.* 92(1), 011927 (2008)
201. C. Wang, Y. Sun, Y. C. Wen, L. H. Chu, and M. Nie, Investigation of lattice contraction in Mn_3XN (X=Zn, Cu, Sn), *Mater. Sci. Forum* 638–642, 2195 (2010)
202. R. J. Huang, L. F. Li, F. S. Cai, X. D. Xu, and L. H. Qian, Low-temperature negative thermal expansion of the antiperovskite manganese nitride Mn_3CuN codoped with Ge and Si, *Appl. Phys. Lett.* 93(8), 081902 (2008)
203. T. Hamada and K. Takenaka, Giant negative thermal expansion in antiperovskite manganese nitrides, *J. Appl. Phys.* 109(7), 07E309 (2011)
204. K. Takenaka and H. Takagi, Zero thermal expansion in a pure-form antiperovskite manganese nitride, *Appl. Phys. Lett.* 94(13), 131904 (2009)
205. C. Wang, L. H. Chu, Q. R. Yao, Y. Sun, M. M. Wu, L. Ding, J. Yan, Y. Y. Na, W. H. Tang, G. N. Li, Q. Huang, and J. W. Lynn, Tuning the range, magnitude, and sign of the thermal expansion in intermetallic $Mn_3(Zn, M)_xN$ (M = Ag, Ge), *Phys. Rev. B* 85(22), 220103 (2012)
206. E. F. Wasserman, in: Ferromagnetic Materials, ed. K. H. J. Buschow and E. P. Wohlfartht, Elsevier Science Publishers B. V., Ch. 3, Vol. 5, pp 238–322, 1990
207. E. F. Wassermann, The Invar problem, *J. Magn. Magn. Mater.* 100(1–3), 346 (1991)
208. M. Shiga, Invar alloys, *Curr. Opin. Solid State Mater. Sci.* 1(3), 340 (1996)
209. J. Chen, L. Hu, J. Deng, and X. Xing, Negative thermal expansion in functional materials: Controllable thermal expansion by chemical modifications, *Chem. Soc. Rev.* 44(11), 3522 (2015)
210. S. Khmelevskyi, I. Turek, and P. Mohn, Large negative magnetic contribution to the thermal expansion in iron-platinum alloys: Quantitative theory of the Invar effect, *Phys. Rev. Lett.* 91(3), 037201 (2003)
211. D. D. Johnson and W. A. Shelton, in: The Invar effect: A centennial symposium, Ed. J. Wittenauer, The Minerals, Metals and Materials Society, Warrendale, PA, pp 63–74, 1997
212. M. Shiga and Y. Nakamura, Magnetovolume effects and Invar characters of $(Zr_{1-x}Nb_x)Fe_2$, *J. Phys. Soc. Jpn.* 47(5), 1446 (1979)
213. H. Wada and M. Shigaand, Thermal expansion anomaly and Invar effect of $Mn_{1-x}Co_xB$, *J. Magn. Magn. Mater.* 104–107, 1925 (1992)
214. A. G. Kuchin, I. V. Medvedeva, V. S. Gaviko, and V. A. Kazantsev, Magnetovolume properties of $Y_2Fe_{17-x}M_x$ alloys (M = Si orAl), *J. Alloys Compd.* 289(1–2), 18 (1999)
215. P. Álvare, P. Gorria, J. S. Marcos, I. P. Orench, J. A. R. Velamazán, G. Cuello, J. L. S. Llamazares, and J. A. Blanco, Magnetic structure and magneto-volume anomalies in Er_2Fe_{17} compound, *J. Phys.: Conf. Ser.* 325, 01 (2011)
216. A. Shuitcev, R. N. Vasin, A. M. Balagurov, L. Li, I. A. Bobrikov, and Y. X. Tong, Thermal expansion of martensite in $Ti_{29.7}Ni_{50.3}Hf_{20}$ shape memory alloy, *Intermetallics* 125, 106889 (2020)
217. I. S. Winter, J. Montoya, K. A. Persson, and D. C. Chrzan, *Ab initio* calculation of thermal expansion with application to understanding Invar behavior in gum metal, *Phys. Rev. Mater.* 2(7), 073601 (2018)
218. R. Li, R. Huang, W. Wang, H. Liu, Y. Han, C. Huang, and L. Li, Low-temperature negative thermal expansion property of Mn doped La(Fe, Si)$_{13}$ compounds, *J. Alloys Compd.* 628, 308 (2015)
219. F. Shen, H. Zhou, F. Hu, J. T. Wang, S. Deng, B. Wang, H. Wu, Q. Huang, J. Wang, J. Chen, L. He, J. Hao, Z. Yu, F. Liang, T. Liang, J. Sun, and B. Shen, Cone-spiral magnetic ordering dominated lattice distortion and giant-negative thermal expansion in Fe-doped MnNiGe compounds, *Mater. Horiz.* 7(3), 804 (2020)
220. J. Xu, X. Zheng, S. Yang, L. Xi, S. Wang, L. Zhang, W. Yang, J. Yang, X. Ma, D. Chen, L. He, S. Deng, J. Zhang, Y. Wu, and B. Shen, Large linear negative thermal expansion in NiAs-type magnetic intermetallic Cr−Te−Se compounds, *Inorg. Chem.* 59(12), 8603 (2020)
221. L. Y. Hao, T. Yang, and M. Tan, Negative thermal expansion and spontaneous magnetostriction of $Nd_2Fe_{16.5}Cr_{0.5}$ compound, *Chin. Phys. Lett.* 37(1), 016501 (2020)

222. Y. Yan, J. Yang, N. Zhao, G. Yao, X. Fu, Y. Zhang, and W. Cui, Large negative thermal expansion and magnetoelastic coupling in metamagnetic tetragonal (Mn, T)$_2$Sb (T = Cr, V) alloys, *J. Supercond. Nov. Magn.* 33(9), 2551 (2020)

223. J. H. Belo, A. L. Pires, I. T. Gomes, V. Andrade, J. B. Sousa, R. L. Hadimani, and C. David, Giant negative thermal expansion at the nanoscale in the multifunctional material Gd$_5$(Si, Ge)$_4$, *Phys. Rev. B* 100(13), 134303 (2019)

224. Y. Z. Song, Q. Sun, T. Yokoyama, H. H. Zhu, Q. Li, R. J. Huang, Y. Ren, Q. Z. Huang, X. R. Xing, and J. Chen, Transforming thermal expansion from positive to negative: The case of cubic magnetic compounds of (Zr, Nb)Fe$_2$, *J. Phys. Chem. Lett.* 11(5), 1954 (2020)

225. Y. Z. Song, Q. Sun, M. Xu, J. Zhang, Y. Q. Hao, Y. Q. Qiao, S. T. Zhang, Q. Z. Huang, X. R. Xing, and J. Chen, Negative thermal expansion in (Sc, Ti)Fe$_2$ induced by an unconventional magnetovolume effect, *Mater. Horiz.* 7(1), 275 (2020)

226. T. Yokoyama, A. Koide, and Y. Uemura, Local thermal expansions and lattice strains in Elinvar and stainless steel alloys, *Phys. Rev. Mater.* 2(2), 023601 (2018)

227. X. Y. Song, Z. G. Sun, Q. Z. Huang, M. Rettenmayr, X. M. Liu, M. Seyring, G. N. Li, G. G. Rao, and F. X. Yin, Adjustable zero thermal expansion in antiperovskite manganese nitride, *Adv. Mater.* 23(40), 4690 (2011)

228. M. Kobayashi and M. Mochizuki, Theory of magnetism-driven negative thermal expansion in inverse perovskite antiferromagnets, *Phys. Rev. Mater.* 3(2), 024407(2019)

229. K. Takenaka, M. Ichigo, T. Hamada, A. Ozawa, T. Shibayama, T. Inagaki, and K. Asano, Magnetovolume effects in manganese nitrides with antiperovskite structure, *Sci. Technol. Adv. Mater.* 15(1), 015009 (2014)

230. H. Lu, Y. Sun, S. Deng, K. Shi, L. Wang, W. Zhao, H. Han, S. Deng, and C. Wang, Tunable negative thermal expansion and structural evolution in antiperovskite $Mn_3Ga_{1-x}Ge_xN$ ($0 \leq x \leq 1.0$), *J. Am. Ceram. Soc.* 100(12), 5739 (2017)

231. S. Tan, C. Gao, C. Wang, T. Zhou, G. Yin, M. Sun, F. Xing, R. Cao, and Y. Sun, The tunable negative thermal expansion covering a wide temperature range around room temperature in Sn, Mn co-substituted Mn_3ZnN, *Dalton Trans.* 49(27), 10407 (2020)

232. S. Iikubo, K. Kodama, K. Takenaka, H. Takagi, M. Takigawa, and S. Shamoto, Local lattice distortion in the giant negative thermal expansion material $Mn_3Cu_{1-x}Ge_xN$, *Phys. Rev. Lett.* 101(20), 205901 (2008)

233. P. Tong, D. Louca, G. King, A. Llobet, J. C. Lin, and Y. P. Sun, Magnetic transition broadening and local lattice distortion in the negative thermal expansion antiperovskite $Cu_{1-x}Sn_xNMn_3$, *Appl. Phys. Lett.* 102(4), 041908 (2013)

234. J. C. Lin, P. Tong, X. J. Zhou, H. Lin, Y. W. Ding, Y. X. Bai, L. Chen, X. G. Guo, C. Yang, B. Song, Y. Wu, S. Lin, W. H. Song, and Y. P. Sun, Giant negative thermal expansion covering room temperature in nanocrystalline-GaN_xMn_3, App, *Phys. Lett.* 107, 131902 (2015)

235. J. Tan, R. Huang, W. Wang, W. Li, Y. Zhao, S. Li, Y. Han, C. Huang, and L. Li, Broad negative thermal expansion operation-temperature window in antiperovskite manganese nitride with small crystallites, *Nano Res.* 8(7), 2302 (2015)

236. B. Paul, S. Chatterjee, A. Roy, A. Midya, P. Mandal, V. Grover, and A. K. Tyagi, Geometrically frustrated $GdInO_3$: An exotic system to study negative thermal expansion and spin-lattice coupling, *Phys. Rev. B* 95(5), 054103 (2017)

237. P. Miao, X. Lin, A. Koda, S. Lee, Y. Ishikawa, S. Torii, M. Yonemura, T. Mochiku, H. Sagayama, S. Itoh, K. Ikeda, T. Otomo, Y. Wang, R. Kadono, and T. Kamiyama, Large magnetovolume effect induced by embedding ferromagnetic clusters into antiferromagnetic matrix of cobaltite perovskite, *Adv. Mater.* 29(24), 1605991 (2017)

238. B. Ranjbar and B. J. Kennedy, Unusual thermal expansion of Sr_2IrO_4: A variable temperature synchrotron X-ray diffraction study, *J. Solid State Chem.* 232, 178 (2015)

239. M. S. Senn, A. Bombardi, C. A. Murray, C. Vecchini, A. Scherillo, X. Luo, and S. W. Cheong, Negative thermal expansion in hybrid improper ferroelectric Ruddlesden–Popper perovskites by symmetry trapping, *Phys. Rev. Lett.* 114(3), 035701 (2015)

240. S. C. Abrahams, S. K. Kurtz, and P. B. Jamieson, Atomic displacement relationship to Curie temperature and spontaneous polarization in displacive ferroelectrics, *Phys. Rev.* 172(2), 551 (1968)

241. J. Chen, F. Wang, Q. Huang, L. Hu, X. Song, J. Deng, R. Yu, and X. Xing, Effectively control negative thermal expansion of single-phase ferroelectrics of $PbTiO_3$-(Bi, La)FeO_3 over a giant range, *Sci. Rep.* 3(1), 2458 (2013)

242. J. Chen, K. Nittala, J. S. Forrester, J. L. Jones, J. X. Deng, R. Yu, and X. R. Xing, The role of spontaneous polarization in the negative thermal expansion of tetragonal $PbTiO_3$-based compounds, *J. Am. Chem. Soc.* 133(26), 11114 (2011)

243. P. E. Janolin, P. Bouvier, J. Kreisel, P. A. Thomas, I. A. Kornev, L. Bellaiche, W. Crichton, M. Hanfland, and B. Dkhil, High-pressure effect on $PbTiO_3$: An investigation by Raman and X-ray scattering up to 63 GPa, *Phys. Rev. Lett.* 101(23), 237601 (2008)

244. L. Wang, P. Yuan, F. Wang, E. Liang, Q. Sun, Z. Guo, and Y. Jia, First-principles study of tetragonal $PbTiO_3$: Phonon and thermal expansion, *Mater. Res. Bull.* 49, 509 (2014)

245. H. Fang, Y. Wang, S. Shang, and Z. K. Liu, Nature of ferroelectric–paraelectric phase transition and origin of negative thermal expansion in $PbTiO_3$, *Phys. Rev. B* 91(2), 024104 (2015)

246. D. Zhou, W. Tan, W. Xiao, M. Song, M. Chen, X. Xiong, and J. Xu, Structural properties of $PbVO_3$ perovskites under hydrostatic pressure conditions up to 10.6 GPa, *J. Phys.: Condens. Matter* 24(43), 435403 (2012)

247. K. Oka, T. Yamauchi, S. Kanungo, T. Shimazu, K. Ohishi, Y. Uwatoko, M. Azuma, and T. Saha-Dasgupta, Experimental and theoretical studies of the metallic conductivity in cubic $PbVO_3$ under high pressure, *J. Phys. Soc. Jpn.* 87(2), 024801 (2018)

248. T. Ogata, K. Oka, and M. Azuma, Negative thermal expansion in electron doped $PbVO_{3-x}F_x$, *Appl. Phys. Express* 12(2), 023005 (2019)

249. T. Ogata, Y. Sakai, H. Yamamoto, S. Patel, P. Keil, J. Koruza, S. Kawaguchi, Z. Pan, T. Nishikubo, J. Rödel, and M. Azuma, Melting of d_{xy} orbital ordering accompanied by suppression of giant tetragonal distortion and insulator-to-metal transition in Cr-substituted $PbVO_3$, *Chem. Mater.* 31(4), 1352 (2019)

250. H. Ishizaki, Y. Sakai, T. Nishikubo, Z. Pan, K. Oka, H. Yamamoto, and M. Azuma, Negative thermal expansion in lead-free La-substituted $Bi_{0.5}Na_{0.5}VO_3$, *Chem. Mater.* 32(11), 4832 (2020)

251. M. Rong, M. Li, J. Chen, M. Zhou, K. Lin, L. Hu, W. Yuan, W. Duan, J. Deng, and X. Xing, Large negative thermal expansion in non-perovskitelead-free ferroelectric $Sn_2P_2S_6$, *Phys. Chem. Chem. Phys.* 18(8), 6247 (2016)

252. T. Chattopadhyay, J. X. Boucherle, and H. G. von Schnering, Neutron diffraction study on the structural phase transition in GeTe, *J. Phys. C: Solid State Phys.* 20(10), 1431 (1987)

253. T. Chatterji, C. M. N. Kumar, and U. D. Wdowik, Anomalous temperature-induced volume contraction in GeTe, *Phys. Rev. B* 91(5), 054110 (2015)

254. Đ. Dangić, A. R. Murphy, É. D. Murray, S. Fahy, and I. Savić, Coupling between acoustic and soft transverse optical phonons leads to negative thermal expansion of GeTe near the ferroelectric phase transition, *Phys. Rev. B* 97(22), 224106 (2018)

255. R. D. Shannon, Revised effective ionic radii and systematic studies of interatomic distances in halides and chalcogenides, *Acta Crystallogr. A* 32(5), 751 (1976)

256. J. Arvanitidis, K. Papagelis, S. Margadonna, K. Prassides, and A. N. Fitch, Temperature-induced valence transition and associated lattice collapse in samarium fulleride, *Nature* 425(6958), 599 (2003)

257. S. Margadonna, J. Arvanitidis, K. Papagelis, and K. Prassides, Negative thermal expansion in the mixed valence ytterbium fulleride, $Yb_{2.75}C_{60}$, *Chem. Mater.* 17(17), 4474 (2005)

258. A. Jayaraman, P. Dernier, and L. D. Longinotti, Study of valence transition in SmS induced by alloying, temperature, and pressure, *Phys. Rev. B* 11(8), 2783 (1975)

259. K. Takenaka, D. Asai, R. Kaizu, Y. Mizuno, Y. Yokoyama, Y. Okamoto, N. Katayama, H. S. Suzuki, and Y. Imanaka, Giant isotropic negative thermal expansion in Y-doped samarium monosulfides by intra-atomic charge transfer, *Sci. Rep.* 9(1), 122 (2019)

260. D. Asai, Y. Mizuno, H. Hasegawa, Y. Yokoyama, Y. Okamoto, N. Katayama, H. S. Suzuki, Y. Imanaka, and K. Takenaka, Valence fluctuations and giant isotropic negative thermal expansion in $Sm_{1-x}R_xS$ (R = Y, La, Ce, Pr, Nd), *Appl. Phys. Lett.* 114(14), 141902 (2019)

261. D. G. Mazzone, M. Dzero, A. M. M. Abeykoon, H. Yamaoka, H. Ishii, N. Hiraoka, J. P. Rueff, J. M. Ablett, K. Imura, H. S. Suzuki, J. N. Hancock, and I. Jarrige, Kondo-induced giant isotropic negative thermal expansion, *Phys. Rev. Lett.* 124(12), 125701 (2020)

262. H. Li, S. Lv, Z. Wang, Y. Xia, Y. Bai, X. Liu, and J. Meng, Machanism of A-B intersite charge transfer and negative thermal expansion in A-site-ordered perovskite $LaCu_3Fe_4O_{12}$, *J. Appl. Phys.* 111(10), 103718 (2012)

263. K. Yamada, K. Shiro, H. Etani, S. Marukawa, N. Hayashi, M. Mizumaki, Y. Kusano, S. Ueda, H. Abe, and T. Irifune, Valence transitions in negative thermal expansion material $SrCu_3Fe_4O_{12}$, *Inorg. Chem.* 53(19), 10563 (2014)

264. M. W. Shimakawa, M. W. Lufaso, and P. M. Woodward, Negative and positive thermal expansion-like volume changes due to intermetallic charge transfer based on an ionic crystal model of transition-metal oxides, *APL Mater.* 6(8), 086106 (2018)

265. Z. Liu, Z. Wang, D. Chang, Q. Sun, M. Chao, and Y. Jia, Charge transfer induced negative thermal expansion in perovskite $BiNiO_3$, *Comput. Mater. Sci.* 113, 198 (2016)

266. M. Naka, H. Seo, and Y. Motome, Theory of valence transition in $BiNiO_3$, *Phys. Rev. Lett.* 116(5), 056402 (2016)

267. E. Pachoud, J. Cumby, J. Wright, B. Raguž, R. Glaum, and J. P. Attfield, Charge order and negative thermal expansion in V_2OPO_4, *J. Am. Chem. Soc.* 140(2), 636 (2018)

268. E. Pachoud, J. Cumby, J. Wright, B. Raguz, R. Glaumc, and J. P. Attfield, Electronic origin of negative thermal expansion in V_2OPO_4, *Chem. Commun. (Camb.)* 56(48), 6523 (2020)

269. K. Nabetani, Y. Muramatsu, K. Oka, K. Nakano, H. Hojo, M. Mizumaki, A. Agui, Y. Higo, N. Hayashi, M. Takano, and M. Azuma, Suppression of temperature hysteresis in negative thermal expansion compound $BiNi_xFe_xO_3$ and zero-thermal expansion composite, *Appl. Phys. Lett.* 106(6), 061912 (2015)

270. S. Yamada, S. Marukawa, M. Murakami, and S. Mori, "True" negative thermal expansion in Mn-doped $LaCu_3Fe_4O_{12}$ perovskite oxides, *Appl. Phys. Lett.* 105(23), 231906 (2014)

271. E. E. McCabe, E. Bousquet, C. P. J. Stockdale, C. A. Deacon, T. T. Tran, P. S. Halasyamani, M. C. Stennett, and N. C. Hyatt, Proper ferroelectricity in the Dion–Jacobson material $CsBi_2Ti_2NbO_{10}$: Experiment and theory, *Chem. Mater.* 27(24), 8298 (2015)

272. M. J. Pitcher, P. Mandal, M. S. Dyer, J. Alaria, P. Borisov, H. Niu, J. B. Claridge, and M. J. Rosseinsky, Tilt engineering of spontaneous polarization and magnetization above 300 K in a bulk layered perovskite, *Science* 347(6220), 420 (2015)

273. J. Mangeri, K. C. Pitike, S. P. Alpay, and S. Nakhmanson, Amplitudon and phason modes of electrocaloric energy interconversion, *npj Comput. Mater.* 2(1), 16020 (2016)

274. Y. Kimura, Y. Tomioka, H. Kuwahara, A. Asamitsu, M. Tamura, and Y. Tokura, Interplane tunneling magnetoresistance in a layered manganite crystal, *Science* 274(5293), 1698 (1996)

275. L. F. Huang, X. Z. Lu, and J. M. Rondinelli, Tunable negative thermal expansion in layered perovskites from quasi-two-dimensional vibrations, *Phys. Rev. Lett.* 117(11), 115901 (2016)

276. T. Vogt and D. Buttrey, Temperature dependent structural behavior of Sr_2RhO_4, *J. Solid State Chem.* 123(1), 186 (1996)

277. B. Ranjbar and B. J. Kennedy, Anisotropic thermal expansion in Sr_2RhO_4 — A variable temperature synchrotron X-ray diffraction study, *Solid State Sci.* 49, 43 (2015)

278. J. Takahashi and N. Kamegashira, X-ray structural study of calcium manganese oxide by Rietveld analysis at high temperatures, *MRS Bull.* 28(6), 565 (1993)

279. M. S. Senn, A. Bombardi, C. A. Murray, C. Vecchini, A. Scherillo, X. Luo, and S. W. Cheong, Negative thermal expansion in hybrid improper ferroelectric Ruddlesden–Popper perovskites by symmetry trapping, *Phys. Rev. Lett.* 114(3), 035701 (2015)

280. K. J. Cordrey, M. Stanczyk, C. A. L. Dixon, K. S. Knight, J. Gardner, F. D. Morrison, and P. Lightfoot, Structural and dielectric studies of the phase behaviour of the topological ferroelectric $La_{1-x}Nd_xTaO_4$, *Dalton Trans.* 44(23), 10673 (2015)

281. J. W. Zhang, A. S. McLeod, Q. Han, X. Chen, H. A. Bechtel, Z. Yao, S. N. Gilbert Corder, T. Ciavatti, T. H. Tao, M. Aronson, G. L. Carr, M. C. Martin, C. Sow, S. Yonezawa, F. Nakamura, I. Terasaki, D. N. Basov, A. J. Millis, Y. Maeno, and M. Liu, Nano-resolved current-induced insulator–metal transition in the Mott insulator Ca_2RuO_4, *Phys. Rev. X* 9(1), 011032 (2019)

282. G. Zhang and E. Pavarini, Mott transition, spin–orbit effects, and magnetism in Ca_2RuO_4, *Phys. Rev. B* 95(7), 075145 (2017)

283. Q. Han and A. Millis, Lattice energetics and correlation-driven metal–insulator transitions: The case of Ca_2RuO_4, *Phys. Rev. Lett.* 121(6), 067601 (2018)

284. M. Braden, G. Andre, S. Nakatsuji, and Y. Maeno, Crystal and magnetic structure of Ca_2RuO_4: Magnetoelastic coupling and the metal–insulator transition, *Phys. Rev. B* 58(2), 847 (1998)

285. O. Friedt, M. Braden, G. Andre, P. Adelmann, S. Nakatsuji, and Y. Maeno, Structural and magnetic aspects of the metal–insulator transition in $Ca_{2-x}Sr_xRuO_4$, *Phys. Rev. B* 63(17), 174432 (2001)

286. A. S. Alexander, G. Cao, V. Dobrosavljevic, S. McCall, J. E. Crow, E. Lochner, and R. P. Guertin, Destruction of the Mott insulating ground state of Ca_2RuO_4 by a structural transition, *Phys. Rev. B* 60(12), R8422 (1999)

287. T. F. Qi, O. B. Korneta, S. Parkin, L. E. De Long, P. Schlottmann, and G. Cao, Negative volume thermal expansion via orbital and magnetic orders in $Ca_2Ru_{1-x}Cr_xO_4$ ($0 < x < 0.13$), *Phys. Rev. Lett.* 105(17), 177203 (2010)

288. T. F. Qi, O. B. Korneta, S. Parkin, J. P. Hu, and G. Cao, Magnetic and orbital orders coupled to negative thermal expansion in Mott insulators $Ca_2Ru_{1-x}M_xO_4$ (M = Mn and Fe), *Phys. Rev. B* 85(16), 165143 (2012)

289. K. Takenaka, T. Shinoda, N. Inoue, Y. Okamoto, N. Katayama, Y. Sakai, T. Nishikubo, and M. Azuma, Giant negative thermal expansion in Fe-doped layered ruthenate ceramics, *Appl. Phys. Express* 10(11), 115501 (2017)

290. Y. G. Cheng, Y. C. Mao, B. H. Yuan, X. H. Ge, J. Guo, M. J. Chao, and E. J. Liang, Enhanced negative thermal expansion and optical absorption of $In_{0.6}(HfMg)_{0.7}Mo_3O_{12}$ with oxygen vacancies, *Phys. Lett. A* 381(24), 2195 (2017)

291. J. Zegkinoglou, J. Strempfer, C. S. Nelson, J. P. Hill, J. Chakhalian, C. Bernhard, J. C. Lang, G. Srajer, H. Fukazawa, S. Nakatsuji, Y. Maeno, and B. Keimer, Orbital ordering transition in Ca_2RuO_4 observed with resonant X-ray diffraction, *Phys. Rev. Lett.* 95(13), 136401 (2005)

292. M. C. Lee, C. H. Kim, I. Kwak, J. Kim, S. Yoon, B. C. Park, B. Lee, F. Nakamura, C. Sow, Y. Maeno, T. W. Noh, and K. W. Kim, Abnormal phase flip in the coherent phonon oscillations of Ca_2RuO_4, *Phys. Rev. B* 98(16), 161115 (2018)

293. M. C. Lee, C. H. Kim, I. Kwak, C. W. Seo, C. H. Sohn, F. Nakamura, C. Sow, Y. Maeno, E. A. Kim, T. W. Noh, and K. W. Kim, Strong spin–phonon coupling unveiled by coherent phonon oscillations in Ca_2RuO_4, *Phys. Rev. B* 99(14), 144306 (2019)

294. V. Sivasubramanian, T. R. Ravindran, R. Nithya, and A. K. Arora, Structural phase transition in indium tungstate, *J. Appl. Phys.* 96(1), 387 (2004)

295. B. A. Marinkovic, M. Ari, P. M. Jardim, R. R. de Avillez, F. Rizzo, and F. F. Ferreira, $In_2Mo_3O_{12}$: A low negative thermal expansion compound, *Thermochim. Acta* 499(1–2), 48 (2010)

296. J. S. O. Evans, T. A. Mary, and A. W. Sleight, Negative thermal expansion in $Sc_2(WO_4)_3$, *J. Solid State Chem.* 137(1), 148 (1998)

297. J. S. O. Evans and T. A. Mary, Structural phase transitions and negative thermal expansion in $Sc_2(MoO_4)_3$, *Inter. J. Inorg. Mater.* 2(1), 143 (2000)

298. H. Liu, W. Sun, Z. Zhang, X. Zhang, Y. Zhou, J. Zhua, and X. Zeng, Tailored phase transition temperature and negative thermal expansion of Sc-substituted $Al_2Mo_3O_{12}$ synthesized by a co-precipitation method, *Inorg. Chem. Front.* 6(7), 1842 (2019)

299. H. F. Liu, Z. P. Zhang, J. Ma, J. Zhu, and X. H. Zeng, Effect of isovalent substitution on phase transition and negative thermal expansion of $In_{2-x}Sc_xW_3O_{12}$ ceramics, *Ceram. Int.* 41(8), 9873 (2015)

300. Y. G. Cheng, Y. C. Mao, X. S. Liu, B. H. Yuan, M. J. Chao, and E. J. Liang, Near-zero thermal expansion of $In_{2(1-x)}(HfMg)_xMo_3O_{12}$ with tailored phase transition, *Chin. Phys. B* 25(8), 086501 (2016)

301. W. B. Song, B. H. Yuan, X. S. Liu, Z. Y. Li, J. Q. Wang, and E. J. Liang, Tuning the monoclinic-to-orthorhombic phase transition temperature of $Fe_2Mo_3O_{12}$ by substitutional coincorporation of Zr^{4+} and Mg^{2+}, *Mater. Res.* 29(7), 849 (2014)

302. W. B. Song, J. Q. Wang, Z. Y. Li, X. S. Liu, B. H. Yuan, and E. J. Liang, Phase transition and thermal expansion property of $Cr_{2-x}Zr_{0.5x}Mg_{0.5x}Mo_3O_{12}$ solid solution, *Chin. Phys. B* 23(6), 066501 (2014)

303. K. J. Miller, C. P. Romao, M. Bieringer, B. A. Marinkovic, L. Prisco, and M. A. White, Near-zero thermal expansion in $In(HfMg)_{0.5}Mo_3O_{12}$, *J. Am. Ceram. Soc.* 96(2), 561 (2013)

304. S. L. Li, X. H. Ge, H. L. Yuan, D. X. Chen, J. Guo, R. F. Shen, M. J. Chao, and E. J. Liang, Near-zero thermal expansion and phase transitions in $HfMg_{1-x}Zn_xMo_3O_{12}$, *Front. Chem.* 6, 115 (2018)

305. A. Madrid, P. I. Ponton, F. Garcia, M. B. Johnson, M. A. White, and B. A. Marinkovic, Solubility limit of Zn^{2+} in low thermal expansion $ZrMgMo_3O_{12}$ and its influence on phase transition temperature, *Ceram. Int.* 46(3), 3979 (2020)

306. R. F. Shen, B. H. Yuan, S. L. Li, X. H. Ge, J. Guo, and E. J. Liang, Near-zero thermal expansion of $Zr_xHf_{1-x}MgMo_3O_{12}$ in a larger temperature range, *Optik (Stuttg.)* 165, 1 (2018)

307. S. Sumithra and A. M. Umarji, Role of crystal structure on the thermal expansion of $Ln_2W_3O_{12}$ (Ln =La, Nd, Dy, Y, Er and Yb), *Solid State Sci.* 6(12), 1313 (2004)

308. X. L. Xiao, Y. Z. Cheng, J. Peng, M. M. Wu, D. F. Chen, Z. B. Hu, R. Kiyanagi, J. S. Fieramosca, S. Short, and J. Jorgensen, Thermal expansion properties of $A_2(MO_4)_3$ (A = Ho and Tm; M=W and Mo), *Solid State Sci.* 10(3), 321 (2008)

309. E. J. Liang, H. Huo, J. Wang, and M. J. Chao, Effect of water species on the phonon modes in orthorhombic $Y_2(MoO_4)_3$ revealed by Raman spectroscopy, *J. Phys. Chem. C* 112(16), 6577 (2008)

310. Z. Y. Li, W. B. Song, and E. J. Liang, Structures, phase transition, and crystal water of $Fe_{2-x}Y_xMo_3O_{12}$, *J. Phys. Chem. C* 115(36), 17806 (2011)

311. N. A. Banek, H. I. Baiz, A. Latigo, and C. Lind, Autohydration of nanosized cubic zirconium tungstate, *J. Am. Chem. Soc.* 132(24), 8278 (2010)

312. N. Duan, U. Kameswari, and A. W. Sleight, Further contraction of ZrW_2O_8, *J. Am. Chem. Soc.* 121(44), 10432 (1999)

313. Q. L. Gao, J. Chen, Q. Sun, D. H. Chang, Q. Z. Huang, H. Wu, A. Sanson, R. Milazzo, H. Zhu, Q. Li, Z. N. Liu, J. X. Deng, and X. R. Xing, Switching between giant positive and negative thermal expansions of a $YFe(CN)_6$-based Prussian blue analogue induced by guest species, *Angew. Chem. Int. Ed.* 56(28), 9023 (2017)

314. A. L. Goodwin, K. W. Chapman, and C. J. Kepert, Guest-dependent negative thermal expansion in nanoporous Prussian blue analogues $M^{II}Pt^{IV}(CN)_6 \cdot x(H_2O)$ ($0 \leq x \leq 2$; M =Zn, Cd), *J. Am. Chem. Soc.* 127(51), 17980 (2005)

315. T. Pretsch, K. W. Chapman, G. J. Halder, and C. J. Kepert, Dehydration of the nanoporous coordination framework $Er^{III}[Co^{III}(CN)_6]\cdot 4(H_2O)$: Single crystal tosingle crystal transformation and negative thermal expansion in $Er^{III}[Co^{III}(CN)_6]$, *Chem. Commun. (Camb.)* 17(17), 1857 (2006)

316. M. K. Gupta, R. Mittal, B. Singh, and S. L. Chaplot, Effect of hydration and ammonization on the thermal expansion behavior of ZrW_2O_8: *Ab initio* lattice dynamical perspective, *Phys. Rev. B* 98(22), 224303 (2018)

317. H. Liu, Z. Zhang, W. Zhang, X. Zeng, and X. Chen, Synthesis and negative thermal expansion property of $Y_{2-x}La_xW_3O_{12}$ ($0 \leq x \leq 2$), *Ceram. Int.* 39(3), 2781 (2013)

318. Q. J. Li, B. H. Yuan, W. B. Song, E. J. Liang, and B. Yuan, Phase transition, hygroscopicity and thermal expansion properties of $Yb_{2-x}Al_xMo_3O_{12}$, *Chin. Phys. B* 21(4), 046501 (2012)

319. X. S. Liu, Y. G. Cheng, E. J. Liang, and M. J. Chao, Interaction of crystal water with the building block in $Y_2Mo_3O_{12}$ and the effect of Ce^{3+} doping, *Phys. Chem. Chem. Phys.* 16(22), 12848 (2014)

320. X. S. Liu, B. H. Yuan, Y. G. Cheng, X. H. Ge, E. J. Liang, and W. F. Zhang, Avoiding the invasion of H_2O into $Y_2Mo_3O_{12}$ by coating with C_3N_4 to improve negative thermal expansion properties, *Phys. Chem. Chem. Phys.* 19(21), 13443 (2017)

321. A. Sanson, On the switching between negative and positive thermal expansion in framework materials, *Mater. Res. Lett.* 7(10), 412 (2019)

322. M. Cetinkol and A. P. Wilkinson, Pressure dependence of negative thermal expansion in $Zr_2(WO_4)(PO_4)_2$, *Solid State Commun.* 149(11–12), 421 (2009)

323. M. Cetinkol, A. P. Wilkinson, and P. L. Lee, Structural changes accompanying negative thermal expansion in $Zr_2(MoO_4)(PO_4)_2$, *J. Solid State Chem.* 182(6), 1304 (2009)

324. M. Y. Wu, L. Wang, Y. Jia, Z. X. Guo, and Q. Sun, Theoretical study of hydration in $Y_2Mo_3O_{12}$: Effects on structure and negative thermal expansion, *AIP Adv.* 5(2), 027126 (2015)

325. M. Y. Wu, Y. Jia, and Q. Sun, Effects of A^{3+} cations on hydration in $A_2M_3O_{12}$ family materials: A first-principles study, *Comput. Mater. Sci.* 111, 28 (2016)

326. G. Jefferson, T. A. Parthasarathy, and R. J. Kerans, Tailorable thermal expansion hybrid structures, *Int. J. Solids Struct.* 46(11–12), 2372 (2009)

327. L. Wu, B. Li, and J. Zhou, Isotropic negative thermal expansion metamaterials, *ACS Appl. Mater. Interfaces* 8(24), 17721 (2016)